Modelling Peptides at Interfaces in Atomic Detail

vorgelegt von
Dipl.-Phys.
Tobias Daniel Pobandt
aus Meppen

Von der Fakultät II - Mathematik und Naturwissenschaften
der Technischen Universität Berlin
zur Erlangung des akademischen Grades

Doktor der Naturwissenschaften
- Dr. rer. nat. -

genehmigte Dissertation

Promotionsausschuss:

Vorsitzende:	Prof. Dr. Sabine Klapp
Gutachter:	Prof. Dr. Martin Schoen
Gutachter:	Dr. Volker Knecht

Tag der wissenschaftlichen Aussprache: 13. Dezember 2013

Berlin 2014
D 83

Contents

1 Introduction

The interaction between proteins and biomembranes is crucial for many biological processes including membrane fusion, selective transport through membranes, or defence mechanisms of the innate immune system. Under pathogenic conditions this interaction might be strongly involved in the progress of several severe maladies including neurodegenerative diseases. A prevalent example of such a neurodegenerative disease is Alzheimer's disease. Here, the mutual interaction of the so-called amyloid β (Aβ) peptide with cellular membranes is believed to be essential for the pathogenesis. Cellular membranes might promote aggregation of the peptide which may result in the formation of amyloid deposits. On this aggregation pathway the peptide accumulates into various toxic oligomers which affect the cell membrane by increasing its permeability for ionic species like Ca^{2+} ions leading to calcium dyshomeostasis and, subsequently, cell death. This alteration of the membrane permeability might arise from peptide mediated membrane pores.

Another class of peptides capable to induce pores in membranes is provided by antimicrobial peptides. These peptides are part of the innate immune system of nearly all higher organisms. Antimicrobial peptides attack and kill intruding prokaryotic cells like bacteria but spare organism innate eukaryotic cells. Several studies suggest that this selectivity arises from different affinities of the peptides to prokaryotic and eukaryotic plasma cell membranes due to a different lipid composition between these two types of membranes. Antimicrobial peptides may play a fundamental role in future health care as they might serve as a template for the development of peptidomimetic alternatives to conventional

antibiotics which suffer from increasing inefficiency due to growing resistance of pathogenic bacteria.
In this study three questions concerning peptide-membrane interactions are addressed. The first two involve the amyloid β peptide and its role in Alzheimer's disease and the third the selectivity mechanism of antimicrobial peptides.

- How do various factors like the presence of interfaces, pH or the number of residues influence the folding behaviour of Aβ monomers?
- How does the Aβ monomer affect membrane defects like water pores in terms of their size, frequency, or stability?
- How does the lipid composition affect the membrane affinity of the antimicrobial peptide NK-2?

All three questions are addressed by molecular dynamics (MD) simulations. In the first case 2μs MD simulations in combination with secondary structure and cluster analysis methods are employed to study the folding behaviour of Aβ_{40} and Aβ_{42} in bulk solution and at an air-water-interface under slightly acidic and pH neutral conditions. The influence of the Aβ_{42} monomer on membrane defects is investigated by determining the free energy of water pores within zwitterionic phospholipid bilayers by means of MD simulations combined with the umbrella sampling technique. Finally, the difference in the affinity of NK-2 for anionic and zwitterionic phospholipid bilayers is estimated by MD simulations in conjunction with the thermodynamic integration (TI) method. All methods are introduced in chapter 2.
In the remainder of this chapter the biological background is given. In section 1.1 phospholipid bilayers serving as model systems for biomembranes are introduced. Subsequently, the structure and the aggregation process of amyloids known to be formed by several different peptides are presented in section 1.2. Alzheimer's disease and in particular the Aβ peptide as well as peptide-mediated calcium dyshomeostasis are described in section 1.3. Finally, antimicrobial peptides, their mode of action, and especially the NK-2 peptide are treated in section 1.4.

1.1 Biological membranes and phospholipid bilayers

Biological cells are categorized as (i) eukaryotes being mostly the building-blocks of multicellular organisms like animals, land plants, and fungi, or (ii) prokaryotes occurring mostly as unicellular organisms including bacteria, archaea, or protozoa. In eukaryotic cells the majority of the genetic material is stored in a nucleus enveloped by a membrane whereas the genetic material of prokaryotes is largely bound in a DNA/protein complex, the so-called nucleoid. In contrast to prokaryotes, eukaryotic cells are furthermore compartmentalized into organelles like the nuclei, mitochondria, chloroplasts, and the endoplasmic reticulum.
However, in both cases cell membranes are essential for the existence and viability of the cell. They do not just simply separate the inside from the outside of the cell but also fulfil many fundamental biological tasks as the importation of gases, nutrients, or solutes into the cell, as well as the exportation of toxic waste products out of the cell. The permeability of cell membranes has thus to be highly selective concerning the molecular species and the direction of the molecular flux through the membrane. Permeation through membranes is enabled by passive diffusion as well as active transport by carrier and channel proteins. Furthermore cell membranes have to maintain large chemical gradients between the intra- and extracellular space. This involves especially ionic species. For instance the extracellular concentration of K^+ ions is with ~ 4 mM much lower than inside the cell where a K^+ ion concentration of ~ 140 mM is maintained. The concentration of Ca^{2+} ions outside the cell is typically 1000-fold higher than in the cytosol [1].
Biological membranes are mainly composed of lipids and integral or peripheral

Membrane	Lipid	Protein
Myelin Sheath	80%	20%
Plasma Membrane	50%	50%
Mitochondrial Inner Membrane	25%	75%

Table 1.1: Mass content of lipids and proteins of three different mammalian membranes as taken from [1].

proteins. Here, the protein content strongly depends on the biochemical functionality of the membrane as indicated in table 1.1. Myelin sheaths have a rather simple biological function as they merely electrically insulate axons whereas mitochondrial inner membranes fulfil several tasks involving the reformation of the energy carrier adenosine triphosphate (ATP). Lipids can be grouped into functional lipids like phosphatidylinositol, phosphatic acid or gangliosides as well

as lipids playing a predominately structural role. The latter can furthermore be categorized into sterols like cholesterol, phospholipids including phosphatidylcholine (PC), phosphatidylethanolamine (PE) or phosphatidylglycerol (PG), and sphingolipids like cerebrosides or glycolipids. Especially phospholipids provide the main component of biomembranes. The structure of three different phospholipids is exemplary shown in figure 1.1. These lipids contain a polar headgroup composed of an alcohol group, phosphate, and glycerol and two non-polar tails each comprising 14 to 24 hydrocarbon groups. Hydrocarbon tails can be saturated as well as mono- or poly-unsaturated.

The amphipathic nature of phospholipids is essential for the formation of lipid

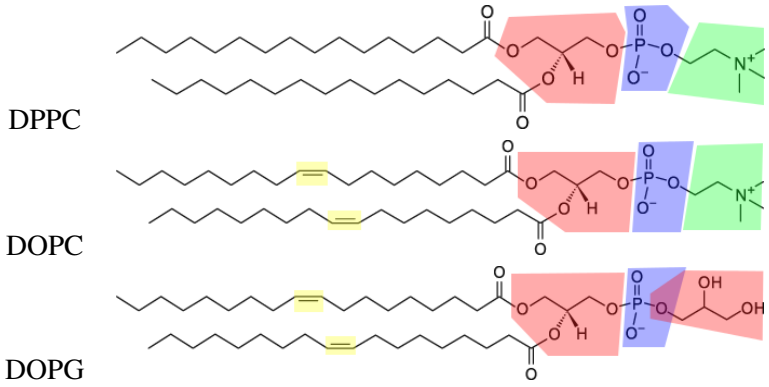

Figure 1.1: Structure of phospholipids considered in this study. Shown are zwitterionic dipalmitoylphosphatidylcholine (DPPC) (chapter 4) and dioleoylphosphatidylcholine (DOPC) (chapter 5) as well as anionic dioleoylphosphatidylglycerol (DOPG) (chapter 5). Cationic choline groups are highlighted in light green, anionic phosphate groups in blue, neutral glycerol groups in red, and acyl groups in yellow.

bilayers being the basis of biomembranes. Lipid bilayers are composed of two leaflets of phospholipids arranged such that the lipid head groups are aligned in a plane whereas all hydrocarbon tails point in one direction. Both leaflets are orientated in opposite direction with the hydrophilic head groups facing water and the hydrophobic hydrocarbon tails buried in the bilayer interior as shown in figure 1.2. Lipid bilayers form spontaneously if the concentration of phospholipids solvated in water exceeds a critical value. Depending on the environmental conditions and the lipid concentration other assemblies like micelles or vesicles may form. This self assembly process is largely driven by the hydrophobic effect which results from a entropy loss of water molecules surrounding solvated non-polar particles. The self assembly of (partially) non-polar molecules into larger clusters minimizes the described entropy loss due to a decreased contact surface with the aqueous environment. A well known example for this effect are oil droplets in water. The lack of covalent bonds stabilizing the bilayer struc-

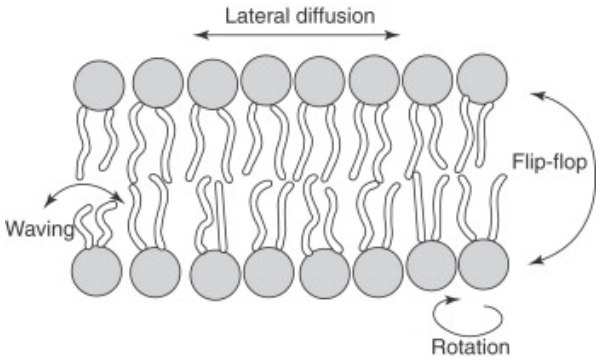

Figure 1.2: Model of a phospholipid bilayer as taken from [2].

ture allows phospholipids as well as incorporated proteins to rotate and diffuse almost freely lateral to the bilayer surface which is why a phospholipid bilayer is described as a two dimensional fluid. Even lipid flip flops denoting the translation of a phospholipid from one leaflet to the other are possible.

The first biomembrane model proposing the described lipid bilayer structure including incorporated integral and peripheral proteins was postulated by Singer and Nicolson in 1972 and is known as the fluid mosaic model [3]. Their model was the first to be capable of describing the lateral protein and lipid dynamics. An extension of the fluid mosaic model was provided by Simon and Ikonen in 1997 by additionally regarding so called lipid rafts [4]. Lipid rafts are sphingolipid- and cholesterol-rich relatively tight packed microdomains floating in the lipid bilayer matrix which might be associated with cellular signalling processes [5]. Here, cholesterol is believed to serve as glue holding the microdomain together whereas the higher packing density results from an extraordinarily high content of saturated hydrocarbon tails.

The phospholipid composition of the outer plasma membrane leaflet of eu- and prokaryotic cells differs in that the plasma membrane of eukaryotes contains mainly zwitterionic PC lipids and cholesterol whereas prokaryotic membranes contain phospholipids with anionic PG or zwitterionic PE head groups. Prokaryotic cells are surrounded by a cell wall which can be either detected as gram-positive or gram-negative depending on its peptidoglycan, i. e. murein, content.

1.2 Amyloid deposits

1.2.1 Components and structure

In 1854 the German physician Rudolph Virchow found deposits in abnormal human brains that showed a characteristic reaction with iodine similar to that seen for starch. He denominated these deposits 'amyloids' as this term had been previously used for starchy (i.e. amylaceous) components of plants by the German botanist Mathias Schleiden in 1838 [6]. Nowadays it is known that amyloids are mainly composed of unbranched fibrillar structures of peptides or proteins as shown in figure 1.3. Amyloid fibrils are associated with several neurodegen-

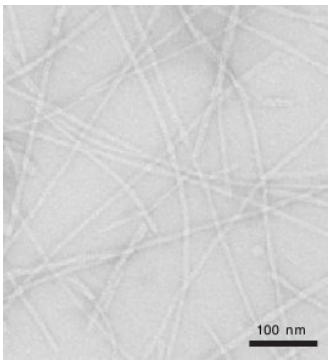

Figure 1.3: Amyloid fibrils of the islet amyloid polypeptide (IAPP) associated with type II diabetes visualized by electron microscopy (EM) as taken from [7].

erative diseases like Alzheimer's, Parkinson's, and Huntington's disease as well as non-neuropathic diseases like type II diabetes. These fibrils arise due to misfolding and subsequent aggregation of disease-related proteins or peptides, like the amyloid β (Aβ) peptide (39 to 43 residues) associated with Alzheimer's, α-synuclein protein (140 residues) related to Parkinson's, or the huntingtin protein (about 3144 residues) with expanded polyQ stretches associated with Huntington's disease. Although formed by many different peptides or proteins with diverse amino acid sequences as well as chain lengths, the corresponding fibrils exhibit similar structures. As revealed by atomic force microscopy (AFM) and transmission electron microscopy (TEM) they are typically built of two to six protofilaments with diameters between 2 nm and 5 nm. If these protofilaments twist around each other along the fibril axis as shown in figure 1.4 (*left*) they form rope-like fibrils with a diameter of 7-13 nm [8, 9], whereas they form ribbon-like fibrils with a thickness of 2-5 nm and a width of up to 30 nm if they align laterally [10–12].

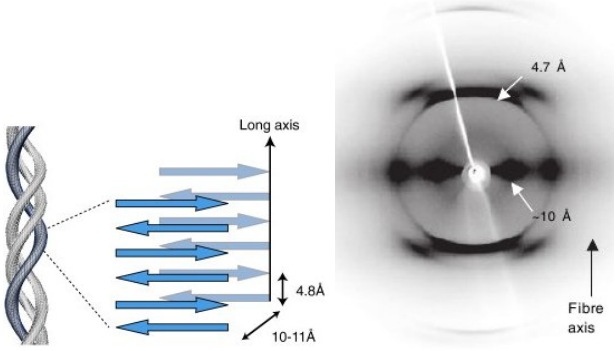

Figure 1.4: Sketch of the molecular cross-β structure of amyloid protofilaments (*top*) as taken from [13] and the characteristic X-ray fibre diffraction pattern (*bottom*) of fibrils consisting of islet amyloid polypeptides (IAPP) as taken from [7].

Polypeptides within a protofilament are arranged in a characteristic cross-β structure where the polypeptide forms β-strands normal and inter-strand hydrogen bonds nearly parallel to the fibril axis indicated in figure 1.4 (*middle*). Characteristic patterns from X-ray diffraction experiments [7, 14] are shown in figure 1.4 (*right*). A strong meridional reflection at 4.7 Å corresponds to the hydrogen bonding distance between the β-strands and the more diffuse equatorial reflection at about 10 Å to the inter-sheet distance as apparent from figure 1.4 (*middle*). The latter depends on the side chain lengths of the fibril forming polypeptides and may vary from 5 to 15 Å [15, 16]. The β-sheets as well as the β-strands may be in parallel or antiparallel orientation. The relative orientation cannot be determined from X-ray diffraction but from solid-state nuclear magnetic resonance (SSNMR) [17] and Fourier-transform infrared spectroscopy (FTIR) [18]. Further experimental techniques to illuminate the structure of amyloid fibrils include circular dichroism (CD) spectroscopy and electron microscopy (EM). The presence of regular β-sheet and therefore fibril structures can be detected by the fluorescence of Thioflavin T (ThT) as well as by the binding of Congo red (CR) [19].

1.2.2 Formation: Misfolding and intermediates

The aggregation of proteins or peptides into amyloids arises due to their misfolding under specific pathological conditions. A large number of human diseases is associated with protein misfolding, with the majority of these diseases being linked to the formation of fibrillar aggregates. Misfolding takes place due to pathological, non-natural conditions which prevent the folding or refolding of the corresponding polypeptide into, or support their unfolding out of, their native, functional state.
Since 1998 an increasing number of proteins not related to amyloid diseases were found to undergo fibril formation [16, 20–22]. It is furthermore notable that all amyloid forming proteins show no similarities in sequence, size or native folding structure [23, 24]. This led to the proposal of the "generic hypothesis" of amyloid formation which states that the ability to aggregate into fibrils is a generic property of the backbone of all polypeptide chains [25] though the propensity for fibril formation depends on the particular amino acid sequence. Amino acid substitution experiments show that the aggregation susceptibility of a polypeptide can be increased by decreasing its net charge or increasing its hydrophobicity as well as its propensity to form β-structures [26]. The folding of a protein into its native state and its aggregation can be seen as two separate but competitive processes. They are distinct as the unique native structure of a natural protein is determined by its amino acid sequence selected by evolution whereas the aggregation into fibrils occurs for each polypeptide with no regard of its specific amino acid sequence. The native state is mainly determined by side chain and the fibrillar conformation by main chain interactions [15, 24]. Which of these effects is dominant is determined by the given conditions. In natural environments the biological relevant conformation state of a protein is its native state. Several mechanisms in living cells including chaperones or ubiquitination help the protein to find its native state and suppress misfolding. These control mechanisms can fail in amyloid diseases as they may be saturated due to an overbalance of misfolded proteins. This may furthermore be caused by the overproduction of the corresponding protein or the failing of its clearance [27].
The close competition between folding and aggregation is indicated in the free energy landscape of conformational and oligomerization states shown in figure 1.5. Although the thermodynamically most stable state and thus the global free energy minimum is assumed to correspond to fibrillar structures these structures are not readily adopted, as proteins have to overcome large free energy barriers to escape their native state where they may be kinetically trapped. The shape of the free energy landscape depends on the amino acid sequence of the polypeptide as well as the environmental conditions like pH, temperature, ionic strength, polarity of the medium, peptide concentration and available space. In general the

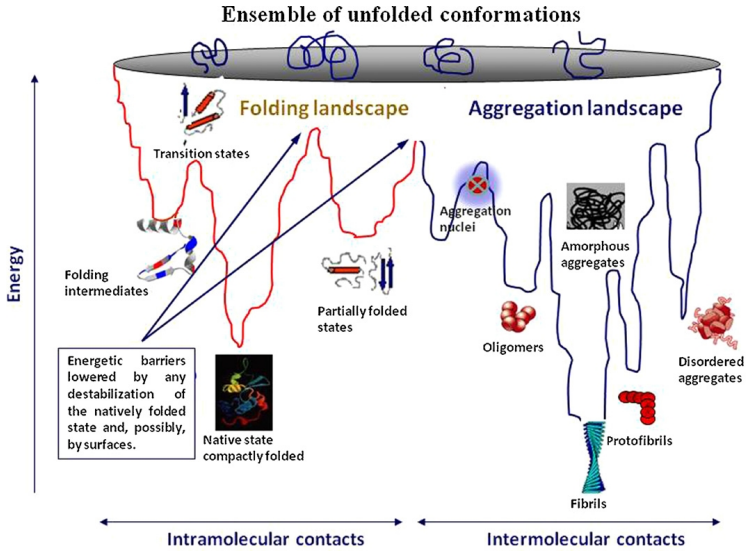

Figure 1.5: Free energy landscape of peptide folding and aggregation as taken from [24].

latter is much larger *in vitro* than *in vivo* as the concentration of macromolecules inside the cell amounts to 20-30 % of the total volume. This 'macromolecular crowding' reduces the conformational space available for the polypeptide dramatically and favours the occupation of rather compact structures like the native or the aggregation state [24, 28].

An important factor for the folding and misfolding process is the interaction of the corresponding polypeptide with surfaces. In the native environment, such surfaces are provided by macromolecules or membranes and can support protein folding as well as unfolding followed by aggregation. Here the efficiency and rate of protein folding is enhanced at the surface or the interior of chaperones [29] whereas membrane surfaces allow polypeptides to partly unfold and adopt aggregation prone states. Furthermore, surfaces increase the local polypeptide concentration accelerating its aggregation [30–32]. Evidence from sonication experiments suggests that even for *in vitro* experiments intended to probe aggregation in solution, interactions with interfaces as provided by accidentally present gas bubbles determines the kinetics of aggregation and fibril formation [33, 34].

As the aggregation-prone residues of natively folded polypeptides like globular proteins are usually shielded by side-chains a partial unfolding of the polypeptide is often necessary before aggregation takes place. For several natively unstructured polypeptides, aggregation is preceded by the formation of secondary structure [22]. In both cases the peptide adopts a partially folded state before

entering the aggregation landscape as indicated in figure 1.5.
During the aggregation of monomers the number of fibrils grows exponentially after an initial lag phase as it was observed *in vitro* by the binding of Thioflavin T (ThT). This lag phase can be shortened by adding preformed fibrillar structures [35, 36]. This suggests that the formation of fibrils involves a nucleation process representing the rate limiting step. The nucleus therefore resides at a local free energy maximum. Due to their heterogeneity the states of small oligomers are not as well defined as for fibrils, protofilaments, or natively folded proteins.

The interplay between different folding and aggregation states of a polypeptide can be illustrated in a network of equilibria as shown in figure 1.6. After synthesis from the ribosome and under natural conditions the initially unstructured polypeptide folds into its native state. These natively folded peptides may associate into functional oligomers as it occurs for actins, myosins, or microtubules. Along its folding pathway the polypeptide undergoes several transitions between partially folded intermediates. Non-natural conditions can cause the aggregation of these intermediates into more or less disordered, soluble, low-weight aggregates. For the amyloid-β peptide such oligomers were found to assemble and dissolve at very high rates. They typically consist of two to six mainly unstructured monomers [37, 38]. These small oligomers may be precursors of larger, metastable, in general β-sheet enriched protofibrils which adopt different shapes like spherical beads with a diameter of 2-5 nm, linear or curly chains consisting of these beads or doughnut-like, annular structures [39, 40]. Several polypeptides including amyloid β, α-synuclein, or polyQ-containing proteins [23] were found to form protofibrils assumed to precede the aggregation into fibrils [23, 41, 42]. Interestingly, in some cases aggregation was found to take place before the unfolding of the polypeptide. This results in the temporary formation of native-like aggregates where the native structure of the corresponding polypeptide is almost retained. Examples are given by the insulin peptide [43] or the pathogenic form of the ataxin-3 protein [44] associated with spinocerebellar ataxia type-3 also known as 'Machado Joseph disease'. Beside these aforementioned on-pathway oligomers several off-pathway products also occur during the aggregation process.
Nowadays much effort is put into the investigation of these off- and on-pathway oligomers as they have been found to be the major toxic species along the aggregation pathway. This was observed for several disease- (e.g. amyloid β [45, 46] or α synuclein [47]) as well as nondisease-associated polypeptides [48, 49]. Their toxicity may be caused by the exposure of residues usually buried in the native or fibrillar state. This may cause several undesired, harmful interactions with cell components as for example the plasma membrane resulting in the for-

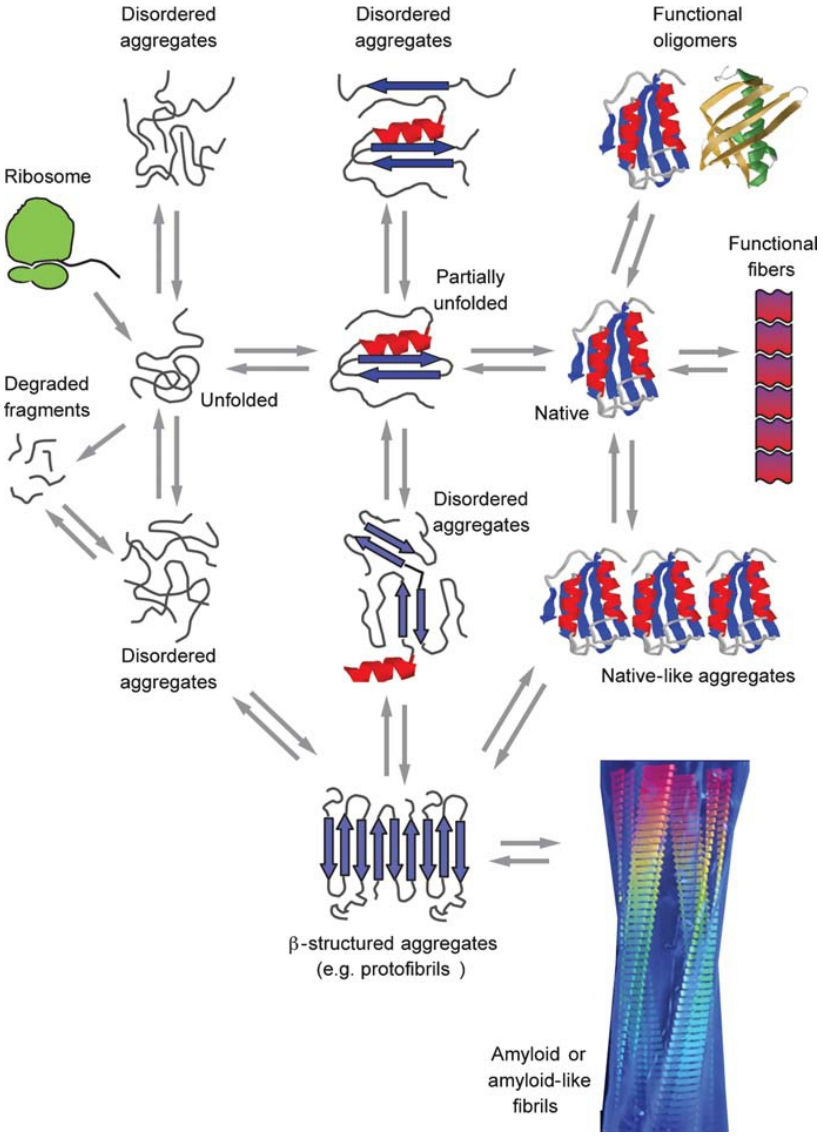

Figure 1.6: Aggregation and folding pathways taken from [23].

mation of membrane pores [23]. The proportion of exposed residues is increased for smaller oligomers.

1.3 Alzheimer's disease

Alzheimer's disease (AD) being the most common form of dementia is an age related, progressive, fatal, and up to date incurable neurodegenerative disorder. It affects memory, thinking as well as behaviour and is therefore an extremely staggering diagnosis for patients and their families. The risk of dementia roughly doubles every five years for individuals aged over 65 years. In 2010 about 36 million people were suffering from dementia worldwide. The total related costs were estimated to US$ 604 billion. According to the 2010 annual report of Alzheimer's Disease International (ADI) the number of dementia patients is expected to increase up to 115 million until 2050 due to increasing life expectancies. Especially in the developing countries the number of affected individuals will increase dramatically [50].

1.3.1 Molecular aspects

In a 1907 published study Alois Alzheimer for the first time described the disease-typical extracellular deposits accumulating in specific regions of the cortex of the brain as well as the neurofibrillary tangles within neurone cells [51]. He obtained his insights from a post-mortem examination of Auguste Deter who suffered from an early onset type of the disease showing symptoms like rapid memory loss, delusion and disorientation [52]. In the 1980s the extracellular deposits were identified as senile plaques consisting of fibrillar structures of the peptide amyloid β (Aβ) [53] and the neurofibrillary tangles as aggregates of hyperphosphorylated tau proteins [54–56].
Hydrophilic tau proteins primarily occur in neuron cells where they facilitate the nucleation and stabilization of microtubules. In tauopathic diseases like AD, hyperphosphorylated tau proteins aggregate in an abnormal way as they form neurofibrillary tangles which might be neurotoxic. Furthermore the aberrant aggregation of tau proteins provokes the destabilization and reorganization of microtubules. This also influences other subcellular components like mitochondria or lysosomes. The number of tangles correlates with the grade of dementia in AD [57].
The 37 to 43 residues long Aβ peptide is a cleavage product of the type I orientated trans-membrane amyloid precursor protein (APP). The physiological role of APP is still unclear and a matter of intense research. It might be crucial for the survival of neurones, plasticity of synapses as well as the adhesion of cells [58], and furthermore seems to have synapto- and neurotrophic functions [59].
The proteolytic enzymes are called secretases. The cleavage of APP via the secretases proceeds either via a non-amyloidogenic or an amyloidogenic and therefore pathological pathway as shown in figure 1.7. In the non-amyloidogenic

pathway the APP is first cleaved by α-secretase releasing the peptide APPsα into the extracellular space (lumen) and leaving behind the αAPP carboxy-terminal fragment (CTF). Subsequent intersection of the latter by γ-secretase within the hydrophobic membrane environment delivers the non disease relevant peptide P3. In the amyloidogenic pathway the cleavage of APP by β-secretase leaves the αAPP CTF domain in the membrane whereas the APPsβ peptide escapes into the lumen. The following cleavage by γ-secretase generates the Aβ peptide. In both pathways APP intracellular domains (AICD) are delivered into the cytosol. These peptides might play a role in nuclear signalling [60]. Both cleavage pathways compete with each other.
In rare, autosomal, early onset forms of AD gene mutations lead to an overproduction of the 42 amino acids long, most toxic and most amyloidogenic form of Aβ. This gives strong evidence for the pivotal role of the Aβ peptide and its aggregation process in the pathogenesis of AD. It is expressed in the prevalent 'Amyloid-hypothesis' [53, 61]. The susceptibility for the most common, sporadic form of AD is determined by different genes which still have to be completely identified. One of these genes is located at chromosome 19 and is responsible for the generation of the apolipoprotein E (ApoE). The gene occurs in three different alleles which results in the generation of three different isoforms of ApoE. A higher risk of AD is associated with the production of the ApoE-ε4 isoform which might cause an increased cleavage and aggregation as well as a decreased clearance of the Aβ_{42} peptide [58].

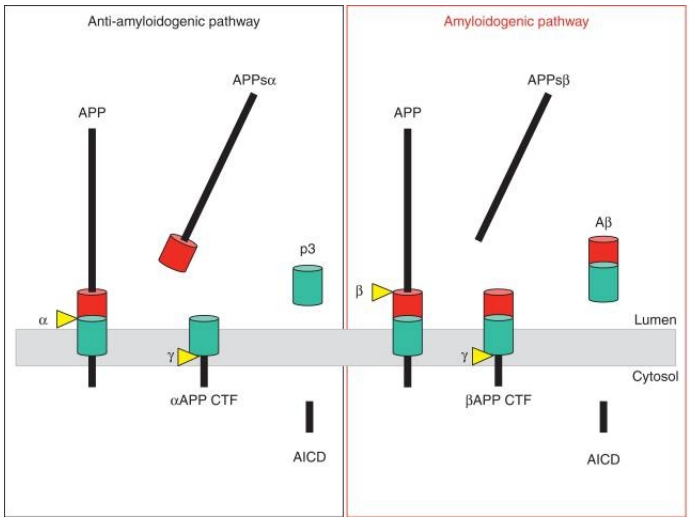

Figure 1.7: The anti-amyloidogenic (*left*) and the amyloidogenic (*right*) pathway of APP cleavage as taken from [60].

Several findings support the view that not insoluble mature fibrils but instead soluble structures like small oligomers [62, 63], Aβ derived diffusible ligands (ADDL) [64] or protofibrils [65,66] are the most toxic forms of the Aβ peptide. Several different mechanisms may cause the neurotoxicity of Aβ. Patients of AD exhibit an increased concentration of highly reactive oxygen species (ROS) in brain cells. This oxidative stress might be correlated with the Aβ peptide in a vicious circle. On the one hand, the interaction of Aβ with metal ions as Fe^{2+} or Cu^{+} generates reactive oxygen radicals (ROS) like hydrogen peroxide increasing the oxidative stress [67, 68]. On the other hand, oxidative stress might promote the amyloidogenic cleavage of APP and therefore the generation of Aβ [58]. The radicals provoke lipid peroxidation and protein oxidation [69]. Furthermore the oxidative stress causes changes in membrane transport, receptor, ion channel, or even tau proteins. The latter might facilitate the formation of neurofibrillary tangles [58]. In addition, Aβ also directly interacts with tau proteins leading to a disassembly of microtubules followed by cell death [70]. Another very important aspect of Alzheimer's disease is the disruption of calcium homeostasis as described in section 1.3.3.

Larger amounts of Aβ oligomers are especially found in the vicinity of synapses as APP is transported along the axons and cleaved at presynaptic terminals. Neuronal death might start at synapses where Aβ oligomers cause disruption of calcium homeostasis, alterations in vesicle trafficking, oxidative stress as well as the injury of mitochondria and the endoplasmic reticulum. The obstruction of long-term potentiation by Aβ oligomers might be the reason for memory deficits at an early stage of the disease before degeneration of neurons takes place [58, 71, 72].

Several therapeutic approaches against AD are still under development. One of these approaches is based on preventing the cleavage of toxic forms of the Aβ peptide by β- or γ-secretase blockers [73]. Other strategies try to reduce the fibril formation and therefore the oligomerization of Aβ. This can be obtained by binding Aβ aggregation provoking copper and iron ions to ligands. The resulting complexes additionally reduce oxidative stress [58]. Promising as well are therapies based on the stimulation of the immune system which consequently increases the clearance of Aβ from the brain [74, 75].

1.3.2 Amyloid β

The amino acid sequence of the Aβ_{42} peptide is shown in figure 1.8. The peptide is amphiphilic as it contains a largely hydrophilic domain starting from its N-terminus and spanning the residues ASP1 to LYS16 and an hydrophobic domain spanning the residues LEU17 to ALA42.

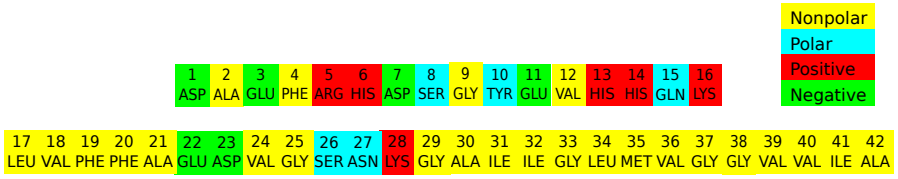

Figure 1.8: Amino acid sequence of the Aβ_{42} peptide and the charge state of its residues at the isoelectric point.

Several findings indicate that the so called 'self recognition site' including the residues Lys16 to Phe20 is crucial for the oligomerization and formation of fibrils [76]. It serves as 'glue' to bind several peptides together. Especially π-stacking interactions between the aromatic rings of the phenylalanine residues Phe19 and Phe20 are believed to drive the aggregation and determine the β-sheet structure [77]. According to this the domains Aβ_{15-20} [78] as well as Aβ_{17-21} [79] have been reported to bind to the full length Aβ_{42} peptide. The Aβ_{16-22} domain assembles into well ordered fibrils [80].
The hydrophobic C-terminal domain of the Aβ peptide which is buried in the membrane environment before cleavage of APP takes place features three GlyXXXGly motifs involving the residues Gly25, Gly29, Gly33, and Gly37. Such glycine patterns are rather common in helical transmembrane channel proteins and believed to drive and determine the packing of these proteins by the so called glycine zipper mechanism resulting in the formation of membrane channels [81]. On the other hand glycine is known to destabilize helices in aqueous environments due to its high flexibility [82]. The direct interaction of Aβ oligomers with the membrane leading to the emergence of ion permeable membrane channels might play a crucial role in the pathogenesis of Alzheimer's disease as described in section 1.3.3. Singular substitutions of Gly25, Gly29, Gly33 or Gly37 by leucine within the Aβ_{42} peptide have been shown to reduce the neurotoxicity of the peptide and concentration of small toxic oligomers in solution and attached to lipid membranes [83, 84]. These findings underline the crucial role of the GlyXXXGly motif for oligomerization and membrane binding of Aβ and therefore its neurotoxicity.

The three histidine residues His6, His13, and His14 are double protonated in slightly acidic and mono protonated in pH neutral environments. This leads to a change in the net charge of the peptide from -3 e in neutral to 0 in acidic environments. Accordingly, the hydrophilicity of the N-terminal residues decreases which might promote amyloid formation [85]. This may be disease-relevant as AD patients exhibit a rather acidic environment within the brain compared to the non diseased case [86].

A still very elusive question about Aβ concerns the much higher neurotoxicity and aggregation propensity of the Aβ_{42} alloform compared to Aβ_{40} as both peptides differ only in two additional residues. Simulation and nuclear magnetic resonance (NMR) spectroscopy studies suggest that the additional residues Ile41 and Ala42 increase the rigidity of C-terminal residues promoting aggregation [87,88]. By comparing the secondary structures of Aβ_{40} and Aβ_{42} at aggregation favouring ($T > 5°$C) and non-favouring ($T < 5°$C) conditions by a combination of CD and NMR spectroscopy it was found that both peptides undergo similar changes from coil to aggregation prone, β-sheet enriched conformations due to a temperature increase which suggests a similar aggregation mechanism. Striking differences were mainly observed for the C-terminal residues being more structured and prone for β-sheet formation in case of the Aβ_{42} alloform [89].

Despite much effort that had be taken into account the soluble structure of the full length Aβ_{40} and Aβ_{42} peptides in aqueous solution has so far not been identified. This is due to the peptides' high tendency to aggregate in water.

NMR experiments indicate that the Aβ_{10-35} fragment in aqueous solution adopts a stable collapsed coil structure lacking any significant secondary structure content but forming a well defined hydrophobic cluster spanning residues Leu17 to Ala21 [90]. Aβ_{10-35} is more soluble than the full length Aβ_{40} peptide but shows comparable chemical shifts in NMR measurements suggesting similar secondary structure features. The occurrence of a collapsed coil structure could not be confirmed for Aβ_{40} and Aβ_{42} by NMR spectroscopy at low temperatures ($< 5°C$) whereas local structure motifs as bends and turns appear similar [91]. More recent NMR experiments showed that Aβ_{40} in aqueous solution adopts a partially folded conformation exhibiting a helical structure spanning residues His13 to Asp23 [92]. Nowadays it is widely believed that the free energy landscape of folding for the Aβ peptide is rather flat. This implies a high dependence of the peptide structure on the environmental conditions as well as a rather high transition rate between different conformations. The latter is confirmed by NMR [93] as well as replica exchange molecular dynamics (MD) simulations in implicit [94] and explicit solvent [95]. These simulations predict several different peptide conformations featuring structures comprising rather small peptide

segments. Based on similarity the conformations can be classified into a few clusters between which rapid exchange was found. Hereby it has to be noted that the results from [94] should be regarded with care as peptide structure predictions by means of implicit solvent models suffer several shortcomings. For instance β-structure contents are under- and α-helix contents are overestimated, and non-native states appear to be overrepresented in replica exchange simulations [96].
In membrane-mimicking environments containing micelles or organic solvents like fluorinated alcohols (e.g. trifluoroethanol (TFE) or hexafluoroisopropanol (HFIP)) Aβ_{40} and Aβ_{42} were found to adopt mainly α-helical structures [97,98]. The peptides therefore have to undergo a transition from α-helical to β-sheet conformations on their pathway from the membrane environment to the aggregation state. Although this transition is still poorly understood, it could been monitored for the Aβ_{42} peptide solvated in a water/HFIP solution by NMR and CD spectroscopy [97]. The transition was induced by gradually increasing the water content of the water/HFIP solution and was shown to be reversible.

1.3.3 Interaction of amyloid β with membranes: Ca^{2+} dyshomeostasis

Aβ-mediated disruption of Ca^{2+} homeostasis in neuronal cells might provide an early and crucial step in the pathogenesis of Alzheimer's disease. The level of Ca^{2+} ions within the cytosol is rigorously regulated as Ca^{2+} ions play a crucial role in the functionality of essential enzymes including kinases or phosphatases. Furthermore, an elevation of the Ca^{2+} concentration within the cell activates proteolytic enzymes as for example calpain and caspase initiating apoptotic pathways leading to cell death [99]. Ca^{2+} ions enter into the cytosol via intracellular stores like mitochondria or the endoplasmic reticulum (ER) or from the extracellular fluid. In the latter case Ca^{2+} ions cross the plasma membrane via Ca^{2+} exchangers or receptor-, voltage-, or store-operated channels [100].
Ca^{2+} homeostasis might be disrupted by an increased influx of the ions into the cell induced by Aβ oligomers. Primarily three different mechanisms shown in figure 1.9 have been proposed:(i) the modulation of ion channels, (ii) disruption of membrane integrity, and (iii) the formation of high conductance cation pores. As to (i), Aβ oligomers were reported to strongly affect the permeability and activity of several Ca^{2+} associated channels like voltage-gated Ca^{2+} channels, serotonin receptors, glutamate receptors, dopamine receptors, or nicotinic acetylcholine receptors [101–105]. The interaction of Aβ with nicotinic acetylcholine receptors might result in the activation of several signal pathways leading to cell death [106].
As to (ii), a direct, non receptor mediated interaction of Aβ with the cell mem-

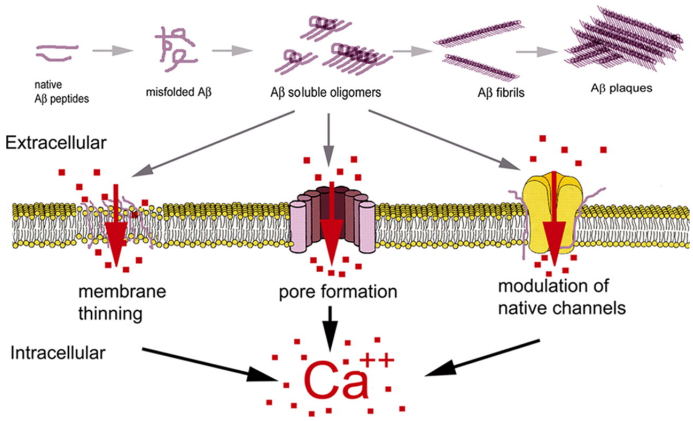

Figure 1.9: Schematic model of Ca^{2+} dyshomeostasis caused by the interaction of Aβ oligomers with cell membranes as taken from [100]. Aβ oligomers are part of the aggregation pathway of the misfolded Aβ monomer.

brane was proposed by Cribbs *et al.* who investigated the structural and assembly characteristics as well as the toxicity of all-D- and all-L-stereoisomers of truncated Aβ_{25-35} and Aβ_{1-42} peptides towards cultured hippocampal neurons [107]. For both alloforms they found no difference in the structural or toxic features between both stereoisomers. This suggests that Aβ directly interacts with the lipid matrix of the cell membrane as most receptor mediated interactions are stereoisomer-specific. Demuro *et al.* observed an increase of the intracellular Ca^{2+} level in human derived SH-SY5Y cells due to the presence of extracellular Aβ_{42} oligomers [108]. The enhanced permeability of the membrane for Ca^{2+} ions might be explained by a general disruption of the membrane lipid integrity as the addition of cobalt known to block various Ca^{2+}-permeable channels [109] as well as the depletion of intracellular Ca^{2+} stores does not affect the toxicity of the oligomers. Sokolov *et al.* proposed that an Aβ oligomer mediated increase of membrane ion permeability might arise from a lowering of the dielectric barrier provided by the non-polar bilayer core region. This furthermore might be caused by an increase in the area per lipid leading to a thinning of the membrane [110]. Sokolov *et al.* investigated the effect of Aβ oligomers on the electrical current through lipid bilayers solvated in different aqueous electrolyte solutions including KCl, NaCl, and $CaCl_2$. The electrical current increases due to the presence of Aβ oligomers and shows no jumps in its time evolution as it would be expected for the appearance of Ca^{2+} permeable channels. Furthermore they found that the effect of Aβ oligomers on the bilayer washes out rapidly indicating an interaction of the oligomers primarily with the bilayer surface. However, the membrane thinning observed by Solokov *et al.*

could also have been caused by hexafluoroisopropanol (HFIP) used to solvate the Aβ oligomers during their preparation as pointed out by Capone *et al.* [111].

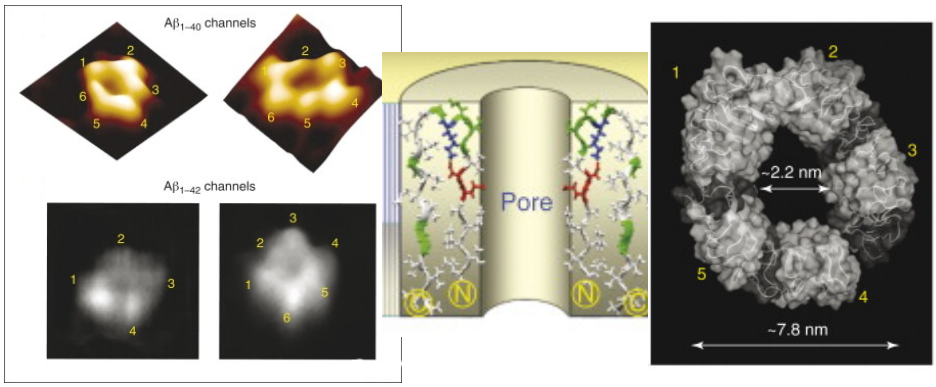

Figure 1.10: Pores induced by Aβ in planar lipid bilayers as observed by AFM (*left*) and MD simulations (*right*). The pores are characterized by four to six clumps of Aβ monomers as apparent from AFM images showing Aβ_{40} (*left,top*) and Aβ_{42} (*right,bottom*) mediated pores as taken from [112] and [113], respectively. A similar partition in loosely connected subunits can be observed by 30 *ns* MD simulations of an annular oligomer comprising 24 Aβ_{9-42} monomers located in a lipid bilayer (*right*) as reported by Jang *et al.* [114]. Here, ordered regions characterized by intermolecular β-sheets are depicted as light grey whereas more disordered regions are coloured dark grey. Each monomer was prepared to adopt an U-shaped strand-turn-strand motif with the hydrophilic N-terminus exposed to the pore interior and the hydrophobic C-terminus facing the non-polar bilayer core region (*middle*). Here, hydrophobic residues are shown in white, polar ones in green, positively charged ones in blue and negatively charged residues are depicted in red.

As to (iii), ion channels induced by Aβ_{40} in planar lipid bilayers were first reported by Arispe *et al.* in 1993 [115, 116]. These channels turned out to be highly cation selective as expressed by the magnitudes of membrane permeabilities $P_{Cs} > P_{Li} > P_{Ca} = P_K > P_{Na}$, to survive for minutes up to hours and to be blocked by Zn^{2+} ions. Furthermore as various single-channel conductances up to 5 nS were reported it is suggested that several different channel phenotypes may occur [115–117]. Atomic force microscopy (AFM) shown in figure 1.10 (*left*) revealed that pores induced by Aβ_{40} and Aβ_{42} are typically characterized by an outer diameter of $8-12$ nm and an inner diameter of $1-2$ nm. The rim of the channel is partitioned in four or six subunits which might themselves be tetra- or hexameric oligomers as suggested by biochemical analysis [112, 113]. The different sizes of the channels correspond to various levels of single-channel conductances [113]. As shown in figure 1.10 (*middle*), Jang *et al.* proposed the Aβ channels to consist of monomers adopting U-shaped strand-turn-strand motifs in the C-terminal residues Aβ_{17-42} whereas

the polar N-terminal residues Aβ_{1-16} are unstructured and solvated in the aqueous environment [114, 118, 119]. The described motif resembles the fibrillar secondary structure. Based on this hypothesis, Jang *et al.* simulated membrane pores formed by annular shaped oligomers of 12, 24 or 36 Aβ_{17-42} or Aβ_{9-42} monomers exhibiting the according U-shaped conformation. After 30 ns simulation time they found the shape and dimensions of the channel to agree with the results from AFM microscopy. In particular, the partitioning into subunits could be reproduced and their rigidity could be explained by intermolecular β-sheets comprising the inner and the outer β-strands, respectively. The formation of β-sheets spanning outer β-strands may not be possible in a perfect annular ring as the large diameter of the outer pore rim corresponds to a relatively large distance between the single β-strands.
Channels in lipid bilayers, liposomes, neurons, and fibroblasts were also found to be induced by several other amyloidogenic, disease-relevant peptides and may play a key role in various different misfolding diseases [120].

1.4 Antimicrobial peptides

In modern health care the increasing resistance of pathogenic bacteria against antibiotic agents is becoming a challenge of drastically growing importance [121]. During the last 20 years, the resistance against methicillin and vancomycin observed in hospitals increased exponentially whereas the number of new antibiotics decreased markedly [122]. A possible solution to this dilemma might be provided by antimicrobial peptides.

1.4.1 Properties and modes of action

Antimicrobial peptides represent an ancient part of the innate immune system of especially higher organisms like vertebrates, insects or plants [123]. As even one single species may possess more than 24 different antimicrobial peptides, their number can be expected to be humongous. Nowadays, more than 880 different antimicrobial peptides are known [124]. Besides directly attacking and killing intruding pathogens like fungi, bacteria, or viruses, antimicrobial peptides are also known to modify the immune system which impacts the infection and inflammation process [125]. As they are a component of the immune system they show on the other hand poor activity against eukaryotic cells. Although a large configurational diversity exists among antimicrobial peptides they can in general be characterized as cationic, amphipathic (usually they comprise about 50% hydrophobic amino acids) and also as relatively small as they mostly contain only 12 to about 50 residues. Based on their three dimensional structure and amino acid sequence antimicrobial peptides can be categorized into five

different subgroups [124]. These are (i) anionic peptides, (ii) linear cationic α-helical peptides, (iii) peptides containing cysteine and forming disulphide bonds, (iv) peptides containing a high content of certain amino acids including proline, phenylalanine, arginine or tryptophan, and, (v) peptides occurring as fragments of larger proteins. The majority of known antimicrobial peptides belongs to the second or the third group. Many of the about 290 cationic α-helical peptides are disordered in aqueous solutions but convert to α-helical structures if solvated in trifluoroethanol (TFE) or in presence of phospholipid vesicles as well as sodium dodecyl sulphate (SDS) micelles [126, 127]. Best studied peptides in this group include magainin 2 found in the African clawed frog *Xenopus laevis* as well as melittin occurring in bee venom. Protegrins appearing in porcine leukocytes are the primary representatives of the cysteine-containing disulphide bonding group. This group contains about 380 peptides. Due to the disulphide bonds they are prone to form stable β-sheets.

Several different killing and lysis modes of antimicrobial peptides have been

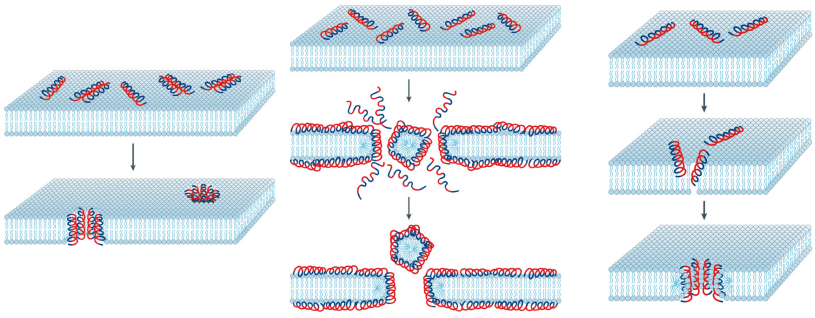

Figure 1.11: The barrel-stave (*left*), carpet (*center*) and the toroidal (*right*) models of antimicrobial peptide activity as taken from [124]. The peptides' hydrophilic part is depicted in red whereas the hydrophobic part is coloured blue.

discovered. On the one hand, they can cause cell death by intracellular mechanisms as for example the flocculation of intracellular contents [1] or the binding of nucleic acids[2]. Furthermore antimicrobial peptides have been suggested to inhibit the synthesis of cell walls [3], ribonucleic acids (RNA) [4], or proteins[4]as well as the activity of enzymes [5]. On the other hand, antimicrobial peptides address the cell plasma membrane causing the formation of ion channels, transmembrane pores, or membrane rupture. Although several mechanisms for mem-

[1] as observed for anionic peptides [128]
[2] as observed for Buforin 2 [129]
[3] as observed for Mersacidin [130]
[4] as observed for Pleurocidin [131]
[5] as observed for Histatins [132]

brane permeabilization mediated by antimicrobial peptides have been proposed especially three models, namely the barrel-stave-, the carpet- and the toroidal-pore-model presented in figure 1.11 are nowadays widely assumed. Initially, in case of low peptide/lipid ratios the peptides are bound parallel to the membrane surface whereas they change to a transmembrane orientation if the peptide/lipid ratio exceeds a peptide and membrane specific threshold. In the barrel-stave-model helical peptides arrange perpendicular to the bilayer surface aligning the rim of the pore and thus forming the stave of the barrel-shaped pore. Hereby the hydrophobic side of the peptide faces the apolar bilayer interior and the hydrophilic side the pore interior. To shield the apolar tail region from water the peptides are packed rather tightly. This mechanism has up to now only been found for the alamethicin peptide derived from the fungus *Trichoderma viride* [133]. In the carpet-model the cationic peptides accumulate at the membrane surface and cover its surface like a carpet. At high peptide/lipid ratios the peptide forms toroidal holes in the bilayer to increase the peptide accessible surface. This process is succeeded by the disintegration of the membrane and the formation of micelles. An example for a peptide showing this mechanism is the model peptide ovispirin [134]. In the toroidal-pore-model the polar sites of the peptides associate with the polar lipid head groups to form the rim of an hour-glass shaped pore and shield the bilayer core from water. Toroidal pores are formed by magainin 2, protregrins, and melittin [124, 133].
For both of the above described killing and lysis modes of antimicrobial peptides, the intracellular and the membrane associated mechanisms, the peptide first of all has to reach the cell plasma membrane. To address the plasma membrane of gram-negative bacteria the peptide has to pass an outer, lipopolysaccharide and phospholipids containing, outer membrane as well as a thin, rather stiff peptidoglycan layer. The plasma membrane of gram-positive bacteria is merely enveloped by a rather thick peptidoglycan layer. The peptidoglycan layer and the corresponding membranes are in each case separated by periplasmic space. The transit of antimicrobial peptides up to the plasma membrane is still poorly understood. For gram-negative bacteria a so-called self-promoting uptake process has been proposed [135] whereby the peptide initially binds to polyanionic lipopolysaccharides (LPS) incorporated in the outer membrane. The peptide displaces salt bridge relevant cations and partly neutralizes the LPS. This causes the rupture of the outer membrane which enables other peptides to pass. On the surface of gram-positive bacteria the cationic peptides might bind to teichoic acids [124].

1.4.2 NK-2 and its interaction with biological membranes

A very promising antibiotic agent may be provided by the NK-2 peptide. It is derived from the larger NK-lysin polypeptide which is furthermore synthesized by porcine NK (natural killer) or T-cells [136] [6] being part of the innate immune system of pigs. NK-lysin consists of 78 residues and folds into five amphipathic α-helices in aqueous [137] as well as in liposome solutions [138]. The peptide adopts a rather globular shape where the longest, residues 3-18 comprising helix is surrounded by the four remaining helices. This conformation is stabilized by three disulfide bridges [139]. NK-lysin has been reported to show lytic activity against gram-positive and gram-negative bacteria, fungi, and even tumour cells. On the other hand, it does not target red blood cells [136, 140].
In 1999 Andrä and Leippe investigated the antimicrobial and hemolytic activity as well as the cytotoxicity of two peptides namely NK-1 and NK-2 derived from the cationic core region of NK-lysin [140]. Thereby they synthesized the

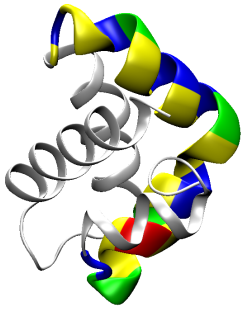

Figure 1.12: The NK-2 peptide highlighted as part of the NK-lysin protein. Polar residues are coloured in green, non-polar residues as yellow, anionic residues as red and cationic residues as blue.

NK-2 peptide by extracting the residues 39 to 65 from NK-lysin which corresponds to its third and fourth helix. The residues Leu6, Ser13 and Trp20 are point mutated by valine, tyrosine and lysine, respectively. The C-terminus is amidated. This results in an amphipathic peptide with a net charge of $+10\,\mathrm{e}$. Whereas the peptide is unstructured in buffer or water solution it adopts α-helical conformations in membrane mimicking environments, namely micellar solutions of anionic, cationic or non-ionic amphiphiles, trifluoroethanol (TFE) or at the air-buffer-interface [141, 142]. Experimental studies of the interaction of NK-2 with liposomes suggest that the selectivity of NK-2 is based on the difference in lipid compositions of eu- and prokaryotic cytoplasmic membranes [143, 144]. NK-2 interacts with zwitterionic phosphatidylethanolamine

[6] The term T-cells arises as they originate in the thymus

(PE) and much more strongly with anionic phosphatidylglycerol (PG) lipids, both contained in the outer leaflet of prokaryotic cell membranes. On the other hand, the outer leaflet of eukaryotic cell membranes contains mainly zwitterionic phosphatidylcholine (PC) lipids to which NK-2 has a low affinity. The affinity of the cationic peptide for zwitterionic PE lipids suggest that the adsorption process is not exclusively driven by charge complementary. This founding was confirmed by von Deuster and Knecht [145, 146]. They determined the free energy for the transfer of NK-2 monomers from palmitoyloleoylphosphatidylcholine (POPC) to palmitoyloleoylphosphatidylethanolamine (POPE) as well as palmitoyloleoylphosphatidylglycerol (POPG) bilayers by means of coarse grained MD simulations in combination with the thermodynamic integration (TI) method [145, 146]. POPC and POPE lipids are zwitterionic whereas POPG lipids have a negative net charge. Their results confirm that besides electrostatic peptide attraction other effects like the release of counter ions or the peptide mediated perturbation of lipid-lipid interactions might be crucial for the adsorption propensity.

2

Methods

In this chapter employed simulation and analysis techniques are described. First molecular dynamics (MD) simulation in general and subsequently the umbrella sampling as well as the thermodynamic integration (TI) method are explicated in sections 2.1, 2.2, and 2.3, respectively. Finally, in section 2.4 we present analysis methods to investigate lipid order parameters as well as secondary structures and peptide conformation clusters.

2.1 Molecular dynamics

Molecular dynamics (MD) simulations provide a powerful tool to study biomolecular processes like polypeptide folding, peptide-membrane adhesion, lipid membrane, and micelle formation as well as protein-ligand, DNA-ligand or protein-DNA complexation. As these processes involve typically energies of $1-10\,k_{\mathrm{B}}T$ at physiological temperatures they can sufficiently be described by *classical* mechanics. Newton's second law determines the dynamics of an N atom system by the equations of motion

$$m_i \frac{\partial^2 \mathbf{r_i}}{\partial t^2} = \mathbf{F_i} \quad i = 1,2,\cdots,N. \tag{2.1}$$

Here, $\mathbf{r_i}$ is the position of the ith nucleus whereas electrons are assumed to remain in their ground state. The electrons are assumed to follow the nuclei motions instantaneously. This so-called *Born-Oppenheimer*-approximation is

justified due to the much lower electron mass compared to the nuclei masses. As a consequence, the electronic ground state for given nuclei positions yields the effective potential governing the motion of the nuclei. The force $\mathbf{F}_i = \mathbf{F}_i(\mathbf{r_1}, \mathbf{r_2}, \cdots, \mathbf{r_N})$ on the ith nuclei is given by the negative gradient of the potential $V = V(\mathbf{r_1}, \mathbf{r_2}, \cdots, \mathbf{r_N})$, i. e.

$$\mathbf{F_i} = -\nabla_i V \qquad i = 1, 2, \cdots, N. \tag{2.2}$$

Here, $\nabla_i = (\partial/\partial x_i, \partial/\partial y_i, \partial/\partial z_i)$. After choosing the initial atom positions and velocities which are commonly set to zero or obtained from a Maxwell-Boltzmann distribution at a given temperature T the forces are computed via equation 2.2. If the potential energy of the initial system configuration resides rather far away from a local minimum a MD simulation may fail due to extraordinary large forces as apparent from equation 2.2. This effect might for example occur if atoms strongly overlap. To overcome this shortcoming the system is first relaxed to a local energy minimum. In our simulations we employed the *steepest decent* method which changes the configuration of the system in direction of the negative gradient of the potential, i.e. the force, until a local minimum is reached. Starting from the initial configuration equation 2.1 is integrated numerically in small time steps Δt using methods like the *velocity Verlet* or the *leap frog* algorithm [147, 148]. The latter is typically used in the GROMACS[1] simulation package and computes the atom positions at times $t + \Delta t$ and the velocities at times $t + \Delta t/2$ which accounts for the term *leap-frog* algorithm.
Interactions between atoms as occurring in the equations of motion are either bonded (covalent) or non-bonded. The latter determine to a large extend the computing time and are described by the Coulomb-Potential accounting for electrostatic interactions between charged particles,

$$V_{\mathrm{C}} = \sum_{i<j} \frac{1}{4\pi\varepsilon_0\varepsilon_r} \frac{q_i q_j}{r_{ij}}, \tag{2.3}$$

and the Lennard-Jones-potential approximating London dispersion as well as short-range Pauli repulsion according to

$$V_{\mathrm{LJ}} = \sum_{i<j} \frac{C_{ij}^{(12)}}{r_{ij}^{12}} - \frac{C_{ij}^{(6)}}{r_{ij}^{6}}. \tag{2.4}$$

Here, ε_0 is the vacuum permittivity, ε_r the dielectric constant with $\varepsilon_r = 1$ for explicit solvents, r_{ij} the distance between two particles i and j with the partial charges $q_{i,j}$, and $C_{ij}^{(12)}$ and $C_{ij}^{(6)}$ are the Lennard-Jones parameters.

[1] **GRO**ningen **MA**chine for **C**hemical **S**imulations

Bonded interactions comprise interactions between two, three or four atoms and are except for dihedral angles described by harmonic functions. The stretching along the axis connecting two bonded particles at an equilibrium bond length d_i^0 is described by the potential

$$V_\mathrm{b} = \sum_{i=1}^{N_\mathrm{b}} \frac{k_i^\mathrm{b}}{2} \left(d_i - d_i^0\right)^2 \tag{2.5}$$

whereas the bond angle potential is given by

$$V_\theta = \sum_{i=1}^{N_\theta} \frac{k_i^\theta}{2} \left(\theta_i - \theta_i^0\right)^2. \tag{2.6}$$

Here, θ_i^0 is the reference angle. The potential associated with the torsion of proper dihedral angles between two planes spanned by three non-planar bonds is described by

$$V_\Phi = \sum_{i=1}^{N_\Phi} \frac{k_i^\Phi}{2} \left(1 + \cos\left(n\Phi_i - \Phi_i^0\right)\right) \tag{2.7}$$

with the reference dihedral angle Φ_i^0 and $n = 1, 2, ...$ Improper dihedral angle potentials expressed as

$$V_\zeta = \sum_{i=1}^{N_\zeta} \frac{k^\zeta}{2} \left(\zeta_i - \zeta_i^0\right)^2 \tag{2.8}$$

with the equilibrium angle ζ_i^0 are employed to avoid for example the out of plane bending of aromatic rings or to conserve tetrahedral structures. The summation in equations 2.5 to 2.8 runs over all N_b covalent bonds, N_θ bond angles θ, N_Φ dihedral angles Φ, or N_ζ improper dihedral angles ζ, respectively.
The set of interaction functions comprising the force constants, reference angles or distances, partial charges, and Lennard-Jones parameters in equations 2.5 to 2.8 as well as 2.3 and 2.4 for all combinations of interatomic interactions provide a so-called force field. Force fields can be categorized into all-atom, united-atom, and coarse grained descriptions. In the first case all atoms are represented explicitly whereas in the united-atom force field non-polar hydrogen atoms are described by treating CH, CH_2, and CH_3 groups as single particles. Coarse grained force fields treat functional groups of multiple atoms as single interaction beads to describe a system. Corresponding force field parameters can be obtained by *ab initio* quantum chemistry calculations or by experiments providing macroscopic quantities like dielectric permittivities, diffusion, and viscosity coefficients, heats of vaporization, free energies of solvation or structural and dynamic properties including crystal structures or vibrational frequencies.

In general, force field parameters are inferred from rather small molecules as for these data are easier accessible and the derived parameters are transferable to a wider range of molecular species. Popular force fields for biomolecular systems comprise the all- and united-atom OPLS[2] [149], CHARMM[3] [150], AMBER[4] [151] and GROMOS [5] [152] as well as the MARTINI[6] coarse grain force field [153].
Although MD simulations complement and enlarge experimental findings to a large extend some shortcomings or inaccuracies associated with MD simulations may occur. This includes the negligence of quantum effects which have to be taken into account for the description of chemical reactions, relatively light particles like hydrogens or protons able to tunnel through potential barriers, or for high frequency covalent bonds with $h\nu \gtrsim k_{\mathrm{B}}T$. Here, ν is the resonance frequency of the bond and h the Planck constant. To minimize artifacts from the classical treatment as well as for computational efficiency, bond lengths are often fixed using the SHAKE or the LINCS[7] algorithm [154, 155]. Furthermore, finite size effects arising due to the relatively small sample size of typically 10^5 to 10^6 atoms considered in MD studies might cause inaccuracies in the derivation of macroscopic quantities valid for numbers of particles comparable to the Avogadro constant. This effect can partly be compensated by surrounding the simulation box under study by an infinite number of copies of itself which provides periodic boundary conditions. To investigate macroscopic properties from a MD simulation the trajectory of the system has to sample all relevant parts of the phase space sufficiently which might not necessarily be achieved during accessible computation times. This especially holds true if the free energy landscape of the system is rather rough and features comparably high barriers. This sampling problem might be overcome by advanced techniques like the replica exchange, umbrella sampling or thermodynamic integration method. The latter two are explained in more detail in the following two sections.

[2] **O**ptimized **P**otential for **L**iquid **S**imulations
[3] **C**hemistry at **HAR**vard **M**olecular **M**echanics
[4] **A**ssisted **M**odel **B**uilding with **E**nergy **R**efinement
[5] **GRO**ningen **MO**lecular **S**imulations
[6] Named after a cocktail and the nickname for the city of Groningen
[7] **LIN**ear **C**onstraint **S**olver

2.2 Umbrella sampling

The umbrella sampling technique is based on the potential of mean (PMF) first introduced by Kirkwood in 1935 [156]. The PMF describes the free energy change of a system along a reaction coordinate $\lambda(q_1...q_N)$ which can be a distance between two particles, an angle or a more complicated function of the generalized coordinates $q_1...q_N$. The averaged probability density, $\langle p(\lambda)\rangle$, that $\lambda(q_1...q_N)$ adopts a certain value $\lambda(q_1...q_N)=\lambda$ can be described by

$$\langle p(\lambda)\rangle = \frac{\int \delta(\lambda'(q_1...q_N)-\lambda)\exp(-\beta U(q_1...q_N))\,dq_1...dq_N}{\int \exp(-\beta U(q_1...q_N))\,dq_1...dq_N}. \tag{2.9}$$

Here, $\beta = 1/(k_B T)$ is defined by the Boltzmann constant k_B and the temperature T while $U(q_1...q_N)$ is the potential energy of the system and $\delta(\cdot)$ denotes the Dirac delta function. The integral runs over the complete configuration space. The PMF $\mathscr{W}(\lambda)$ with respect to an arbitrary reference reaction coordinate λ^* can be obtained from

$$\mathscr{W}(\lambda) = \mathscr{W}(\lambda^*) - k_B T \log\left[\frac{\langle p(\lambda)\rangle}{\langle p(\lambda^*)\rangle}\right].$$

A sufficient sampling of the configuration space along the reaction coordinate λ is often hindered by large free energy barriers which makes it impossible to determine $\langle p(\lambda)\rangle$ within reasonable simulation times. An approach to overcome this issue is provided by the umbrella sampling technique proposed by Torrie and Valleau [157]. In this method the potenial of the system is biased by an additional potential which leads to a change of the potential energy $U(q_1...q_N) \rightarrow U(q_1...q_N) + \mathscr{w}_i(\lambda)$. The additional bias potential effects a confinement of the system in a configuration space region of interest according to a particular λ_i. The complete path along λ is divided into several windows each corresponding to a value λ_i. Often the bias potential is chosen as a harmonic potential $\mathscr{w}_i(\lambda) = \frac{k}{2}(\lambda-\lambda_i)^2$ with the force constant k. According to equation 2.9 the unbiased averaged distribution function $\langle p(\lambda)\rangle_i^{\text{unbias}}$ for the ith umbrella window can be determined from the corresponding biased distribution function via

$$\langle p(\lambda)\rangle_i^{\text{unbias}} = \exp(\beta \mathscr{w}_i(\lambda))\,\langle p(\lambda)\rangle_i^{\text{bias}} \langle \exp(-\beta \mathscr{w}_i(\lambda))\rangle. \tag{2.10}$$

In combination with equation 2.2 this leads to the unbiased PMF

$$\mathscr{W}_i^{\text{unbias}}(\lambda) = \mathscr{W}(\lambda^*) - k_B T \log\left[\frac{\langle p(\lambda)\rangle_i^{\text{bias}}}{\langle p(\lambda^*)\rangle}\right] - \mathscr{w}_i(\lambda) + G_i.$$

including the free energy constant G_i which is determined from

$$\exp(-\beta G_i) = \langle \exp\left(-\beta \mathscr{W}_i(\lambda)\right) \rangle$$

and associated with the introduction of the bias potential $\mathscr{W}_i(\lambda)$. The information of all umbrella simulations has to be combined in order to construct the unbiased distribution function $\langle p(\lambda) \rangle$ along the whole path of the reaction coordinate λ. A very effective approach is provided by the weighted histogram analysis method (WHAM) proposed by Kumar *et al.* in 1992 [158]. The method is similar to the Bennett acceptance method [159] presented in section 2.3 and based on the histogram method suggested by Ferrenberg and Swendsen [160]. Its central idea is to estimate $\langle p(\lambda) \rangle$ by a sum of the weighted unbiased averaged distribution functions $\langle p(\lambda) \rangle_i^{\text{unbias}}$ determined by equation 2.10 and obtained from restrained simulations. The weighting factors are optimized such as to minimize the statistical error. In this way Kumar *et al.* obtained

$$\langle p(\lambda) \rangle = \frac{\sum_{i=1}^{N_W} n_i \langle p(\lambda) \rangle_i^{\text{bias}}}{\sum_{j=1}^{N_W} n_j \exp\left(-\beta \left(\mathscr{W}_j(\lambda) - G_j\right)\right)}. \tag{2.11}$$

Here, N_W denotes the number of umbrella windows and n_i the number of independent data points used to construct the biased distribution function $\langle p(\lambda) \rangle_i^{\text{bias}}$. The free energy constant G_i is determined by

$$\exp(-\beta G_i) = \int d\lambda \exp\left(-\beta \mathscr{W}_i(\lambda)\right) \langle p(\lambda) \rangle \tag{2.12}$$

As G_i depends on $\langle p(\lambda) \rangle$ the two equations 2.11 and 2.12 have to be solved iteratively until self consistency is reached. The WHAM method is implemented as g_wham in the GROMACS software package [161].

2.3 Thermodynamic integration

By means of the thermodynamic integration (TI) method the free energy difference between two system states or even between two different systems is estimated by integrating over the work required to go along a reversible pathway from an initial to a final state. In simulations this pathway can also be non-physical.

The difference in the Gibbs free energy, ΔG, between two systems B and A described by the Hamiltonian functions H_{B} and H_{A}, respectively, may be calcu-

lated via

$$\Delta G = \Delta G_{\mathrm{B}} - \Delta G_{\mathrm{A}} = \int_0^1 d\lambda \frac{\delta G}{\delta \lambda} = \int_0^1 d\lambda \left\langle \frac{\delta H}{\delta \lambda} \right\rangle_{\lambda}. \tag{2.13}$$

Hereby the Hamiltonian function $H(\lambda)$ depending on the continuous coupling parameter $\lambda = [0,1]$ is a superposition of the Hamiltonian functions of both systems with $H(\lambda) \to H_{\mathrm{A}}$ for $\lambda \to 0$ as well as $H(\lambda) \to H_{\mathrm{B}}$ for $\lambda \to 1$. This holds true for the choice

$$H(\lambda) = (1-\lambda) \cdot H_{\mathrm{A}} + \lambda \cdot H_{\mathrm{B}}. \tag{2.14}$$

Equation 2.13 goes back to Kirkwood in 1935 [156] and provides the basis of the thermodynamic integration (TI) methods. The brackets $\langle \cdot \rangle_{\lambda}$ refer to a thermodynamic average corresponding to a particular coupling parameter λ. In practice this parameter is varied in discrete steps.
A very efficient way to compute the free energy difference between two systems 1 and 2 via their potential energy U_1 and U_2 is provided by the Bennett acceptance ratio method [159] according to

$$\Delta G_{12} = -k_{\mathrm{B}} T \log \frac{Q_1}{Q_2} = -k_{\mathrm{B}} T \log \left(\frac{\langle W \exp(-\beta U_1) \rangle_2}{\langle W \exp(-\beta U_2) \rangle_1} \right). \tag{2.15}$$

Here, the brackets $\langle \cdot \rangle_1$ and $\langle \cdot \rangle_2$ denote a thermodynamic average over system 1 and system 2, respectively, whereas Q_1 and Q_2 represent the corresponding configurational integrals,

$$Q_i = \int \exp\left(\frac{-U_i(q_1, ..., q_N)}{k_{\mathrm{B}} T} \right) dq_1 ... dq_N \quad \text{with } i = 1,2. \tag{2.16}$$

The potential energies $U_i(q_1, ..., q_N)$ depend on the N configurational degrees of freedom $q_1 ... q_N$ of the system and the integration runs over the complete configuration space. Bennett optimized the weighting function $W \hat{=} W(q_1 ... q_N)$ by means of variational calculus in order to minimize the variance of the free energy difference ΔG_{12}. Especially for rather poor overlap between the phase spaces of system 1 and 2 and if the slope of $\frac{\delta G}{\delta \lambda}$ is rather rough, the Bennett acceptance ratio method provides higher accuracy than the thermodynamic integration method [162].
To determine the difference in binding free energies $\Delta\Delta G = \Delta G_{\mathrm{PG}} - \Delta G_{\mathrm{PC}}$ for the association of the NK-2 peptide with anionic DOPG and zwitterionic DOPC bilayers the thermodynamic cycle shown in figure 2.1 was applied. As the Gibbs

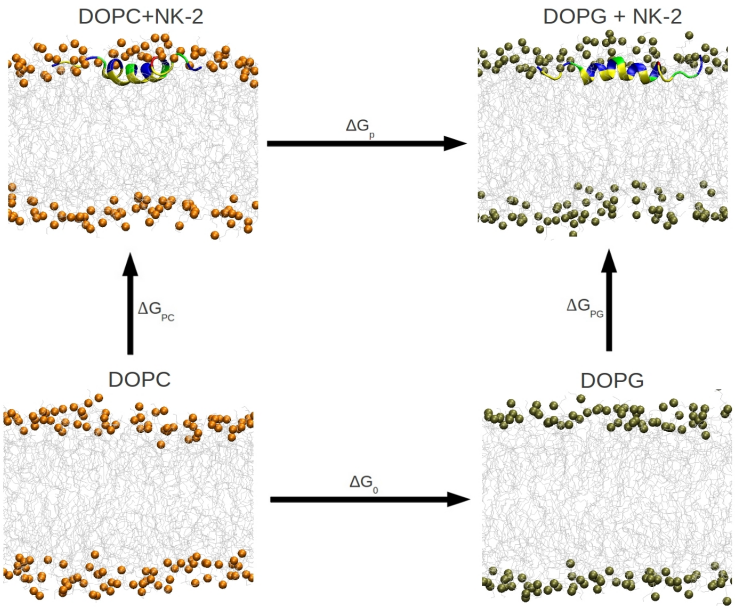

Figure 2.1: Thermodynamic cycle to compute the difference in the affinity of the NK-2 peptide for an anionic DOPG and a zwitterionic DOPC bilayer. Carbon tails are presented in grey and nitrogens of the phosphocholine (PC) headgroup in orange. The latter, as described in section 2.3.1, transformed into oxygens of the phosphoglycerol (PG) headgroup which are depicted in tan. For the peptide, colours distinguish between hydrophilic (green), hydrophobic (yellow), cationic (blue), and anionic (red). The snapshots where taken after 100 ns of simulation.

free energy is a state function the relation

$$\Delta G_0 + \Delta G_{\mathrm{PG}} = \Delta G_{\mathrm{PC}} + \Delta G_{\mathrm{P}}$$

and therefore

$$\Delta\Delta G = \Delta G_{\mathrm{P}} - \Delta G_0$$

holds. Hence, the desired free energy difference $\Delta\Delta G$ may be computed from the free energy changes ΔG_0 and ΔG_{P} upon the alchemical transformation of DOPC to DOPG in absence and presence of NK-2.
In this work, the free energy differences ΔG_0 and ΔG_{P} were determined using thermodynamic integration according to equation 2.13. The step size of λ was chosen as $\Delta\lambda = 0.05$ for $\lambda \in [0.1, 0.9]$ whereas $\Delta\lambda = 0.01$ was applied for $\lambda \in [0, 0.1]$ as well as for $\lambda \in [0.9, 1.0]$. The smaller step size for $\lambda \to 0$ and $\lambda \to 1$ was necessary due to appearing and vanishing atoms, so-called dummy atoms, involved in the performed alchemical transformation. These dummy atoms are

described in more detail in section 2.3.1.

2.3.1 Dummy atoms and soft-core-potential

To transform a DOPC to a DOPG lipid merely the phosphocholine (PC) headgroup has to be converted into a phosphoglycerol (PG) headgroup whereas the hydrocarbon tails remain unchanged. Therefore several atomic species have to be replaced by others as shown in figure 2.2. As the lipid headgroups differ in the number of atoms and in the binding structure some atoms have to be created or annihilated during the alchemical transformation. This is achieved by so-called dummy atoms. In one of the two states ($\lambda = 0$ or $\lambda = 1$) these dummy atoms can be considered as mass points assuming neither Lennard-Jones nor Coulomb interactions with other particles of the system. The weight of both interaction terms increases due to the transformation of the Hamiltonian to the other state. The Coulomb interaction between two particles i and j is described

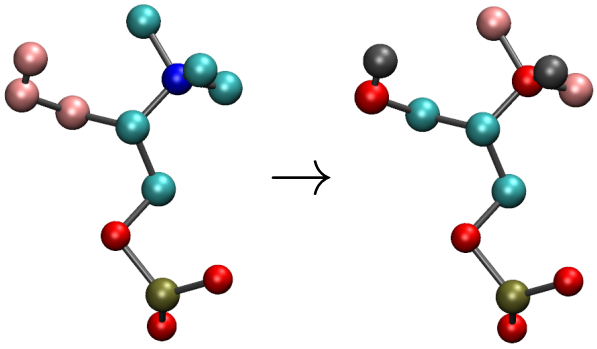

Figure 2.2: The alchemical transformation of the phosphocholine (PC, *left*) of DOPC to the phosphoglycerol (PG, *right*) headgroup of DOPG. Carbon atoms are shown as cyan, oxygen as red, nitrogen as blue, phosphor as tan, and dummy atoms as pink spheres. Transformed hydrogens are coloured dark grey.

by the potential

$$V_{\mathrm{C}}(\lambda) = \frac{1}{4\pi\varepsilon_0\varepsilon_r r_{ij}}\left[(1-\lambda)\,q_i^{\mathrm{A}}q_j^{\mathrm{A}} + \lambda q_i^{\mathrm{B}}q_j^{\mathrm{B}}\right] \tag{2.17}$$

Here ε_0 is the vacuum permittivity, $\varepsilon_r = 1$ (explicit solvent) the dielectric constant, $q_{i,j}^{\mathrm{A,B}}$ the charge of particle i or j in system A or B, and r_{ij} the distance between the particles. The Lennard-Jones potential features an attractive and a repulsive part and is given by

$$V_{\mathrm{LJ}}(\lambda) = \frac{(1-\lambda)\,C_{\mathrm{A},ij}^{(12)} + \lambda C_{\mathrm{B},ij}^{(12)}}{r_{ij}^{12}} - \frac{(1-\lambda)\,C_{\mathrm{A},ij}^{(6)} + \lambda C_{\mathrm{B}}^{(6)}, ij}{r_{ij}^{6}} \tag{2.18}$$

The $C^{(6)}$ and $C^{(12)}$ coefficients are characteristic for each atom type and obtained from quantum mechanical calculations ($C^{(6)}$) or fits to experimental data ($C^{(12)}$). For the interaction between two atoms of different types, combination rules are usually applied. For weak Lennard-Jones interactions, dummy atoms might come very close to other particles of the system. Increasing the weight of the Coulomb and Lennard-Jones interaction terms simultaneously might therefore lead to extraordinarily high attractive forces leading to unstable simulation runs. Hence, two separate simulations are necessary. In the first alchemical transformation, only the Lennard-Jones potentials of the dummy atoms are turned on (no potential $\rightarrow$ Lennard-Jones potential) and in the second transformation, Coulomb potentials are added (Lennard-Jones potential $\rightarrow$ Lennard-Jones and Coulomb potential).
As the Lennard-Jones and the Coulomb interaction terms given in equation 2.18 and 2.17 depend linearly on λ, the corresponding partial derivatives $\delta V/\delta\lambda$ are independent of the coupling parameter λ. For small distances between the particles ($r_{ij} \rightarrow 0$) as it might occur for appearing and vanishing atoms ($\lambda \rightarrow 0$ and $\lambda \rightarrow 1$) this leads to large fluctuations in $\delta V/\delta\lambda$ during the simulations. According to equation 2.13 and due to the fact that the Hamiltonian function is given by the sum of the potential and kinetic energy, large statistical uncertainties in the free energy calculations have to be expected [163]. To overcome this issue, for $0 < \lambda < 1$ the Lennard-Jones and Coulomb potentials are replaced by so-called soft-core potentials

$$\begin{aligned} V_{\mathrm{SC}} &= (1-\lambda)\, V^{\mathrm{A}}\left(r_{ij}^{\mathrm{A}}\right) + \lambda V^{\mathrm{B}}\left(r_{ij}^{\mathrm{B}}\right) \\ r_{ij}^{\mathrm{A}} &= \left(\alpha\sigma_{\mathrm{A}}^{6}\lambda^{p} + r_{ij}^{6}\right)^{\frac{1}{6}} \\ r_{ij}^{\mathrm{B}} &= \left(\alpha\sigma_{\mathrm{B}}^{6}\,(1-\lambda)^{p} + r_{ij}^{6}\right)^{\frac{1}{6}} \end{aligned} \tag{2.19}$$

Here $V^{\mathrm{A}}\left(r_{ij}^{\mathrm{A}}\right)$ and $V^{\mathrm{B}}\left(r_{ij}^{\mathrm{B}}\right)$ are the Lennard-Jones and Coulomb potentials given in equation 2.18 and 2.17, whereas the distances between the particles r_{ij} are shifted depending on λ. In this way the derivative $\delta V_{\mathrm{SC}}/\delta\lambda$ still depends on λ and the singularities for $r_{ij} \rightarrow 0$ are avoided. The radius of interaction σ is given by $\left(C^{(12)}/C^{(6)}\right)^{1/6}$ if these coefficients do not vanish. Otherwise it is given by an input parameter which is often chosen to be $\sigma = 0.3$ nm. The soft-core power p was originally set to $p = 2$ [163] whereas $p = 1$ might lead to better results due to a smoother shape of $\delta H(\lambda)/\delta\lambda$. If atoms have to be annihilated and created, the soft-core parameter should be $\alpha \approx 0.7$ for $p = 1$ or $\alpha \approx 1.5$ for $p = 2$ to obtain reasonable accuracies. In our simulations $\alpha = 0.5$ and $p = 1$ was used. This choice was validated by performing the alchemical transformation from DOPC to DOPG in steps of $\Delta\lambda = 0.5$ for a single lipid solvated in

SPC[8] water [164]. Here we compared the statistical uncertainties in the free energy differences for the parameter combinations $p = 1$ and $\alpha = 0.5 - 0.8$ as well as $p = 2$ and $\alpha = 1.4 - 1.6$. For each value of λ, data were collected from two 10 ns simulations according to the separated transformations of Lennard-Jones and Coulomb interactions. For each λ value the system was first energy minimized using the steepest descent method and subsequently equilibrated for 1 ns.

2.4 Analysis methods

2.4.1 Lipid order parameters

The order of lipid bilayer hydrocarbon tails is measured by the parameters

$$S_z^n = \frac{3}{2}\left\langle \cos^2 \Theta_z^n \right\rangle - \frac{1}{2}. \tag{2.20}$$

In this study only the denoted z-component of the order parameter was considered. The x- and y-components are defined in a similar way. The brackets correspond to an average over simulation time as well as molecules while Θ_z^n is the angle between the bilayer normal and the vector connecting the carbon atoms C_{n-1} and C_{n+1}. Whereas S_z^n vanishes for isotropic orientations it adopts the value -1/2 if all carbon atoms are parallel orientated to the bilayer surface, and $S_z^n = 1$ if they are perpendicular orientated. Order parameters were determined using the script g_order from the GROMACS software package [165–167].

2.4.2 Secondary structure of peptides: DSSP

In 1983 Kabsch and Sander proposed the rather simple but effective DSSP [9] method to categorize the up to then over 100 known protein structures by means of hydrogen bond patterns and geometrical aspects [168]. First the structure is searched for hydrogen bonds within the main chain by determining the Coulomb interaction between partially charged CO $(+q_1, -q_2)$ and NH $(-q_1, +q_2)$ groups via

$$V = \frac{q_1 q_2}{4\pi\varepsilon_0}\left(\frac{1}{r(\mathrm{ON})} + \frac{1}{r(\mathrm{CH})} - \frac{1}{r(\mathrm{OH})} - \frac{1}{r(\mathrm{CN})}\right).$$

Here, r denotes the distance between two atoms and ε_0 the vacuum permittivity. Partial charges are set to $q_1 = 0.42\,\mathrm{e}$ and $q_2 = 0.20\,\mathrm{e}$. Ideal hydro-

[8] **S**imple **P**oint **C**harge
[9] **D**efine **S**econdary **S**tructure of **P**roteins

gen bonds are characterized by a dipole-dipole distance of $d = 2.9$ Å and an alignment angle of $\theta = 0^\circ$ corresponding to an antiparallel orientation yielding $V \approx -3$ kcal/mole. To define hydrogen bonds, Kabsch and Sander chose a rather generous cut-off for the electrostatic potential. They assumed hydrogen bonds for $V \leq -0.5$ kcal/mole corresponding to alignment angles up to $\theta \leq 63^\circ$ at ideal distance and distances up to $d \leq 5.2$ Å at ideal alignment. In this way also bifurcated hydrogen bonds are taken into account. Based on hydrogen bonds so-called turns and β-bridges were defined. A n-turn corresponds to a hydrogen bond between residue i and $i+n$ with $n = 3,4,5$, and a β-bridge corresponds to two hydrogen bonds between two residue stretches $i-1,i,i+1$ and $j-1,j,j+1$ (strands). These strands can be parallel or antiparallel. Turns and bridges are the building blocks of higher structures, namely helices and β-sheets. A β-sheet consists of several consecutive β-bridges of identical type. The three different turn types can also form three different kinds of helices. Accordingly, 3_{10}, α, or π-helices contain at least two consecutive 3-, 4- or 5-turns, respectively. Bends are peptide segments of high curvature. They are defined by the angle between the first (i-2,i-1,i) and the last three residues (i,i+1,i+2) of a five residue peptide section. A segment is called a bend if the angle between these two segments is larger than 70°. In the GROMACS simulation package this algorithm is implemented as do_dssp [165–167].

2.4.3 Cluster analysis

Similar structures adopted by a peptide during a simulation run are clustered by a method proposed by Daura *et al.* based on the root mean square deviation (RMSD) of peptide structures [169]. The RMSD of a peptide structure at the time t_1 with respect to a reference structure at time t_2 is defined as

$$\mathrm{RMSD}(t_1,t_2) = \frac{1}{M}\sum_{i=1}^{N} m_i \left(\|\mathbf{r}_i(t_1) - \mathbf{r}_i(t_2)\|^2\right)^{1/2}. \tag{2.21}$$

Here, N is the number of atoms of the peptide, m_i is the mass of atom i, $\mathbf{r}_i$ its position, and $M = \sum_{i=1}^{N} m_i$ the mass of the peptide. Before evaluating equation 2.21 the structure at t_1 is fitted to the reference structure at t_2 by means of the least square method.

In the method proposed by Daura *et al.* first the $\mathrm{RMSD}(t_1,t_2)$ for all pairs of (t_1,t_2) is calculated and, subsequently, for each peptide structure, the number of neighbouring structures is counted. Here, two structures at t_1 and t_2 are considered as neighbours if the corresponding $\mathrm{RMSD}(t_1,t_2)$ is below a chosen cut-off value. The structure with the largest number of neighbours forms the center of the first cluster and all corresponding structures belong to this cluster. After re-

moving the structures of the first cluster from the complete pool of structures the second cluster is found in the same manner and so on.

3

Amyloid β: Peptide folding at an air-water-interface

A central question regarding Alzheimer's disease addresses the fact that the amyloid β peptide aggregates in the brain although it only occurs in relatively low concentrations. Whereas a peptide concentration in the micromolar range is required to induce fibril formation *in vitro* the peptide already aggregates at submicromolar concentrations *in vivo* [170–172]. Prevalently, it is assumed that this discrepancy might at least partly be caused by a cell membrane mediated increase of the peptide aggregation propensity *in vivo* [173, 174]. Circular dichroism spectroscopy (CD) experiments indicated that the presence of phospholipid vesicles exhibiting zwitterionic headgroups does not largely affect the peptide structure whereas phospholipid vesicles featuring anionic headgroups significantly increase the amount of β-sheet conformations even at low peptide concentrations comparable to *in vivo* conditions [170, 175].
Several mechanisms might play a role in membrane mediated peptide aggregation: (i) formation of aggregation prone monomer structures, (ii) increase of peptide concentration due to the lower dimension or local peptide attracting inhomogeneities, (iii) alignment of the peptide to aggregation favouring orientations, and (iv) local environmental changes in the vicinity of membranes [174]. The latter may for example arise due to the presence of anionic lipids whose negative headgroup charge attracts cations which results in a decrease in the local pH. Accordingly, slightly acidic environments have been reported to increase the oligomerization, aggregation, and neurotoxicity of Aβ

peptides [176–178]. Furthermore a change of the pH from neutral to slightly acidic in extracellular space has been reported to accompany Alzheimer's disease [86].
In this chapter we investigate the influence of air-water-interfaces on the early steps of Aβ_{40} and Aβ_{42} peptide folding under physiological as well as slightly acidic environments mimicking conditions. The two major alloforms of the Aβ peptide show different aggregation behaviours as described in section 1.3.2 of the introduction. Air-water-interfaces serve as hydrophobic/hydrophilic model systems for biological membranes which allow a relatively fast sampling of the peptides' configurational space due to the lack of lipid-peptide-interactions. We investigated peptide folding on a time scale of 2 μs by means of molecular dynamics (MD) simulations. The required time t in nanoseconds to find the peptides' native or equilibrium state can be roughly estimated from the number of residues N (with $N \leq 100$) [179] according to

$$\exp\left(\frac{N^{2/3}}{2}\right) \leq t \leq \exp\left(\frac{3N^{2/3}}{2}\right).$$

For Aβ_{40} and Aβ_{42} we obtain 347 ns $\leq t \leq$ 42 ms and 420 ns $\leq t \leq$ 74 ms, respectively. Hence, we address rather early steps of peptide folding by our simulations. On the other hand, MD simulations of the Aβ_{40} and Aβ_{42} monomer on the 1.5 μs time scale have been shown to reproduce chemical shifts obtained from NMR spectroscopy. This suggests that the Aβ monomer long-term structure can sufficiently be described by μs-simulations [85, 91].

3.1 Simulation setup

The simulations described in this chapter are summarized in diagram 3.1. To imitate the peptides' folding behaviour directly after release from the membrane the initial configuration of both peptides was chosen as to exhibit mainly helical motifs adopted under conditions mimicking water-membrane-interfaces or membrane core environments. Accordingly, the initial structure of the Aβ_{40} peptide was obtained from NMR spectroscopy in aqueous sodium dodecyl sulphate (SDS) micelles at slightly acidic pH [98] whereas the initial structure of Aβ_{42} was obtained from NMR spectroscopy in a nonpolar water-hexafluoroisopropanol (HFIP) solution [97]. Both structures were downloaded from the RCSB[1] protein data bank (PDB entries: 1BA4 for Aβ_{40} and 1Z0Q for Aβ_{42}) [180]. The N-termini of the peptides contain the three histidine residues His6, His13, and His14 whose protonation states are strongly affected by the

[1] **R**esearch **C**ollaboraty for **S**tructural **B**ioinformatics

pH. To mimic physiological conditions corresponding to pH 7.4 the histidine residues were modelled neutral with only one of the imidazolyl nitrogens protonated resulting in a peptide net charge of -3 e. The protonation of both imidazolyl nitrogens of each histidine residue leads to a zero net charge of the peptide in slightly acidic environments ($4 < \mathrm{pH} < 7$) [85]. Each peptide was simulated at both of these histidine protonation states. Hereby glutamic and aspartic acid residues were modelled as deprotonated (negatively charged) and arginine as well as lysine residues as positively charged.

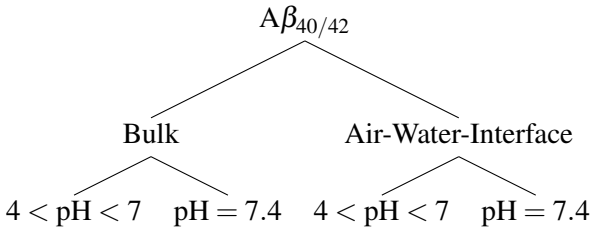

Table 3.1: Systems simulated to study the folding of Aβ_{40} and Aβ_{42} at various conditions.

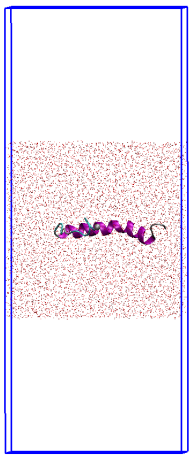

Figure 3.1: Initial configuration of the Aβ_{40} monomer at an air-water-interface.

Each peptide was centered in a simulation box with an initial size of 6.5^3 nm^3 and solvated with 8870 explicit SPC[2] water molecules [164]. Subsequently, Na^+ and Cl^- counter- and co-ions were added in order to obtain an electrical neutral system with a physiological NaCl concentration of 100 mM. The energy of the system was minimized using the steepest descent method [181]. The aqueous NaCl solution was equilibrated via 1 ns NPT-simulations. To avoid non-equilibrium effects the peptide atoms were kept close to their initial position via a harmonic potential with a force constant of $1000\,\mathrm{kJ/(mol \cdot nm^2)}$ during the equilibration process. The set-ups for the air-water-interface simulations were obtained by extending the simulation box in z-direction and subsequently recentering the water-peptide system in the simulation box as shown in figure 3.1.

In all simulations the peptide, ions, and water molecules were separately

[2] **S**imple **P**oint **C**harge

coupled to a velocity rescaling thermostat [182] with a relaxation time of 0.1 ps maintaining a temperature of $T = 300$ K. The simulations in bulk solution were performed at a constant pressure of 1 atm by coupling the system isotropically to a Berendsen barostat [183] with a relaxation time of 0.5 ps. Long-range electrostatic interactions were calculated using particle mesh Ewald (PME) summation [184, 185]. The peptides was described via the united-atom GROMOS96 force field ffG53a6 [186]. This force field has been shown to reproduce chemical shifts of HN, N, Cα, and Cβ atoms of the Aβ_{40} and Aβ_{42} peptide as obtained by NMR spectroscopy [85, 91].

3.2 Results

For all systems the secondary structure of the peptide was determined using the DSSP method [168] described in section 2.4.2 whereas similar conformational states adopted by the peptide during the sampling time were clustered using the method by Daura *et al.* [169] described in section 2.4.3. To this end, the final 1.5 μs of the 2 μs simulation runs were analyzed. The time course of the secondary structure for each residue is shown in the section A.1 of the appendix. During all simulations involving the presence of an air-water-interface the peptide attached to the interface within $10 - 25$ ns as illustrated for Aβ_{40} at neutral pH in figure 3.2 (*left*). Hereby the hydrophilic N-terminus is buried in the water phase whereas the hydrophobic C-terminus tends to face air. This holds true over the whole simulation time as indicated from the mass density profiles shown in figure 3.2 (*right*). In the following we describe the results for each Aβ_{40} system and subsequently compare the results with each other. After reporting the results

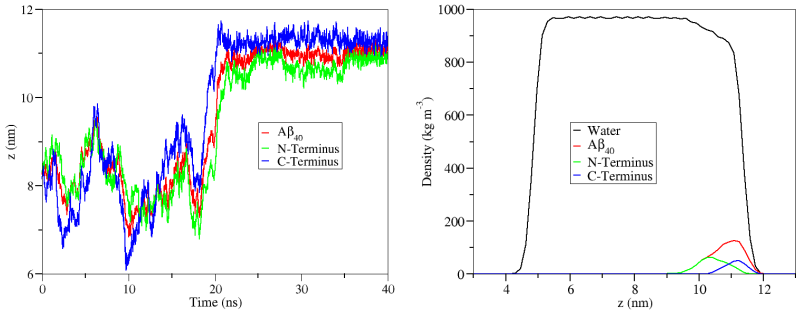

Figure 3.2: z-component of the center of mass for the first 40 ns as well as mass density profiles averaged over the final 100 ns of the 2 μs simulation for an Aβ_{40} peptide at an air-water-interface at neutral pH. The N-terminus corresponds to residues Asp1-Lys16 and the C-terminus to Gly29-Val40.

for Aβ_{42} in a similar manner we compare these with a related study performed by Olubiyi and Strodel [85]. We conclude with a discussion and the comparison of both peptides.

3.2.1 Aβ_{40}: Secondary structure and cluster analysis

The secondary structure content for each residue can be found in figure 3.4 whereas the most present hydrogen bonds as well as the coil and β-motif contents averaged over time are shown in table 3.2. Representatives of the three main clusters are depicted in figure 3.3 while the time evolution of the secondary structure for individual residues is presented in figures A.1 and A.2 attached to the appendix.

If Aβ_{40} is placed in a slightly acid bulk solution, its initial helical structure dissolves within 120 ns as shown in figure 3.5 (*left*). Whereas the hydrophilic N-terminal part consisting of residues Asp1 to Lys16 is mainly unstructured (figure 3.4) the hydrophobic core residues Leu17-Ala21 and residues Ile31-Met35 in the C-terminal region adopt a two-stranded β-sheet after around 500 ns as apparent from figure A.1 (*top*) of the appendix. These β-strands are parallel to each other and accompanied by a small antiparallel β-strand formed by residues Asn27 and Lys28. This β-strand and the C-terminal β-sheet are separated by a turn in residues Gly29 and Ala30 stabilized by hydrogen bonds between Lys28 and Ile31 (stable over 68% of the sampling time). The parallel β-sheet is stabilized by the most present hydrogen bonds between residues Phe19-Ile32, Leu34-Phe19 and Ala21-Leu34 listed in table 3.2. The described motif dominates the secondary structure during the sampling time as apparent from the content of secondary structure as well as the results of the cluster analysis shown in figure 3.4 (*top, left*) and figure 3.3 (*first row*), respectively.

At the surface of an acidic aqueous solution the initial N-terminal helix dissolves more quickly than in bulk water, namely after about 20 ns (figure 3.5 (*left*)). The peptide's secondary structure is dominated by bends or coils and its coil content averaged over sampling time is with 80% listed in table 3.2 comparably high. As in absence of an air-water-interface this holds especially true for the N-terminus. The peptide forms only a rather small number of stable hydrogen bonds. The only exception are two hydrogen bonds between Gly33 and Val18 as well as Phe20 and Ile31. These hydrogen bonds stabilize a β-bridge formed by residues Ile32 and Phe19 which arises after about 100 ns and extends after about 1.2 μs to a β-sheet covering mainly residues Leu17-Phe20 and Ile31-Leu34 as apparent from figure A.1 (*bottom*) of the appendix. This motif resembles the corresponding motif found for Aβ_{40} in acidic bulk solution

Aβ_{40} in bulk water at acidic pH: *575 clusters*

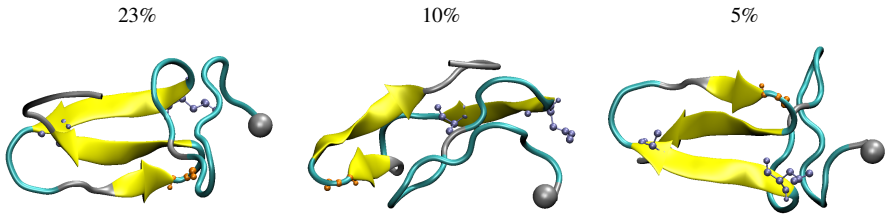

Aβ_{40} at an air-water-interface at acidic pH: *385 clusters*

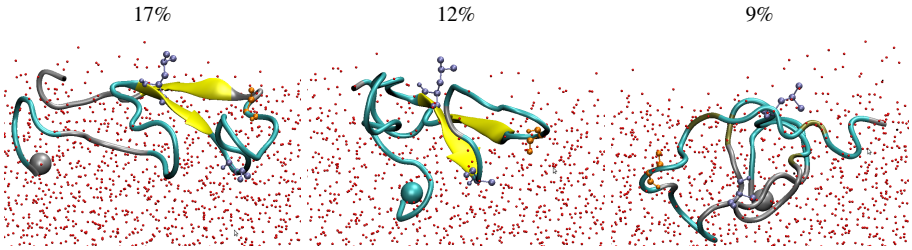

Aβ_{40} in bulk water at neutral pH: *1420 clusters*

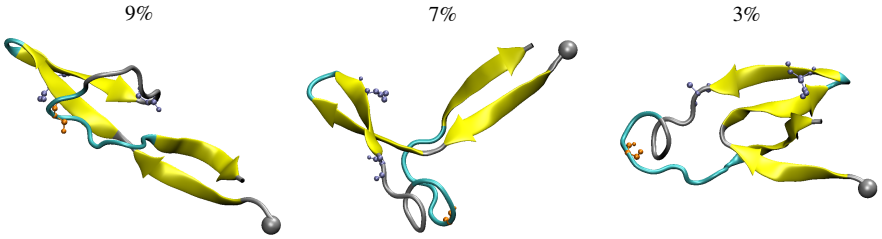

Aβ_{40} at an air-water-interface at neutral pH: *451 clusters*

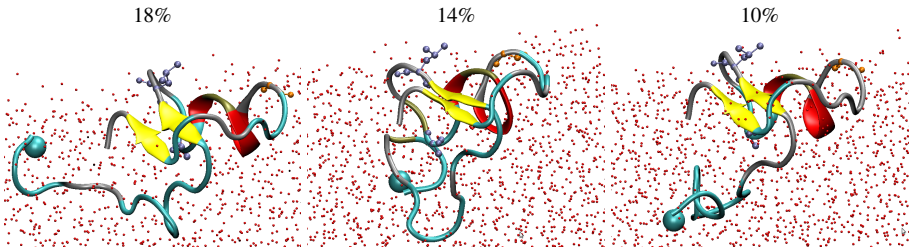

Figure 3.3: Three main conformations of Aβ_{40} at an air-water-interface and in bulk solution at slightly acidic and neutral pH as obtained from a cluster analysis of the final 1.5 μs of a 2 μs simulation. Peptides are represented as *ribbons* and C_α atoms of ASP1 as spheres. Residues are colored according to their secondary structure. Coil structures are represented in silver, turns in cyan, β-sheets in yellow, β-bridges in tan, α-helices in purple, and π-helices in red. Residues 17 and 21 marking the boundary of the hydrophobic core region are highlighted as ice blue spheres and sticks while residue 29 is colored orange to indicate the hydrophobic C-terminus. At the air-water-interface the oxygen atoms of the water molecules are displayed as red spheres. The air-water-interface is shown in side view.

and characterizes the first two main clusters shown in figure 3.3 (*second row*) as well as the secondary structure content of individual residues depicted in figure 3.4 (*top,right*).

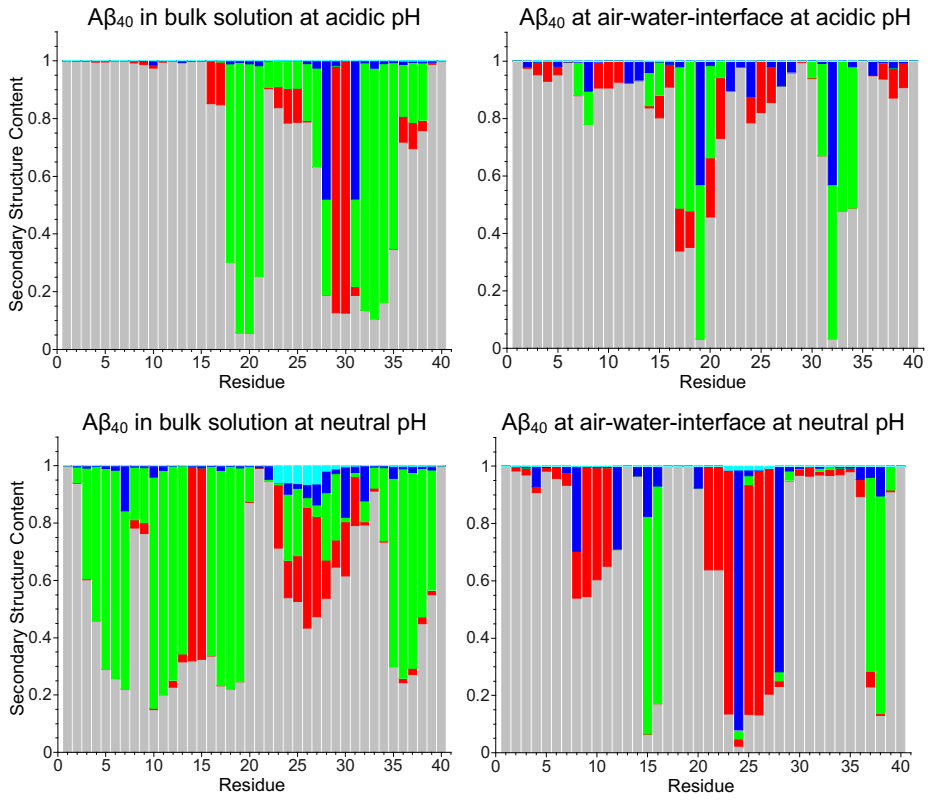

Figure 3.4: Content of secondary structure motifs during the final 1.5 μs of 2 μs simulations for individual residues of Aβ_{40} under various conditions. The corresponding time is given as fraction of the sampling time. Coils are represented in light gray, β-bridges in blue, β-sheets in green, turns in red and helices in cyan.

In pH neutral bulk solution the decay of the initial N-terminal helix is rather slow and takes nearly 500 ns (figure 3.5 (*left*)). A part of an initial C-terminal $\pi-$ or 5-helix, spanning the section Val24-Gly33, survives for about 750 ns (figure A.1 (*bottom*) of the appendix). It has to be noted that the DSSP program does not recognize this helix properly and interprets it as a pattern of turns and small β-sheets as evident from the time evolution of the secondary structure (figure A.2 (*top*) of the appendix). Visualization with the VMD[3] program [187] reveals the helical structure of this motif. The helix is thus not considered in

[3] **V**isual **M**olecular **D**ynamics

figure 3.5 (*left*) which rather shows the time evolution of the initial N-terminal helix as C-terminal helices either decay very fast or are not recognized properly. During the simulation the peptide assumes a large number of various structures as indicated by the large number of clusters (3.3 (*third row*)). These structures include many β-motifs. Interestingly, especially the C-terminus exhibits a stable sheet-turn-sheet motif arising after about 800 ns (figure A.2 (*top*) of the appendix). The two β-strands are antiparallel and span residues Gly9-Val12 and Lys16-Phe19 while a turn is located at His14 and Gln15. This motif is stabilized by mainchain hydrogen bonds between Glu11 and Val18 as well as Phe20 and Gly9 (table 3.2). In addition the residues Glu3-Asp7 and Met35-Val39 form a two-stranded antiparallel β-sheet. This motif arises after about 450 ns, survives for about 1250 ns (figure A.2 (*top*) of the appendix) and is stabilized by a hydrogen bond between Asp7 and Met35 (stable for 55% of the simulation time). Both described motifs dominate the two main clusters presented and also determine the secondary structure content in the corresponding residues as apparent from figure 3.3 (*third row*) and 3.4 (*bottom, left*), respectively. In contrast to the systems described before we thus observe that the hydrophobic core region forms β-sheets with the hydrophilic N-Terminus which furthermore adopts a β-sheet conformation with the hydrophobic C-Terminus.

At the surface of a pH neutral aqueous solution we observe that the N-terminal helix dissolves rather quickly after about 20 ns (figure 3.5 (*left*)) whereas a π-helix comprising residues Ser26-Met35 is present in the C-terminus for the first 500 ns (figure A.2 (*bottom*)). As in the case before this is not recognized by the DSSP method. During the sampling time a small parallel two-stranded β-sheet was found between Gly37-Gly38 and Gln15-Lys16, stabilized by a hydrogen bond between Lys16 and Gly37 shown in table 3.2. A small helix or turn-bridge-turn-bridge motif is adopted by the segment Asp23-Lys28. This motif is fixed to the aforementioned β-sheet by the hydrogen bond Val24-Gln15 (table 3.2). Both described motifs occur in the three main clusters depicted in figure 3.3 and determine the secondary structure content in figure 3.4 (*bottom, right*). In the latter the aforementioned helix in the residues Asp23-Lys28 occurs as turn-bridge-turn-bridge motif.

	Hydrogen Bonds			Secondary Structure	
	$> 60\%$	Bond	Durability	Coil	β-motifs
Bulk water at acidic pH	6	Phe19-Ile32 Leu34-Phe19 Ala21-Leu34	72% 71% 69%	$69 \pm 9\%$	$24 \pm 9\%$
Air-water at acidic pH	4	Gly33-Val18 Phe20-Ile31 His13-Asp7	93% 92% 65%	$80 \pm 9\%$	$15 \pm 11\%$
Bulk water at neutral pH	4	Glu11-Val18 Val18-Glu11 Phe20-Gly9	75% 71% 71%	$53 \pm 11\%$	$37 \pm 13\%$
Air-water at neutral pH	11	Val24-Gln15 Gly25-Lys28 Lys16-Gly37	81% 79% 77%	$70 \pm 9\%$	$15 \pm 6\%$

Table 3.2: Intramolecular hydrogen bonds and temporal structure content of Aβ_{40} in different environments. Data were collected from the final 1.5 μs of 2 μs simulations. Shown are the number of hydrogen bonds existing longer than 60% of the time, the three most common hydrogen bonds and their durability in terms of their content in time as well as the averaged percentage of coils and β-motifs. Hereby, „coil“denotes the sum of coil and bend content from the DSSP method. In the same way the sum of β-sheet and β-bridge content is denoted as „β-motif “.

Conclusion Aβ_{40}

Our simulation show that a slightly acidic environment leads to a destabilization of the initial helical structure. This holds especially true for the C-terminal helix in pH neutral environments. The position of the helix coincides with the threefold GlyXXXGly pattern located between the residues Gly25-Gly37 as described in section 1.3.2. Furthermore the peptide and especially the hydrophilic N-terminus assumes rather unstructured conformations at acidic pH as reflected by the coil content presented in table 3.2 and the secondary structure content depicted in figure 3.4. On the other hand, the number of different conformations and hence the number of clusters is larger in pH neutral environments which comes along with an increased β-sheet content in bulk solution (table 3.2). The latter does not hold true at an air-water-interface where the β-sheet content is rather not affected by the pH. In bulk solution and at an air-water-interface the tendency to form β-structures comprising N-terminal residues is increased at neutral compared to acidic conditions. This effect appears much stronger for the bulk systems. A more detailed analysis reveals that the histidine residues

	HIS hydrogen bonds	
	$> 10\%$	total
Bulk water at acidic pH	16	94
Air-water at acidic pH	20	177
Bulk water at neutral pH	5	157
Air-water at neutral pH	14	174

Table 3.3: Total number of hydrogen bonds and hydrogen bonds existing more than 10% of the sampling time involving histidine residues of the Aβ_{40} peptide.

which are especially affected by changes in pH form a larger number of hydrogen bonds existing longer than 10% of the sampling time at acidic conditions. On the other hand, the total number of histidine involved hydrogen bonds decreases. As shown in table 3.3, this holds especially true for the simulations in bulk water where the pH has a much stronger effect on the N-terminal structure. In a pH neutral environment the N-terminus exhibits rather transient hydrogen bonds which correlates with a larger number of different peptide conformations as reflected in the different cluster sizes. This might also accelerate the reorganization into β-sheet conformations. Under acidic conditions the peptide's N-terminus adopts a rather stable coil and bend structure during the sampling time as apparent from figure A.1 presented in the appendix.

By comparing the peptide's folding behavior in bulk solution and at an air-

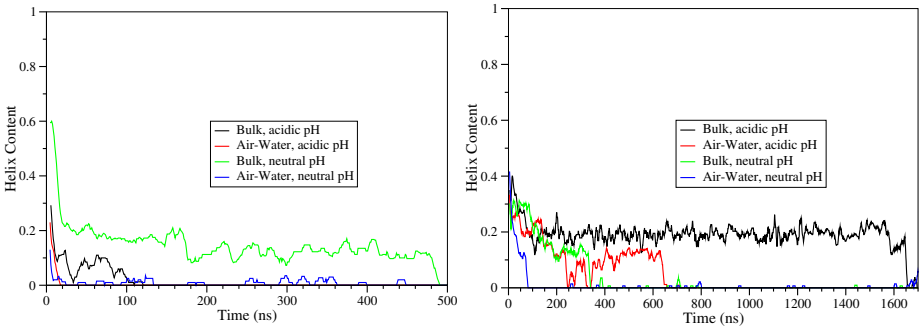

Figure 3.5: Time evolution of helical content for Aβ_{40} (*left*) and Aβ_{42} (*right*) under various conditions.

water-interface we observe that the initial helical structure dissolves faster in the presence of the interface (figure 3.5 (*left*). Furthermore an increased coil but decreased β-bridge and -sheet content was observed compared to the bulk systems (table 3.2). Schladitz *et al.* determined the secondary structure content of Aβ_{40} in a pH neutral aqueous solution by means of circular dichroism

(CD) and at an interface between air and an acidic aqueous solution (pH $\approx$ 5) using infrared reflection-absorption spectroscopy (IRRAS) [188]. They reported a β-sheet content of about 32% in the bulk system which agrees well with our simulations. On the other hand they found an increased β-sheet content of about 75% at the interface while we obtained merely $15 \pm 11\%$. Comparing both studies suggests that rather a cooperative effect due to the increased peptide density at the air-water-interface than its intrinsic hydrophobicity plays the key role in the promotion of β-sheet structures.
The β-sheets in sections Lys16-Phe20 and Met35-Val39 found for Aβ_{40} in pH neutral bulk solution agree partly with results from NMR spectroscopy [189] proposing β-sheets for residues Lys16-Val24 and Ile31-Val40 as well as with MD simulations reporting β-sheets in sections Phe19-Asp23 and Ile32-Gly37 [85].

3.2.2 Aβ_{42}: Secondary structure and cluster analysis

Representatives of the three main clusters are shown in figure 3.6, the secondary structure content for each residue can be found in figure 3.7 whereas the most present hydrogen bonds as well as the coil and β-motif contents averaged over sampling time are tabulated in table 3.4. Time evolutions of secondary structures are shown in section A.1 of the appendix.

The N-terminal secondary structure of the Aβ_{42} peptide in slightly acidic bulk solution is dominated by an α-helix comprising residues Ser8-Val18 and surviving the first 1.6 μs of the simulation as evident from figures 3.5 (*right*) and figure A.3 (*top*) in the appendix. The most present hydrogen bonds stabilize this helix (table 3.4). In the C-terminal we observe rather transient patterns and the β-sheet content is accordingly low. A bridge-turn-bridge motif in residues Lys28-Ile31 is stable for about 1.3 μs (figure A.3 (*top*) of the appendix).

At the surface of a slightly acidic aqueous solution the initial N-terminal helix vanishes after about 650 ns (figure 3.5 (*right*). In the sampling period the secondary structure is dominated by a three-stranded antiparallel β-sheet including residues Phe19-Glu22, Leu34-Val39, and Ala30-Ile31 and stabilized by the hydrogen bonds Ile31-Leu34 (stable for 43% of the sampling time) and Phe20-Gly38 (table 3.4). This motif is accompanied by a β-bridge in Gln15 stabilized by the hydrogen bond Gln15-Ala21. The three stranded β-sheet dominates the three main clusters and the β-sheet content of the corresponding residues as depicted in figure 3.6 (*second row*) and 3.7 (*top, right*), respectively.

Aβ_{42} in bulk water at acidic pH: *459 clusters*

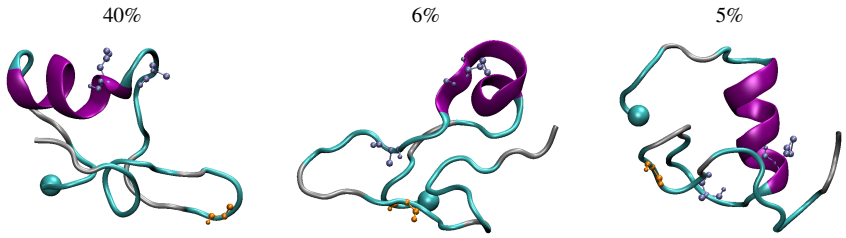

Aβ_{42} at an air-water-interface at acidic pH: *492 clusters*

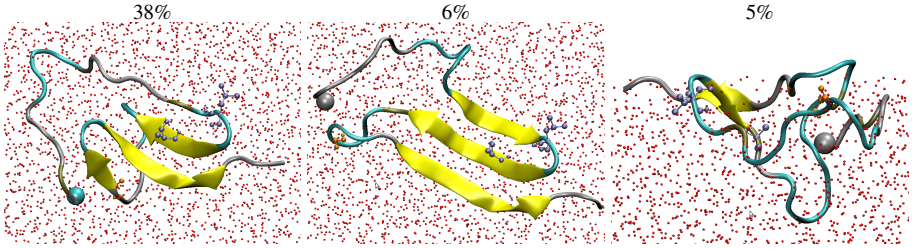

Aβ_{42} in bulk water at neutral pH: *369 clusters*

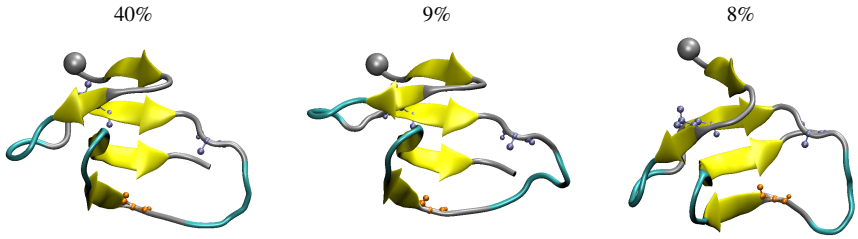

Aβ_{42} at an air-water-interface at neutral pH: *411 clusters*

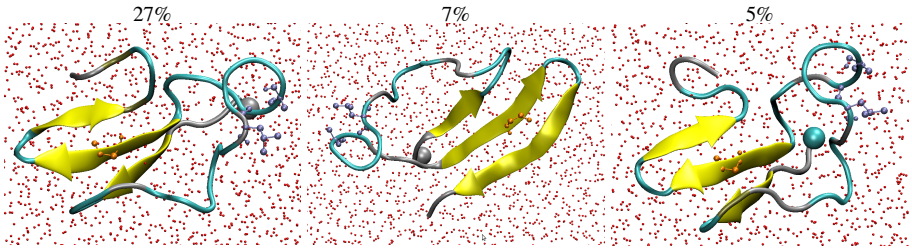

Figure 3.6: Three main conformations of Aβ_{42} at air-water-interface and in bulk solution at slightly acidic and neutral pH as obtained from a cluster analysis of the final 1.5 μs of 2 μs simulations. The representation is the same as chosen in figure 3.3. The air-water-interface is shown in top or side view with its normal orientated in *x*- or *z*-direction, respectively.

In a pH neutral bulk solution the initial N-terminal α-helix dissolves after about 375 ns (figure 3.5 (*right*)). During the sampling time the peptide assumes a stable five-stranded β-sheet spanning the sections Glu3-Arg5, Leu17-Phe20, Val36-Ile41, Ala30-Ile32 and Gly9-Tyr10. Accordingly, the β-sheet content of the whole peptide (table 3.4) as well as of the corresponding residues depicted in figure 3.7 (*bottom, left*) are quite high. The five-stranded β-sheet occurs in all three main clusters shown in figure 3.6 (*third row*) and stabilized by the hydrogen bonds Arg5-Phe20 (present for 46% of the time), Gly38-Ile31 (present for 75% of the time) and Gly9-Met35 (present for 54% of the time). The most robust one of these motifs is the β-sheet with the strands Leu17-Phe20 and Val36-Ile41 as the most stable hydrogen bonds maintain this pattern as tabulated in table 3.4.

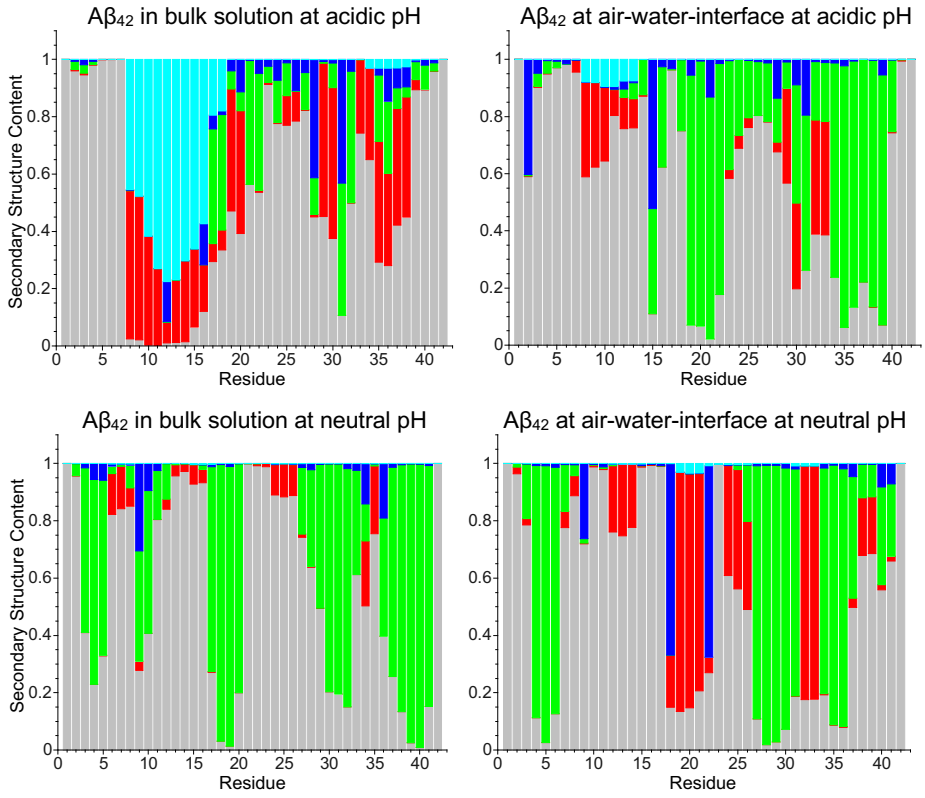

Figure 3.7: Content of secondary structure motifs during the final 1.5 μs of 2 μs simulations for individual residues of Aβ_{42} under various conditions. The representation is the same as that chosen in figure 3.4.

At an air-water-interface at neutral pH the initial α-helix dissolves within 80 ns (figure 3.5 (*right*)). The peptide's secondary structure during the sampling

time is dominated by a three-stranded β-sheet formed by Phe4-His6, Asn27-Ile31, and Leu34-Val36 which is present in all three clusters shown in figure 3.6 (*fourth row*). Hereby the former two β-strands are parallel to each other whereas the third is antiparallel to both. This pattern is stabilized by the three most present hydrogen bonds shown in table 3.2 and indicated by the secondary structure content depicted in figure 3.7 (*right, bottom*).

	Hydrogen Bonds			Secondary Structure	
	$> 60\%$	Bond	Durability	Coils	β-motifs
Bulk water at acidic pH	3	Val12-Asp7 Lys16-Glu11 Gln15-Tyr10	87% 70% 64%	$53 \pm 10\%$	$15 \pm 8\%$
Air-water at acidic pH	9	Phe20-Gly38 Val40-Val18 Gln15-Ala21	90% 86% 85%	$50 \pm 10\%$	$35 \pm 11\%$
Bulk water at neutral pH	9	Phe19-Val39 Ile41-Phe19 Val39-Leu17	97% 92% 90%	$57 \pm 9\%$	$39 \pm 9\%$
Air-water at neutral pH	10	Lys28-Phe4 His6-Lys28 Val36-Gly29	93% 93% 82%	$57 \pm 9\%$	$32 \pm 7\%$

Table 3.4: Hydrogen bonds and secondary structure content of Aβ_{42} in different environments as obtained from a 2 μs simulation. Data were collected from the final 500 ns. Represented are the number of hydrogen bonds existing longer than 60% of the time, the three most common hydrogen bonds and their durability in terms of their content in time as well as the averaged percentage of coils and β-motifs comprising sheets and strands. Hereby, as both are not stabilized by hydrogen bonds, we summarize coils and bends as obtained from the DSSP method in the column termed coils.

Conclusion Aβ_{42}

In contrast to Aβ_{40} we found that the initial N-terminal helix of Aβ_{42} is much more stable at slightly acidic compared to pH neutral conditions as apparent from figure 3.5 (*right*). This holds especially true for the bulk simulations. In accordance with this rather slow unfolding behavior a larger number of stable but smaller content of transient hydrogen bonds involving the histidine residues were observed as presented in table 3.5. The latter effect appears less distinctly in presence of an air-water-interface but corresponds to the influence of the pH

	HIS hydrogen bonds	
	$> 10\%$	total
Bulk water at acidic pH	17	108
Air-water at acidic pH	15	139
Bulk water at neutral pH	9	156
Air-water at neutral pH	13	162

Table 3.5: Total number of hydrogen bonds and hydrogen bonds existing longer than 10% of the sampling time involving histidine residues of the Aβ_{42} peptide.

on the Aβ_{40} alloform. Furthermore a reduction of the β-sheet content in slightly acidic bulk solution but not in presence of an air-water-interface occurs (table 3.4). In both systems, in bulk solution, and at an air-water-interface, the positive charge of the histidine residues at acidic conditions seems to impede the N-terminal residues to form β-strands. Especially the section Glu3-His6 shows a higher propensity for β-sheet formation in case of electrically neutral histidine residues as apparent from the secondary structure content shown in figure 3.7. The corresponding β-sheets involve the hydrophobic core region or the hydrophobic C-terminus. This behavior was partly also found for the Aβ_{40} peptide. The positively and negatively charged residues His6 and Asp7 might have a large dipole moment and therefore their high polarity might decrease the interaction with hydrophobic sequences at acidic conditions. From 1 μs MD simulations under very similar conditions Olubiyi and Strodel reported a comparable effect of the histidine protonation state on the persistence of the Aβ_{42} N-terminal helix [85]. On the other hand, they observed an increase in the β-sheet content due to the positive charge of the His residues in slightly acidic environments. It cannot be excluded that the observed discrepancies are caused by insufficient sampling.

For both pH conditions the presence of an air-water interface results in a faster dissolution of the initial helix in the N-terminus (figure 3.5 (*right*)). The presence of the interface effects the folding behavior much more strongly at acidic conditions where it induces C-terminal β-sheets as reflected by the secondary structure content of the corresponding residues depicted in figure 3.7. This is as well expressed by the number of hydrogen bonds existing longer than 60 % of the time (table 3.4). At pH neutral conditions the presence of an air-water-interface leads to a reduction in the amount of β-sheet conformations in the hydrophobic core residues Leu17-Phe20 which turns into a bridge-turn-bridge-motif in residues Val18-Glu22 as evident from figure 3.7. Much more distinct than in case of Aβ_{40} the formed β-sheets mainly located in the hydrophobic se-

quence sections are parallel to the air-water-interface (compare figures 3.3 and 3.6 (*second and fourth row*)). This β-sheet plane might bind similar structured peptides by hydrogen bonds explaining the increased β-sheet content at the air-water-interface observed in experiment as suggested from the aforementioned study of Schladitz *et al* for Aβ_{40} [188].

Comparison with other MD simulations

Our results might be compared with the aforementioned study by Olubiyi and Strodel [85]. In this work the effect of the atomistic force fields GROMOS43a2 [190] and GROMOS53a6 [186] on the folding behavior of the Aβ_{40} as well as the Aβ_{42} peptide was investigated. The authors found that simulations with GROMOS53a6 as also employed in our study reproduce chemical shifts for both peptides measured by NMR spectroscopy [91]. From their simulations using GROMOS53a6 Olubiyi and Strodel predicted the initial N-terminal helix of Aβ_{40} at physiological pH spanning roughly residues Tyr10-Lys16 to persist for about 600 ns. This agrees partly with our simulations where the helix comprises residues Glu11-Lys16 and dissolves after about 500 ns (figure 3.5 (*left*)). On the other hand they predict the N-terminus to be rather bend or coil dominated after dissolution of the initial N-terminal helix whereas we observe a very high β-sheet content featuring a relatively stable sheet-turn-sheet motif in the section Tyr10-Phe19 occurring after about 800 ns (figure A.2 (*top*) of the appendix). In both studies the section Phe19-Ile32 (Phe19-Gly33 in our case) adopts rather coil and bend motifs although in our case this section is dominated by a π-helix comprising residues Val24-Ile32 during the first 750 ns as apparent from figure A.2 (*top*) of the appendix. Interestingly, a similar helix was found by Olubiyi and Strodel for GROMOS43a2 spanning residues Lys28-Val36 and decaying after 1.4 μs.

Both simulation studies regarding Aβ_{42} under pH neutral conditions described by GROMOS53a6 predict a quite different β-sheet content. Whereas we observe a large and stable β-sheet motif spanning four or partly five β-strands as described in section 3.2.2, Olubiyi and Strodel report a mainly unstructured conformation featuring only temporary β-sheets. In the latter case, the most stable β-sheets arise after about 650 ns, comprise the strands Lys28-Ile31 as well as Gly38-Ala42 and survive for the remaining 850 ns. Interestingly, they found an increased amount of β-sheets at slightly acidic compared to neutral pH whereas we observe a decrease (table 3.4).

It has to be mentioned that our simulations were performed under marginally different conditions as applied in the referenced study. Olubiyi and Strodel coupled their system to a Nosè-Hoover thermostat and a Parinello-Rahman barostat and solvated the Aβ peptide in a water-salt solution exhibiting a NaCl concen-

tration of 150 mM whereas we applied a velocity-rescale thermostat [182] and a Berendsen barostat [183]. We performed our simulations at a NaCl concentration of 100 mM.

3.2.3 Discussion and comparison of Aβ_{40} and Aβ_{42}

In course of our simulations an in general increased content of β-sheets provoked by slightly acidic conditions could not be observed. On the other hand, experimental findings report extraordinary high aggregation propensities as well as cytotoxicities for both major Aβ alloforms at pH values close to the peptide's isoelectric point [176–178]. Guo *et al.* investigated the influence of pH on the oligomerization as well as the fibril formation of Aβ_{40} variants modified by point mutations of charged residues [191]. They substituted the negatively charged Asp, Glu or the positively charged His residues by the electrical neutral Ala amino acid resulting in an increase or decrease in the peptide's net charge by ± 3 e, respectively. By means of turbidity assays, thioflavin T (ThT) binding as well as electron microscopy (EM) they found a maximal propensity of the peptide to form octamers, larger oligomers, very large oligomers, or amyloid fibrils at the isoelectric point of the peptide (pH where its electrophoretic mobility and hence its net charge vanishes). This indicates that instead of the charge of a specific residue the net charge of the peptide plays a crucial role in the pH dependence of amyloid formation, oligomerization, and therefore its toxicity. The results of our simulations support this view as we observed that the β-sheet content of the Aβ monomer does in general not depend on the protonation state of the histidines. The comparably high aggregation rate of both major Aβ alloforms at slightly acidic environments might therefore not be explained by extraordinarily high amounts of aggregation prone monomer conformations but rather by the lack of intermolecular electrostatic repulsion.
Interestingly, we found that the durabilities of initial helical structures of the two alloforms are affected in different ways by changes in the pH. Under slightly acidic environments mimicking conditions the N-terminal helix of the Aβ_{40} peptide dissolves more quickly whereas in case of the $A\beta_{42}$ peptide it dissolves more slowly than at physiological pH. At all conditions and for all peptide lengths the most stable section of the N-terminal helix is roughly located between residues Ser8 and Leu17. This section contains His13 and His14 as well as the positively charged Lys16 and the negatively charged Glu11 residue. The net charge of this section vanishes therefore at the isoelectric point. This might explain the corresponding higher stability of the N-terminal α-helix in case of Aβ_{42}. In case of Aβ_{40} at physiological pH conditions we observe that especially the C-terminal helix retains over an extraordinary long time. As mentioned before this helix spans the GlyXXXGly patterns located in the section Gly25-Gly37. The addi-

tional two hydrophobic residues in Aβ_{42} increase the C-terminal's tendency to minimize its exposure to the aqueous environment and therefore to interact with other peptide sections which furthermore might destabilize the C-terminal helix. This illustrates the flatness of the folding free energy landscape as described in section 1.3.2 of the introduction.

The β-sheet content, especially at the hydrophobic C-terminus of Aβ_{42} is, in particular at the air-water-interface, remarkably higher than for Aβ_{40}. Additionally, these β-sheets are rather parallel to the interface and allow the hydrophobic C-terminus to minimize its exposure to the aqueous solution. This tendency is more distinct for Aβ_{42} due to its additional two hydrophobic residues. Nevertheless, do we not observe a general increase in β-sheet content at the air-water-interface. This is in accordance with replica exchange MD simulations of the Aβ_{42} monomer at anionic and zwitterionic phospholipid bilayers performed by Davis and Berkowitz [192]. At both types of bilayers the peptide adopts secondary structures strongly dominated by coil and bend motifs. The authors proposed that lipid bilayers catalyze the aggregation of Aβ_{42} peptides rather by an increased peptide-peptide interaction than by provoking the transition of monomers to aggregation prone conformations. This is also indicated from our simulations as the alignment of β-sheets parallel to the interface as especially observed for Aβ_{42} might facilitate the formation of intermolecular β-sheets and therefore dramatically increase the β-sheet content as observed in experiment [188].

On the other hand, the higher β-sheet content of Aβ_{42} compared to Aβ_{40} at an air-water-interface might indicate a higher aggregation propensity and thus cytotoxicity of Aβ_{42} *in vivo* where membranes and interfaces are comprehensively present.

4

Amyloid β: Pore formation in phospholipid bilayers

A key aspect regarding the neurotoxicity of Aβ is its high propensity to interact with cell membranes leading to the formation of ion channels [116, 193], insertion of peptides [194, 195], or disruption of membranes [196]. Especially small oligomers are reported to represent the most toxic species of Aβ. In this chapter, as a first step the influence of Aβ_{42} monomers on small membrane defects as provided by water pores is addressed. In this way we try to gain insight into the basic mechanisms of peptide-membrane interactions causing the disturbance of membrane integrity. Water pores within membranes are severe local defects which are capable to increase the permeation of ions, water, or lipids through the membrane [197, 198]. They can form spontaneously by thermal fluctuations [199, 200] or be induced by electrostatic [201], mechanical [202], or chemical stress as arising from peptides [203].
In this chapter we employ molecular dynamics (MD) simulations in combination with the umbrella sampling technique to investigate the influence of an adsorbed Aβ_{42} monomer on the free energy of water pores within a zwitterionic phospholipid bilayer serving as model membrane. From our simulations we are able to determine closure and formation rates as well as densities of membrane pores. In addition our results are compared with a peptide-free reference system. For this system computed water permeabilities and lipid flip flop waiting times are furthermore compared to results reported from experiments.

4.1 Simulation setup

The free energy of small water pores in zwitterionic phospholipid bilayers with and without an Aβ_{42} monomer attached to each leaflet of the bilayer is determined using the potential of mean force (PMF) as obtained from MD simulations combined with the umbrella sampling technique [204] as described in section 2.2 of the introduction. The investigated bilayers contain 128 1,2-dipalmitoyl-sn-glycero-3-phosphocholine (DPPC) lipids depicted in figure 1.1 presented in section 1.1 of the introduction. Pores were induced in the bilayer by pulling a single phosphatidylcholine (PC) headgroup in z-direction to the center of the bilayer. The z-component of the distance between the headgroup and the center of the bilayer was chosen as reaction coordinate λ. Thus, pore formation takes place for $\lambda \to 0$ as depicted in figure 4.1. Two systems were compared: a pure DPPC bilayer and a DPPC bilayer with an Aβ_{42} monomer attached to each bilayer leaflet. Hereby, the initial configuration of the Aβ_{42} monomer attached to a DPPC bilayer was taken from replica exchange simulations [205, 206] performed by Davis and Berkowitz [192]. In advance of the cited study Davis and Berkowitz estimated the free energy of peptide binding by pulling one unstructured Aβ_{42} monomer to the surface of a DPPC bilayer using the umbrella sampling method [207]. Starting from the obtained final configuration of these simulations they investigated the structure of the peptide adsorbed to the bilayer surface by means of the replica exchange method [192]. Due to the enhanced sampling provided by the replica exchange technique the peptide configuration should likely reside in a local free energy minimum at the start of our simulations. To obtain a symmetric setup with one peptide attached to each of the bilayer leaflets we copied and rotated the peptide containing leaflet around the x-axis parallel to the bilayer surface. We compared our simulations with a peptide-free reference system.

To each system about 5700 SPC[1] [164] water molecules and to the peptide containing system Na^+ counter ions were added. The protonation of Aβ_{42} was chosen such as to correspond to a physiological pH of 7. That is, the arginine and the lysine residues were modeled as cationic, aspartic and glutamic acid residues as anionic, the histidine residues as neutral, the C-terminus as deprotonated, and the N-terminus as protonated. This leads to a peptide net charge of -3 e. All systems were energy minimized using the steepest descent method. The peptide-free system was equilibrated for 10 ns and the peptide-bilayer system for 20 ns. The initial configurations for each reaction coordinate were obtained by pulling one lipid headgroup from its equilibrium position normal to the bilayer surface to the center of the bilayer. To locate

[1] **S**imple **P**oint **C**harge

the equilibrium position within the potential of mean force (PMF), in an additional simulation, the corresponding lipid headgroup was pulled about $3-4$ Å out of the bilayer into the aqueous solution. Both simulations were carried out with a pulling rate of $0.02\,\mathrm{nm/ps}$ and an umbrella potential of $500\,\mathrm{kJ/(mol\cdot nm^2)}$. From these simulations we took about 70 snapshots serving as initial configuration for each particular umbrella window. In each window the distance between the pulled lipid headgroup and the center of the bilayer were restrained normal to the bilayer surface using an umbrella potential with a force constant of $5000\,\mathrm{kJ/(mol\cdot nm^2)}$. Each setup was equilibrated for 10 ns and data were collected from additional 100 ns simulation runs. The PMF was calculated using the weighted histogram analysis method (WHAM) [158] described in section 2.2 whereas the statistical errors were estimated by the Bayesian bootstrap method [208]. Both methods are implemented in the Gromacs software package [161] and described in section 2.2.

To determine pore closure rates the umbrella window with the lipid headgroup restrained at the center of the bilayer ($\lambda = 0$) was employed. In both cases, with and without peptide, ten configurations at separate times with a pre-formed pore were taken. After releasing the restrained lipid headgroup the simulations were extended until the pore had closed.

For all simulations a temperature of 323 K was maintained by separately coupling lipids, water, peptides, and ions to a velocity rescaling thermostat [182], with a relaxation time of 0.1 ps. At the chosen temperature the bilayer is in the biologically relevant fluid phase. Furthermore the system was coupled semi-isotropically to a Berendsen barostat [183] with a relaxation time of 0.5 ps in order to maintain an average pressure of 1 atm. Van der Waals and electrostatic short range interactions were truncated at 0.9 nm whereas for long range electrostatics the particle mesh Ewald method [185] was applied. All bonds of the lipids and peptides were constrained using the LINCS algorithm [209]. The lipids were described by parameters from Berger *et al.* [210] while the Aβ_{42} peptide was treated using the united-atom GROMOS96 force field ffG43a1 [165, 166]. The simulation time step was 2 fs. All simulations were performed using the GROMACS 4.0 software package [165–167].

It has to be mentioned that we also determined the PMF of an asymmetric peptide-bilayer system with an Aβ_{42} peptide attached to only one of the bilayer leaflets as obtained from the referenced study [192]. For this system an extraordinarily high free energy barrier of pore formation ($\Delta G \approx 94\,\mathrm{kJ/mol}$) was obtained. This is presumably caused by a discrepancy in the effective areas per lipid A_{Lip} between both leaflets. For the peptide-free system $A_{\mathrm{Lip}} = 0.689 \pm 0.011\mathrm{nm}^2$ whereas for the symmetric system featuring one attached Aβ_{42} monomer at each leaflet a smaller area

per lipid of $A_{\mathrm{Lip}} = 0.660 \pm 0.008\,\mathrm{nm}^2$ was found. In case of the asymmetric system this results in an expansion of the peptide containing and a compression of the peptide-free leaflet. For this system an area per lipid of $A_{\mathrm{Lip}} = 0.669 \pm 0.012\,\mathrm{nm}^2$ was observed. This finite size effect is the presumed reason for the observed extraordinarily high free energy barrier. Consequently, we did not analyze this system in more detail.

4.2 Results

In this section we first describe the influence of the Aβ_{42} peptide on the size and shape of induced pores as well as on the order of the bilayer's hydrocarbon tails described in section 2.4.1 of the introduction. Subsequently, we determine the free energy of membrane pores and explain the results partially by the Aβ_{42} mediated disturbance of the nonpolar bilayer tail region. After computing pore densities, water permeabilities, and lipid flip flop waiting times and comparing the latter with experimental results, pore closure and pore opening times are estimated. We conclude with a summary and a discussion.

4.2.1 Size and shape of pores

Pores were induced by pulling one lipid headgroup along the bilayer normal to the center of the bilayer. For the peptide-free system a pore forms after about 70 ns whereas in presence of bilayer attached Aβ_{42} peptides a pore was induced already after about 5 ns. In the latter case the propensity of pore formation strongly depended on the position of the pulled lipid. We observed pore formation by pulling a lipid headgroup in the vicinity of the hydrophilic segment Ser8-His13. On the other hand, no pore was formed when a lipid headgroup close to the hydrophobic tail region Val40-Ala42 or between the hydrophobic segments Lys16-Phe19 and Ile31-Leu34 was pulled to the bilayer center. Pore formation in the vicinity of hydrophobic segments increases their exposure to water and might therefore be unfavored.

The size and shape of the induced pores are apparent from the snapshots shown in figure 4.1 as well as from the water density maps depicted in figure 4.2. In case of the peptide-free system a relatively large, hour glass shaped pore can be observed whereas the induced pore in case of the peptide containing system is rather small and exhibits a disordered toroidal shape. Hereby it has to be noted that the density maps are averaged over time. In this way the size of the pore in case of the peptide attached bilayer appears much larger in the density map 4.2 (*right*) than in the snapshot 4.1 (*bottom*). This does not hold true for the peptide-free system and indicates that the small pore induced in the Aβ_{42}

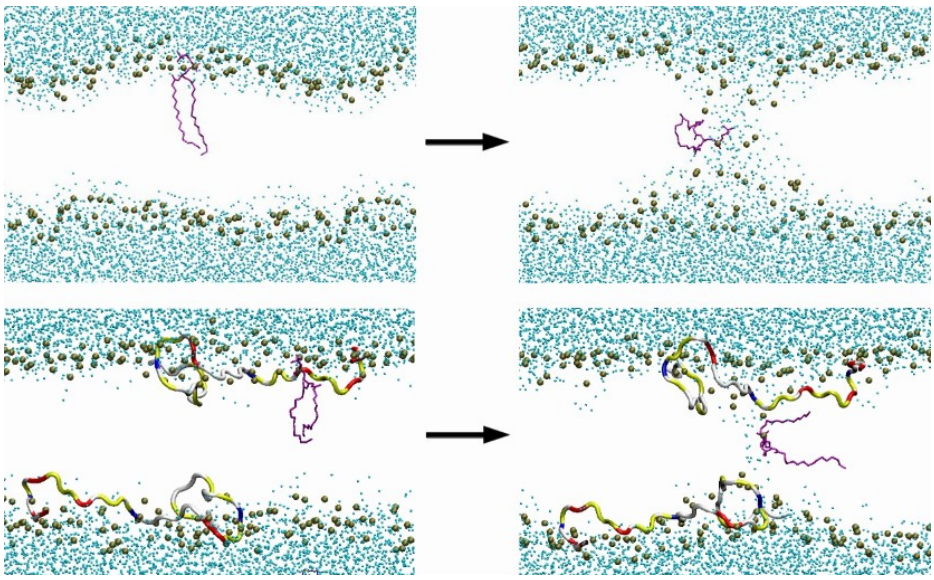

Figure 4.1: Pore formation for $\lambda \to 0$ in absence (*top*) and presence (*bottom*) of Aβ_{42}. The water oxygens are shown as cyan spheres and the lipid restrained by the umbrella potential as purple sticks. The phosphor atoms of the other lipids are shown in tan. The peptides are depicted in ribbon presentation; here, colors distinguish between anionic (blue), cationic (red), hydrophobic (white), and hydrophilic (yellow) residues.

attached bilayer is rather mobile parallel to the bilayer surface whereas the comparably large pore formed in the pure bilayer more or less keeps its position.
The number of water molecules inside the pore and the flux of water molecules

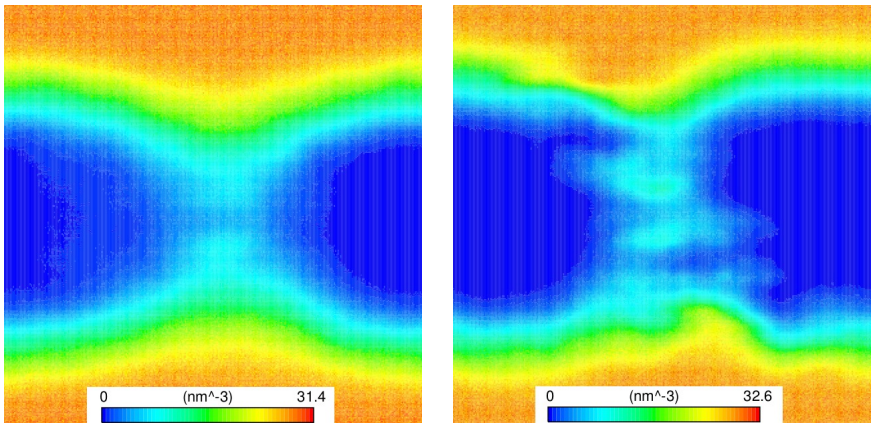

Figure 4.2: Number density map of water molecules in the $x-z$ plane averaged over the 90 ns where a pore is formed. The densities are averaged over 2 nm in y-direction with the pulled lipid headgroup centered in the slices (without (*left*) and with Aβ_{42} (*right*)).

through the pore were calculated using the scripts g_count and g_flux by Oliver Beckstein [211]. To determine the number of water molecules inside a pore the number of molecules residing between the two polar headgroup regions in presence and absence of a pore were counted. Both results were subtracted from each other. The position of each headgroup region normal to the bilayer was determined from the center of mass of its phosphor atoms. This yielded 375 water molecules in the pore for the peptide-free and 195 for the peptide containing system. The flux was estimated from the number of water molecules entering the interior of the bilayer through one headgroup region and leaving it through the other headgroup region. For the peptide-free system a unidirectional flux of $j = 20$ ns^{-1} and for the peptide containing system $j = 0.4$ ns^{-1} was obtained. It has to be noted that in case of the pure bilayer three lipid flips during the 30 ns simulation time during which a stable pore was present were observed. Lipid flips describe the translation of a lipid through the bilayer from one leaflet to the other as shown in figure 1.2 depicted in section 1.1 of the introduction. Our finding agrees well with results from earlier MD simulation studies of vesicle formation [212] and pore mediated lipid flip flops [213]. Similar lipid flips did not occur within the peptide attached bilayer.

We computed lipid order parameters of the pure and the peptide attached bi-

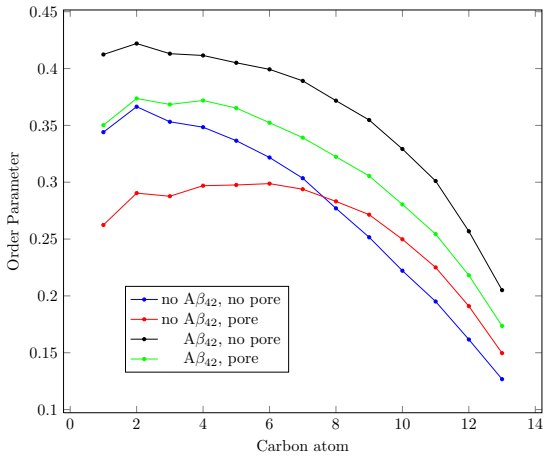

Figure 4.3: Order parameters averaged over 10 ns with and without pore.

layer in presence and absence of a pore by means of equation (2.20) described in section 2.4.1 of the introduction. The results are shown in figure 4.3. Lipid tails in vicinity of the water pore are more parallel to the bilayer surface and the order parameters decrease accordingly as if compared to the case where no pore is formed. In general the attachment of the Aβ_{42} peptides leads to an increase of the lipid order parameters which might be explained by the decreased area per

lipid as described in the method section 4.1. Interestingly, we found that for the peptide-free system the segments of the hydrocarbon tails with a carbon number ≥ 8 are more strongly orientated normal to the bilayer surface than in absence of a pore. We thus observe a crossover of the corresponding graphs.

4.2.2 Free energy of membrane pores

The potentials of mean force being the main result of this study are shown in figure 4.4. In case of the trajectories where pore formation occurs ($\lambda \to 0$) only the part of the trajectory featuring an already formed pore was considered. The reason for this approach is given in the discussion (section 4.3). To describe the profile of the PMF we start from the equilibrium position of the pulled lipid headgroup located in the free energy minimum. An increase of λ corresponds

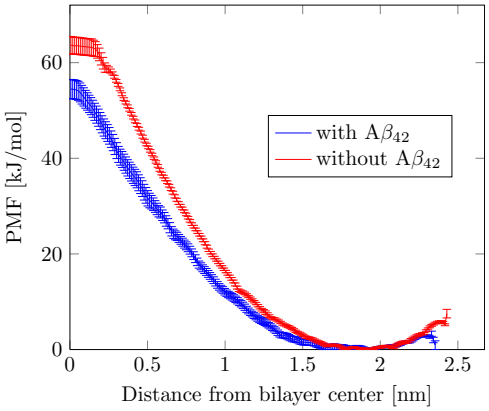

Figure 4.4: Potential of mean force (PMF) governing the motion of a lipid vertically to the bilayer surface for a pure and an Aβ_{42} monomer attached DPPC bilayer. Pore formation takes place in the range of the plateau at $\lambda \to 0$.

to pulling the lipid out of the bilayer and therefore exposing its hydrophobic tail to an aqueous environment and consequently to an increase of the free energy. Decreasing λ and thus pulling the lipid headgroup into the bilayer causes an increase of the free energy as it forces the polar headgroup into the nonpolar tail region. If a hydrophilic pore forms ($\lambda \to 0$) the free energy only slightly changes by further decreasing λ.
This holds especially true for the peptide-free system and can be explained by the geometry of a hydrophilic, hour glass shaped pore. In this shape the nonpolar tails of the pulled lipid are placed within the tail region of the bilayer whereas its hydrophilic headgroup faces water. Dragging the lipid headgroup further into the lipid bilayer (decreasing λ) corresponds to its translation lateral to the curved bilayer surface. Here, the pulled lipid headgroup remains exposed to water and

its nonpolar tail buried in the hydrophobic tail region. This process is similar to pore mediated lipid flips which occurs rather spontaneously once a pore is formed. Accordingly, the potential of mean force exhibits a rather flat shape in this region. For the peptide containing system this effect could not be observed as in this case no real hydrophilic pore is formed. We obtain a free energy of membrane pores of

$\Delta G_{\mathrm{wo}} = 63.7 \pm 1.8$ kJ/mol	for the pure DPPC bilayer and
$\Delta G_{A\beta} = 54.5 \pm 2.0$ kJ/mol	for the Aβ_{42} attached bilayer.

4.2.3 Influence of Aβ_{42} on the bilayer tail region

The mass density profiles given in figure 4.5 B indicate that the Aβ_{42} monomers deeply intrude into the hydrophobic tail region of the bilayer. Furthermore the attachment of the peptides leads to a broadening of the phosphor and nitrogen densities along the bilayer normal as apparent from figure 4.5 A, B. This

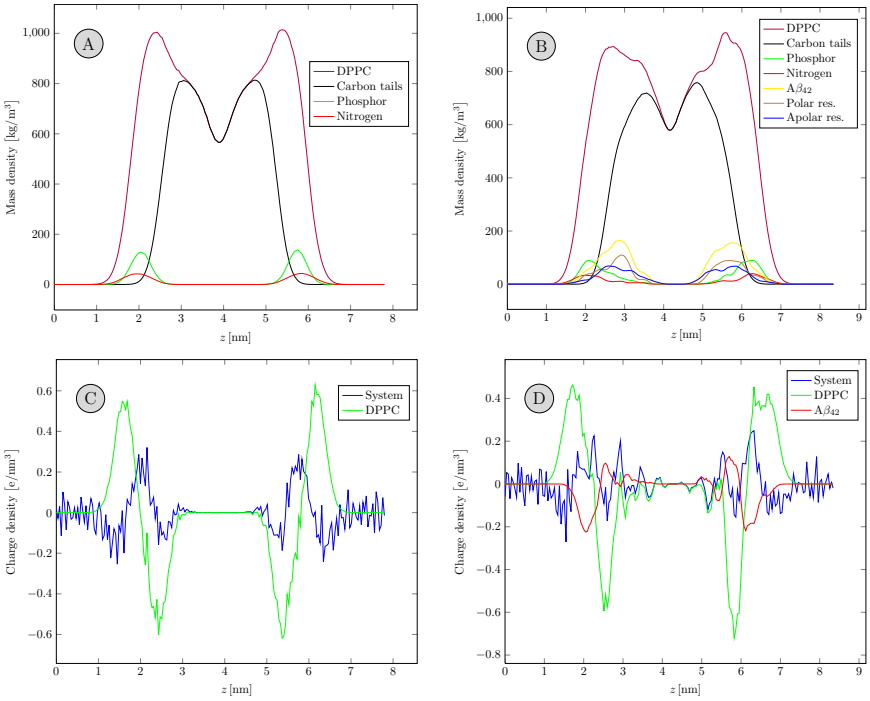

Figure 4.5: Mass and charge densities of the pore-free lipid bilayer without peptide (A, C) and attached by an Aβ_{42} peptide (B, D) averaged over 40 ns.

corresponds to an increased roughness of the polar headgroup region and thus an effective decrease in the thickness of the nonpolar region of the bilayer. To

validate this assumption we calculated the standard deviation of the z-positions of the lipid phosphor atoms along the bilayer surface.
In case of the bottom leaflet a standard deviation of 0.03 nm for the peptide-free and 0.3 nm for the peptide-containing system was obtained. The reduction in the effective thickness of the nonpolar region within the bilayer is even amplified by the intrusion of polar and charged residues of the Aβ_{42} peptide into the hydrophobic bilayer core. This effect is indicated by the charge distributions shown in figure 4.5B. Whereas the bilayer center in the peptide-free system shows no charge density variations over a range of about 2 nm, this region is reduced to about 0.5 nm in the peptide containing system. A broaden increase in the electron density in the nonpolar core region of synaptic plasma membranes due to the presence of Aβ oligomers observed by small angle X-ray diffraction spectroscopy was as well reported by Mason *et al.* [214].
Furthermore the thickness of the bilayer as given by the distance between the two headgroup regions determined by the center of masses of the lipid phosphor atoms was determined. For the pure bilayer a thickness of 3.64 ± 0.05 nm and for the peptide attached bilayer a larger value of 3.75 ± 0.04 nm was obtained. The corresponding error was estimated from the standard deviation over simulation time. We can therefore exclude that the higher propensity for pore formation in case of the peptide containing system is caused by a general thinning of the bilayer mediated by the peptide.

4.2.4 Pore densities

In our simulations we observed that a membrane pore is induced by pulling a single lipid headgroup normal to the bilayer to the center of the bilayer. If the distance z between the lipid headgroup and the bilayer center falls below a critical value z_p, a pore forms. In unrestrained systems this happens spontaneously due to thermal fluctuations. The probability P_p that the distance between a lipid headgroup and the bilayer center is smaller than z_p and thus that a pore is induced is given by

$$P_\mathrm{p} = \exp\left(-\beta \cdot G_\mathrm{p}\right). \tag{4.1}$$

Hereby $\beta = 1/(k_\mathrm{B}T)$ is given by the Boltzmann constant k_B and the temperature T whereas G_p denotes the free energy of membrane pores as given by

$$G_\mathrm{p} = -k_\mathrm{B}T \cdot \log\left(Z_\mathrm{p}/Z\right). \tag{4.2}$$

Here, Z denotes the partition function

$$Z = \int_0^{z_c} \exp\left(-\beta \cdot G(z)\right) \mathrm{d}z \tag{4.3}$$

where z_c denotes the z-position of the phosphocholine group above which the lipid is desorbed from the bilayer and Z_p the partition function of all lipid states involving pore formation ($z \leq z_p$) according to

$$Z_p = \int_0^{z_p} \exp\left(-\beta \cdot G(z)\right) \mathrm{d}z. \tag{4.4}$$

The symbol $G(z)$ denotes the potential of mean force (PMF) along z determined from umbrella sampling as described in section 2.2 of the introduction. The density of pores, i.e., the number of pores per area, is computed from

$$\rho_p = \frac{P_p}{N_l \cdot a}. \tag{4.5}$$

Here we took into account that N_l lipids reside in each existing pore and that these lipids are not available for the formation of new pores. From our simulations N_l was determined by counting all lipid phosphor atoms with $z \leq z_p$ in a given pore. In equation 4.5 a is the area per lipid. This equation holds only true for the peptide-free system as in this case the bilayer surface is homogeneous. If on the other hand a peptide is attached to the bilayer a lipid can be in contact with the peptide or not. The corresponding pore density depends on the number of lipids in contact with a peptide $n_c n_{pep}$. Here, n_{pep} denotes the number of peptides per lipid and n_c the number of lipids in contact with a single peptide. For peptide attached bilayers we obtain

$$\rho_P = \frac{P_c \cdot n_c n_{pep}}{N_{l,c} a} + \frac{P_n \left(1 - n_c n_{pep}\right)}{N_{l,n} a}. \tag{4.6}$$

A more detailed derivation of this equation can be found in section A.2 of the appendix. The probabilities for a lipid to reside close to the bilayer center determined by equation 4.1 are denoted as P_i whereas $N_{l,i}$ stands for the number of headgroups fulfilling $z \leq z_p$. Hereby we took lipids in contact with a peptide ($i = c$) and lipids not affected by any peptide ($i = n$) into account.
The density of pores within a pure lipid bilayer was computed via equation (4.5) and within a peptide attached bilayer via equation (4.6). Hereby it is necessary to integrate the Boltzmann factor in equation 4.3 up to z_c associated with lipid desorption. As this state is not included in our simulations we extrapolated the PMF by means of a harmonic function. Hereby we neglected the plateau in the

PMF corresponding to the pore state. Results from a comparable study published by Tieleman and Marrink [215] suggest that the description of the PMF profile by a harmonic function is appropriate. Figure 4.6 shows the extrapolated Boltzmann factors $b(z) = \exp(-\beta \cdot G(z))$ occurring in equation 4.3 and 4.4 for the peptide containing (*left*) and the peptide-free system (*right*). The Boltzmann factor in equation (4.3) was integrated up to a z-coordinate corresponding to a lipid desorption free energy of $\Delta G_c = 63$ kJ/mol. Lipid desorption free energies of $\Delta G_c = 75 - 80$ kJ/mol and $\Delta G_c = 63 \pm 4$ kJ/mol have been reported for pure DPPC lipid bilayers by Tieleman [215] and Grafmüller [216], respectively. Here, it has to be noted that the results are rather insensitive to this choice as the Boltzmann weight already drops below 10^{-4} for a z-coordinate value associated with $G(z \to z_c) = 30$ kJ/mol. For the pure bilayer we observed pore formation

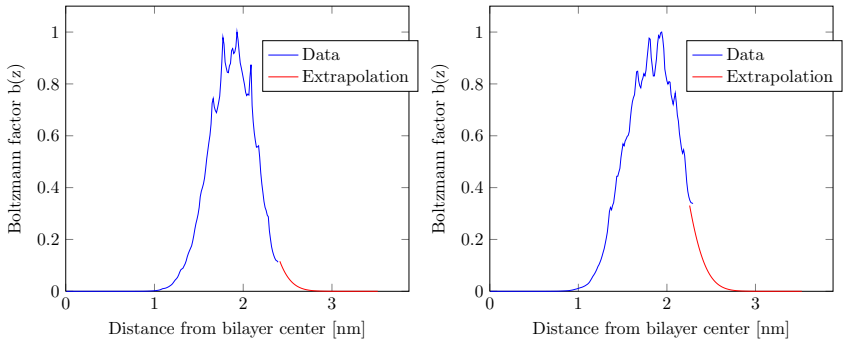

Figure 4.6: Boltzmann factors occurring in equation 4.3 and 4.4 for the peptide-free (*left*) and the peptide containing system (*right*).

for $z \leq 0.3$ nm and in case of the peptide attached bilayer for $z \leq 0.1$ nm. By means of phosphor atom number densities we computed the number of lipids involved in a single pore averaged over time to $N_{L,n} = 2.5$ for the peptide-free and $N_{L,c} = 0.1$ for the peptide containing system. In case of the peptide containing system we estimated the number of lipids in contact with the peptide to $N_c = 35$. Hereby we counted all headgroup phosphor atoms residing closer to the peptide than the headgroup phosphor atom of the pulled lipid. In vicinity of Aβ_{42}, pore formation only occurred for one out of three pulled lipids as described in section 4.2.1. The probability P_c was thus divided by three. With the ratio of peptides per lipid $n_{pep} = 1/64$ we obtain

$\rho_p = 1.8 \pm 3.6 \cdot 10^3$ cm^{-2}	for the peptide-free system and
$\rho_p = 1.2 \pm 1.4 \cdot 10^5$ cm^{-2}	for the peptide containing system.

Thus the attached Aβ_{42} peptides increase the density of membrane pores by a factor of about 10^2.

4.2.5 Water permeabilities and lipid flip flop waiting times

The permeability of molecules through a membrane can be calculated by their flux J through the membrane divided by the permeation driving concentration difference, namely the osmotic gradient, ΔC, as

$$P = \frac{J}{\Delta C}.$$

The flux J is given by the pore density ρ_p and the flux j of molecules through a single pore according to $J = j \cdot \rho_p$. In our case the net flux of water through the bilayer vanishes as the concentrations on both sides of the bilayer coincide and the translation of water molecules through the membrane is driven by self-diffusion. Thus only the uni-directional flux can be considered where the water number density can be assumed to be $\Delta C = 55$ M [215]. With $j = 20$ ns^{-1} for the peptide-free and $j = 0.4$ ns^{-1} for the peptide containing system obtained in section 4.2.1 we obtained

$P \approx 1.1 \cdot 10^{-9}$ cm/s	for the pure DPPC bilayer and
$P \approx 1.4 \cdot 10^{-9}$ cm/s	for the peptide containing system.

Hence, for the peptide attached and the pure bilayer similar water permeabilities are obtained. For pure DPPC bilayers water permeability coefficients were reported to cover a range of $P = 10^2 - 10^4$ cm/s from MD simulations [217, 218] as well as by H_2OD_2O exchange light scattering experiments [199]. Water permeation seems therefore not to be mediated by nanopores as already suggested earlier [219].
A lipid flip as described in section 4.2.1 is in general accompanied by the reverse process, a lipid flop, as both leaflets contain the same number of lipids in equilibrium. The corresponding lipid flip flop waiting time can be determined by

$$\tau = \frac{1}{J}. \tag{4.7}$$

For the peptide-free system three lipid flips were observed during 30 ns and thus $j = 0.1$ ns^{-1}. This leads to a flip flop waiting time of $\tau = 2.71 \cdot 10^2 - 8.12 \cdot 10^2$ s. Accordingly, flip flop times are in the range

$$5 \text{ min} \leq \tau_{\text{Lip}} \leq 14 \text{ min}.$$

By means of sum-frequency vibrational (SFV) spectroscopy Liu and Conboy determined the half-life of lipid flip flops for a planar supported bilayer of DPPC lipids at about 310 K to 9.2 min [220]. It should be noted, though, that our simulations were carried out at 323 K and thus above the phase transition of free standing DPPC bilayers at 314 K [221]. The SFV spectroscopy experiments

were conducted at 310 K and thus below but close to the phase transition of free standing DPPC bilayers. However, supported bilayers are typically under tension which is expected to lower the main transition temperature such that the DPPC bilayers probed in Ref. [220] were most likely in the fluid phase. Hence, the good agreement of the flip flop times between these experiments and our simulation may not be coincidental. Our results confirm that pore formation is the rate determining factor of lipid flip flops [213].

4.2.6 Pore closure and pore opening times

The bilayer attached Aβ_{42} peptide dramatically increases the pore closure time. Whereas pores within the pure bilayer close after 17 ns to 303 ns, in case of the peptide attached bilayer closure times of 40 ns up to over 1.2 μs were observed. In the latter case pore closure took only place in six out of ten simulations.
From the number $q_{\mathrm{cl}}(t)$ of simulations featuring a closed pore at time t and the total number of performed simulations n the probability $P_{\mathrm{cl}}(t)$ for a pore to be closed at time t is estimated as

$$P_{\mathrm{cl}}(t) \equiv P(t \geq \tau_{\mathrm{cl}}) = \frac{q_{\mathrm{cl}}(t)}{n}. \tag{4.8}$$

Thereby it is assumed that the pore opened at time zero. The corresponding closure time is denoted as τ_{cl}. The probability $P_{\mathrm{cl}}(t)$ is furthermore related to

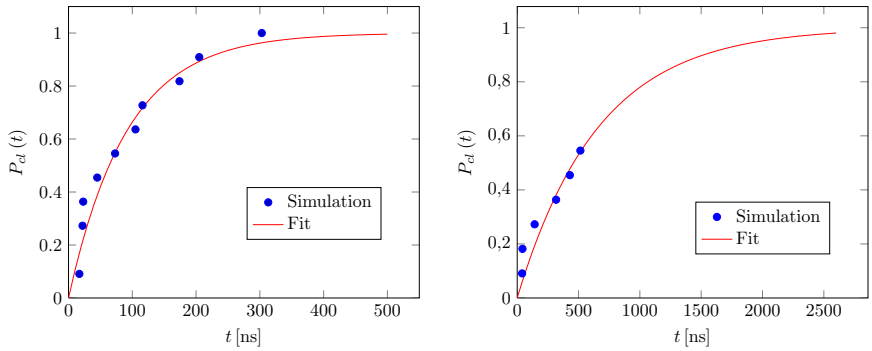

Figure 4.7: Probability of a pore open at $t = 0$ being closed at time t, $P_{\mathrm{cl}}(t)$, from simulation and fitted for the peptide-free (*left*) and the peptide containing system (*right*).

the probability of a pore being still open at time t, $P_{\mathrm{op}} \equiv P(t < \tau_{\mathrm{cl}})$, according to

$$P_{\mathrm{cl}}(t) = 1 - P_{\mathrm{op}}(t).$$

Assuming a Markovian process for pore closure leads to

$$P_{\mathrm{op}}(t) = \exp\left(-\frac{t}{\tau_{\mathrm{cl}}}\right)$$

and thus

$$P_{\mathrm{cl}}(t) = 1 - \exp\left(-\frac{t}{\tau_{\mathrm{cl}}}\right). \tag{4.9}$$

We estimated the confidence interval $\left[P_{\mathrm{cl}}^{-}, P_{\mathrm{cl}}^{+}\right]$ via the Wilson score method [222],

$$P_{\mathrm{cl}}^{\pm}(t) = \frac{P_{\mathrm{cl}}(t) + \frac{z_{1-\alpha/2}^2}{2n} \pm \sqrt{\frac{P_{\mathrm{cl}}(t)(1-P_{\mathrm{cl}}(t))}{n} + \frac{z_{1-\alpha/2}^2}{4n^2}}}{1 + \frac{z_{1-\alpha/2}^2}{n}}. \tag{4.10}$$

Hereby $z_{1-\alpha/2}$ denotes the critical value of the normal distribution with an error α. This says that in case of normal distributed data around a mean value $\bar{x}$ the quantile $1-\alpha$ of the data lies within the interval $\left[\bar{x} - z_{1-\alpha/2}, \bar{x} + z_{1-\alpha/2}\right]$. To obtain a confidence level of 95% we used $\alpha = 5\%$ resulting in $z_{1-\alpha/2} = 1.96$. The probabilities $P_{\mathrm{cl}}(t)$ according to equation (4.9) fitted to the simulation data are depicted in figure 4.7. Using the confidence interval $\left[P_{\mathrm{cl}}^{-}, P_{\mathrm{cl}}^{+}\right]$ obtained from equation (4.10) in combination with the fitting function (4.9) yields

$51.4\ \mathrm{ns} \leq \tau_{\mathrm{cl}} \leq 91.8\ \mathrm{ns}$	for the peptide-free system
$296.1\ \mathrm{ns} \leq \tau_{\mathrm{cl}} \leq 1789.2\ \mathrm{ns}$	for the peptide containing system.

On the basis of the pore closure rates $k_{\mathrm{cl}} = \tau_{\mathrm{cl}}^{-1}$ the pore formation rates, k_{f}, may be derived from the detailed balance condition

$$k_{\mathrm{f}} = k_{\mathrm{cl}} \cdot \exp(-\beta \Delta G)$$

with $\beta = 1/(k_{\mathrm{B}}T)$. This yields

$4.0 \cdot 10^{10}\ \mathrm{s^{-1}cm^{-2}} \leq k_{\mathrm{f}} \leq 2.8 \cdot 10^{11}\ \mathrm{s^{-1}cm^{-2}}$	in absence and
$6.2 \cdot 10^{10}\ \mathrm{s^{-1}cm^{-2}} \leq k_{\mathrm{f}} \leq 1.7 \cdot 10^{12}\ \mathrm{s^{-1}cm^{-2}}$	in presence of Aβ_{42}.

Hence, the attached Aβ_{42} peptide considerably stabilizes nanopores and furthermore tends to slightly increase pore formation rates.

4.3 Discussion and summary

In this chapter it was demonstrated that Aβ_{42} monomers strongly affect zwitterionic phospholipid bilayers leading to thermodynamic and kinetic stabilization of bilayer defects as given by small membrane pores. According to this, the adsorption of Aβ_{42} on the one hand leads to an increase of the pore density by a factor 10^2 as well as a dramatic stabilization of nanopores as in terms of increased pore closure times (life times of pores). On the other hand, the size of membrane pores involving peptides is decreased compared to peptide-free pores. Pore opening rates and water permeabilities were not considerably affected by adsorbed Aβ_{42} monomers. The higher propensity of the peptide attached bilayer to form nanopores might be explained by the peptide mediated disturbance of the nonpolar bilayer region resulting in an effective thinning of this region. This furthermore might facilitate the intrusion of water into the bilayer and thus promote the formation of nanopores. On the other hand, the interaction of lipid headgroups with the peptide might prevent the complete reorganization of the lipids into larger hydrophilic pores. Instead we observe a comparably small pore exhibiting a rather disordered shape.
Our results for the peptide-free reference system might be compared to a similar study by Tieleman and Marrink [215]. Whereas we obtain a free energy of membrane pores of about 64 kJ/mol, Ref. [215] reports a free energy change upon pulling a lipid headgroup from its equilibrium position to the bilayer center of $75 - 80$ kJ/mol. We believe that the main reason for this discrepancy is the underestimation of the pore state due to the shorter production runs of the simulations performed in Ref. [215]. If a lipid is restrained close to the center of the bilayer, a hydrophilic pore forms after several nanoseconds. In this case the free energy of the state characterized by the presence of a hydrophilic pore is lower than the "no pore" state. Hence, the former is more likely and more stable. Accordingly, we obtain a much higher free energy of 78 kJ/mol if we only consider the part of each trajectory in which no pore is formed yet. In contrast, regarding merely the trajectory sections featuring a hydrophilic pore we obtain 64 kJ/mol. Consequently, for long time scales the initial absence of a pore can in terms of the potential of mean force be neglected as the system will strongly prefer the "pore" state. Tieleman and Marrink collected their data from a 50 ns production run. In our study we observe that pore formation takes place after 45 ns in four of nine windows. Therefore the state of the system with an already formed pore is apparently underestimated in the study of Tieleman and Marrink. As a counter check we computed the potential of mean force using only the first 50 ns of our simulations and obtained a free energy of 76 kJ/mol in accordance with the results of Marrink and Tieleman. In addition we extended the particular trajectory in which the lipid headgroup is restrained as close as possible to the

bilayer center $z \approx z_{\mathrm{p}}$ without formation of a pore. No pore formation was observed within a 500 ns simulation. In this way we ensured that the whole range of the reaction coordinate where pore formation takes place is included.
Furthermore, it has to be noted that Tieleman and Marrink simulated a smaller bilayer patch of 64 DPPC lipids. The different size of the bilayer patches, though, might not play a crucial role for the discrepancy observed in the results as the previous analysis showed that this can sufficiently be explained by the difference in simulation timescales.
Tieleman and Marrink also determined lipid flip flop waiting times. Their results seem to overestimate the waiting times as they obtain $4-30$h, whereas our values are with 5 min $\leq \tau_{\mathrm{Lip}} \leq$ 14 min much closer to results reported from experiment.
This study might serve as starting point to investigate the influence of more toxic species like dimers or small oligomers of Aβ_{42} on pore formation and closure.

5

NK-2: Affinity for phospholipid bilayers

In this chapter the mechanisms determining the selectivity of antimicrobial peptides between eu- and prokaryotic plasma cell membranes are studied. To this end the affinities of the antimicrobial peptide NK-2 for zwitterionic 1,2-dioleoyl-sn-glycero-3-phosphocholine (DOPC) and anionic 1,2-dioleoyl-sn-glycero-3-phosphoglycerol (DOPG) bilayers are investigated. These serve as model systems for the corresponding membranes as described in section 1.1 of the introduction. The difference in the binding affinities is determined by means of molecular dynamics (MD) simulations in combination with the thermodynamic integration (TI) method. Our studies were performed at atomistic resolution. In a related work von Deuster and Knecht [145] employed a simplified coarse-grained description and dissected various entropic and enthalpic contributions determining the binding free energy. In the present study, the focus is on the accuracy and the comparability of the computational method with experimental results. After describing simulation details the peptide structure as well as the system composition in terms of density profiles are briefly outlined. Subsequently, our results are compared with the simulations from von Deuster and Knecht [145]. Finally, corresponding experimental binding free energies are inferred from zeta potentials estimated for DOPC, DOPG, and DOPC/DOPG vesicles by means of electrophoresis experiments performed by Karmakar *et al.* [223].

5.1 Simulation setup

The difference in the affinities of NK-2 for anionic DOPG and zwitterionic DOPC bilayers in terms of a shift in the binding free energy, $\Delta\Delta G$, was determined by means of the thermodynamic integration (TI) method according to the thermodynamic cycle described in section 2.3 of the introduction. The transition from DOPC to DOPG was performed by increasing the coupling parameter λ in steps of $\Delta\lambda = 0.05$ for $\lambda \in [0.1, 0.9]$ while $\Delta\lambda = 0.01$ was chosen for $\lambda \in [0, 0.1] \cup [0.9, 1.0]$. To avoid possible singularities due to required dummy atoms, Lennard-Jones and Coulomb interactions were transformed in separate simulations as described in section 2.3. For $\lambda \in [0, 0.1] \cup [0.9, 1.0]$ data were collected from 180 ns simulations whereas the larger step size of $\Delta\lambda = 0.05$ for $\lambda \in [0.1, 0.9]$ made longer simulation times of 360 ns necessary to assure proper sampling. Each particular simulation was first energy minimized using the steepest descent method and equilibrated for 20 ns.
The initial configuration of NK-2 was derived from the solution structure of NK-lysin as obtained from NMR spectroscopy and stored in the RCSB [1] protein data bank (PDB entry: 1NKL [137, 180]). Its initial structure features two α-helices separated by a kink as shown in figure 5.1. This configuration was chosen as the peptide is, as many antimicrobial peptides, known to reorganize into $\alpha-$helical configurations if adsorbed to a bilayer surface [140, 142]. The peptide was added to a DOPC bilayer by placing it within a hole with a radius of 1.5 nm pervading the bilayer as depicted in figure 5.1 (*left*). Hereby the peptide was orientated such that its hydrophobic side chains face the bilayers' nonpolar hydrocarbon tails whereas the hydrophilic side chains pointed toward the polar headgroups. The corresponding bilayer coordinates were downloaded from the lipid bilayer library of the CHARMM[2] graphical user interface [224, 225]. Initially the system was simulated for 20 ps restraining the coordinates of all peptide atoms, succeeded by an additional 9 ns simulation with the peptide helicity being stabilized using distance restraints. The N-terminus of the peptide was pulled towards the upper bilayer leaflet during 600 ps. Finally, the system was equilibrated for 100 ns resulting in the configuration shown in figure 5.1 (*right*). This configuration served as starting point for the alchemical transformation of DOPC to DOPG in presence of the NK-2 peptide. Several times during building up the initial setup water molecules had to be removed manually from the bilayer interior. In several previous attempts with the peptide initially located in the aqueous solution the peptide showed little tendency to attach to the DOPC bilayer indicating a very small affinity for DOPC.

[1] **R**esearch **C**ollaboraty for **S**tructural **B**ioinformatics
[2] **C**hemistry at **HAR**vard **M**acromolecular **M**echanics

The bilayer consisting of 128 DOPC or DOPG lipids, respectively, was sol-

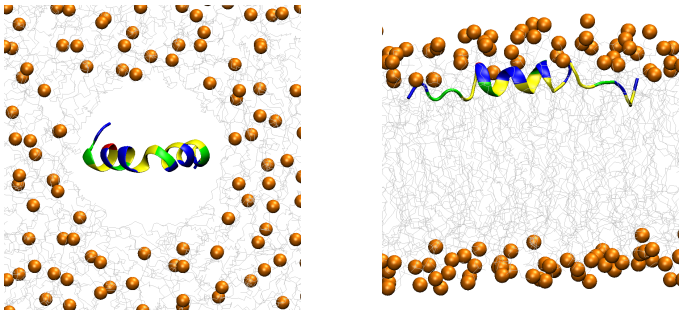

Figure 5.1: NK-2 peptide in helix-kink-helix structured state positioned in a water pore within a DOPC bilayer (*left*) chosen as the initial configuration and after 100 ns equilibration (*right*). Lipids are shown in gray, headgroup nitrogens in orange, polar residues in green, nonpolar residues in yellow, cationic residues in blue and anionic ones in red. The peptide is depicted in *ribbon* representation.

vated by adding 8956 SPC[3] water molecules in presence and 5354 SPC[3]water molecules in absence of the peptide. Both systems include 128 solvated dummy atoms which were transformed to Na^+ ions for $\lambda = 1$, then serving as counter ions of the anionic DOPG bilayer. The electric charge of the cationic peptide was compensated by ten Cl^- ions.
The NK-2 peptide and the phospholipids were described using the united-atom GROMOS96[4] force field ffG53a6 [186] and separately coupled to a velocity rescale [182] thermostat with a relaxation time of 0.1 ps maintaining a temperature of 310 K. An average pressure of 1 atm parallel and normal to the bilayer was maintained using a Berendsen barostat [183] with a relaxation time of 0.5 ps. For all simulations a time step of 2 fs was applied. Long-range electrostatic interactions were calculated using particle mesh Ewald summation [184, 185].

[3] **S**imple **P**oint **C**harge
[4] **GRO**ningen **MO**lecular **SIM**ulations

5.2 Results

5.2.1 Secondary structure and position

Although the peptide is assumed to organize into α-helical structures in the lipid bilayer environment the preformed helical structure was observed to partially or completely unfold as shown in figure 5.2. In case of DOPC the unwrapping comprised the residues Val6-Thr13 and started after 60 ns whereas for DOPG the complete peptide adopts only coil, bend and turn conformations after about 380 ns. Time evolutions of the peptide's secondary structure are shown in section A.3 of the appendix. The unfolding of the peptide could be an artifact of the chosen force field, GROMOS53a6, which is known to artificially destabilize α-helical conformations whereas, on the other hand, it is parameterized to match solvation free enthalpies of polar amino acid side chains which might be important for the accuracy of our free energy calculations. [186].

As indicated from the mass density profiles of the peptide attached and pure

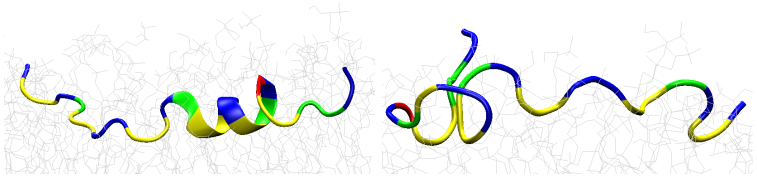

Figure 5.2: Snapshots of NK-2 attached to a zwitterionic DOPC (*left*) and an anionic DOPG bilayer (*right*) after 400 ns of simulation. Lipids are depicted in gray, hydrophobic residues in yellow, hydrophilic ones in green, cationic ones in blue and anionic residues in red. Peptides are shown in *ribbon* presentation.

DOPC and DOPG bilayers shown in figure 5.3 we observe stable bilayers for all four systems with no water molecules being present in the bilayer core region. The profiles show well defined hydrocarbon tail and lipid headgroup regions as indicated from the mass densities of the headgroup phosphor atoms. Interestingly, only for the DOPC bilayer in absence and presence of the peptide, a shoulder in the water density was found. Its position corresponds to the peak of the phosphor atom density indicating a higher hydration of the PC head groups. This effect is accompanied by a corresponding enlarged area per lipid as well as a decrease in the bilayer thickness shown in table 5.1 and may be explained by the larger polarity of the PC headgroup as the negatively charged phosphor group is screened by the positively charged choline nitrogen group in a distinct distance. On the other hand, in case of DOPG, the charge of the phosphor group is directly neutralized by the Na^+ counter cations as indicated by the large overlap in the corresponding density profiles. The peptide density shows a very large

overlap with the phosphor atoms. This holds especially true for the hydrophilic residues whereas the hydrophobic residues rather reside in the nonpolar carbon tail region. For DOPC the peptide density exhibits a slightly broader shape compared to DOPG suggesting more translational freedom along the bilayer normal for the peptide. This may at least partially be explained by the peptide's weaker electrostatic interactions with the zwitterionic PC head group.

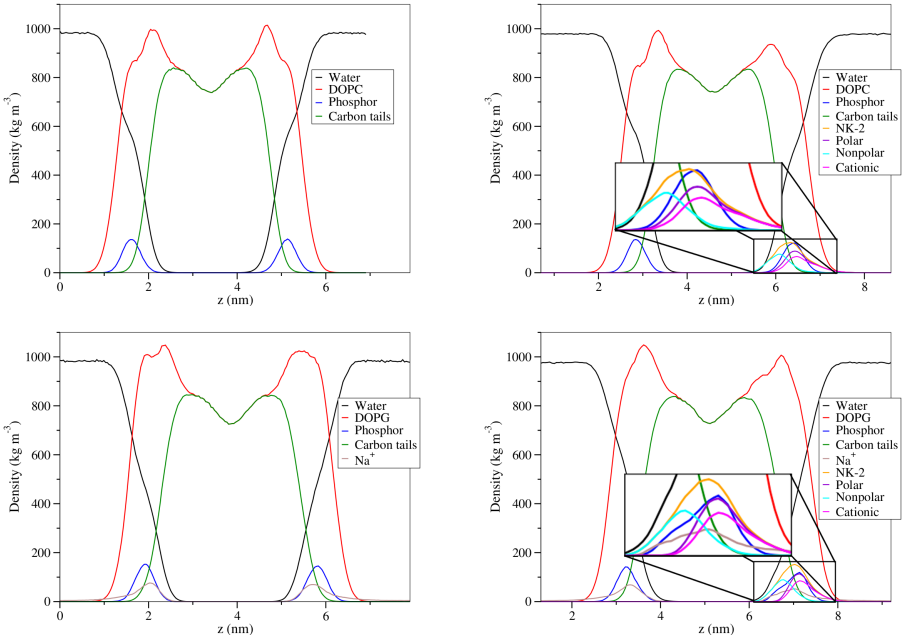

Figure 5.3: Mass density profiles for DOPC (*top*) and DOPG (*bottom*) in absence (*left*) and presence (*right*) of NK-2 averaged over 50 ns. Water is shown in black, DOPC and DOPG in red, headgroup phosphor atoms in blue, carbon tails in light green, Na^+ ions in brown and NK-2 in orange. In addition, hydrophobic residues (isoleucine, leucine, glycine, valine, cysteine, methionine, and phenylalanine) are colored purple, hydrophilic ones (lysine, arginine, threonine, serine, and asparagine) are depicted in cyan, and the cationic residues lysine and arginine in magenta.

Interestingly, only for DOPG, a broadening of the phosphor density peak corresponding to an increased roughness and therefore a spatial disturbance of the headgroup region was caused by the adsorption of NK-2. An explanation might be given by the strong interaction of the cationic peptide residues with the anionic PG head group. During the folding and organization processes the corresponding peptide residues may partially drag the lipid head groups leading to an increased disorder in their spatial distribution normal to the bilayer. At high peptide concentrations this might lead to bilayer disruption in accordance with the

		a_l in nm^2	$d_{P\text{-}P}$ in nm
DOPC	pure	0.73 ± 0.001	3.45 ± 0.06
	NK-2	0.76 ± 0.001	3.49 ± 0.05
DOPG	pure	0.65 ± 0.002	3.84 ± 0.15
	NK-2	0.65 ± 0.003	3.75 ± 0.05

Table 5.1: Area per lipid, a_l, and bilayer thickness as obtained by the distance between the center of masses of the phosphor atoms of the two leaflets, $d_{P\text{-}P}$.

carpet model [226]. This suggests that the higher antimicrobial activity of NK-2 towards anionic lipid bilayers may not only be explained by its larger binding affinity but also by an increased capability to disrupt anionic rather than zwitterionic bilayers and therefore a larger propensity to intrude into anionic bilayers. Additionally, we observed, in accordance with experimental results [143] a very slight thinning of the DOPG bilayer due to the attached NK-2 peptide whereas the thickness of the DOPC bilayer remains unchanged within the error margins.

5.2.2 Binding affinities from simulations

Our simulations indicate that the cationic NK-2 peptide binds much more strongly to the anionic DOPG than to the zwitterionic DOPC bilayer. The TI calculations yield a difference in the binding affinity of NK-2 for DOPG and DOPC bilayers of

$$\boxed{\Delta\Delta G_{\mathrm{PC}\to\mathrm{PG}} = \Delta G_{\mathrm{PG}} - \Delta G_{\mathrm{PC}} = -54.4 \pm 21.8 \text{ kJ/mol.}}$$

Here, the difference in the free energy between two neighboring states associated with a particular λ was calculated using the Bennett acceptance ratio method [159] as described in section 2.3 whereas the statistical error was determined by dividing the trajectory in 20 ns blocks and determining the corresponding standard error. This method refers to as block averaging.
In a comparable study von Deuster and Knecht estimated the difference in the binding affinity $\Delta\Delta G$ of the NK-2 peptide for anionic palmitoyl-oleoyl-phosphatidyl-glycerol (POPG) compared to zwitterionic palmitoyl-oleoyl-phosphatidyl-choline (POPC) lipid bilayers using MD simulations in conjunction with the thermodynamic integration (TI) method [145]. Differing from our atomistic description von Deuster and Knecht applied a rather simple coarse grained representation by use of the MARTINI force field. They obtained a value of $\Delta\Delta G = -56 \pm 6$ kJ/mol which is in good agreement with our results. Both investigated systems are quite similar as the POPC and DOPC as well as

POPG and DOPG lipids are only slightly distinguished in their hydrocarbon tail composition. DOPC as well as DOPG lipids exhibit two mono-unsaturated allyl tails featuring 18 hydrocarbons whereas one of the alkyl tails of POPC and POPG is completely saturated and merely contains 16 hydrocarbons. The comparably large statistic uncertainty of our results is based on the more detailed and therefore more complex description of our system. Here, in particular the use of dummy atoms which were not required in the coarse grain model play a crucial role as described in section 2.3.1 of the introduction.

5.2.3 Comparison with electrophoresis experiments

The difference in the binding affinities $\Delta\Delta G_{\mathrm{PC}\to\mathrm{PG}}$ obtained from our simulations might be compared to zeta potentials inferred from electrophoretic mobilities of lipid vesicles at various NK-2 concentrations. The electrophoretic mobility is the drift velocity of a particle suspended in a liquid due to an external static and homogeneous electric field, normalized by the field intensity. The drift of the particle arises due to its surface charge. The surface charge of the dispersed particle is partially screened by a layer of rather tightly bound counter ions. This layer refers to as the Stern plane and is furthermore surrounded by a diffusive layer of a majority of counter and a minority of co-ions. The zeta potential is the electrostatic potential at the shear plane with respect to the bulk phase. At the shear plane the Stern plane turns into the diffusive layer of counter and co-ions. According to the Smoluchowski equation the zeta potential is proportional to the electrophoretic mobility [227].
Karmakar *et al.* investigated the effect of NK-2 on zeta potentials of large unilamellar DOPG, DOPC, and DOPC/DOPG (4:1) vesicles (LUV) with a diameter of about 20 nm [223]. The zeta potentials in dependence of NK-2 concentrations are depicted in figure 5.4. For zwitterionic DOPC as well as for anionic DOPG vesicles negative zeta potentials are observed in absence of the peptide where the value for DOPG ($\zeta = -61.1 \pm 17.9$ mV) is much lower than for DOPC ($\zeta = -10.6 \pm 9.9$ mV) as expected from the negative charge of the DOPG lipids. The slightly negative value within the range of error for DOPC may be explained by negative ions binding to positive choline groups representing the most solution exposed moiety of the lipid. Willumeit *et al.* reported zeta potentials of $\zeta = 2.3 \pm 2.0$ mV for pure DPPC and $\zeta = -56.0 \pm 2.2$ mV for pure DPPG vesicles [143]. The completely saturated hydrocarbon tails of DPPG and DPPC (16 hydrocarbons per tail) are slightly shorter than the ones of DOPC and DOPG (18 hydrocarbons per tail). It has to be noted that DOPC and DPPC as well as DOPG and DPPG differ remarkably in their main phase transition temperature, T_{m}. For DPPC and DPPG $T_{\mathrm{m}} = 314$ K whereas T_{m} is

much lower for DOPC ($T_{\mathrm{m}} = 253$ K) and DOPG ($T_m = 255$ K). As the study from Karmakar as well as from Willumeit were performed at room temperature ($T = 298.15$ K), DOPC and DOPG vesicles were investigated in the liquid but DPPG and DPPC liposomes in the gel phase.

For anionic DOPG, DPPG and DOPC/DOPG as well as for zwitterionic

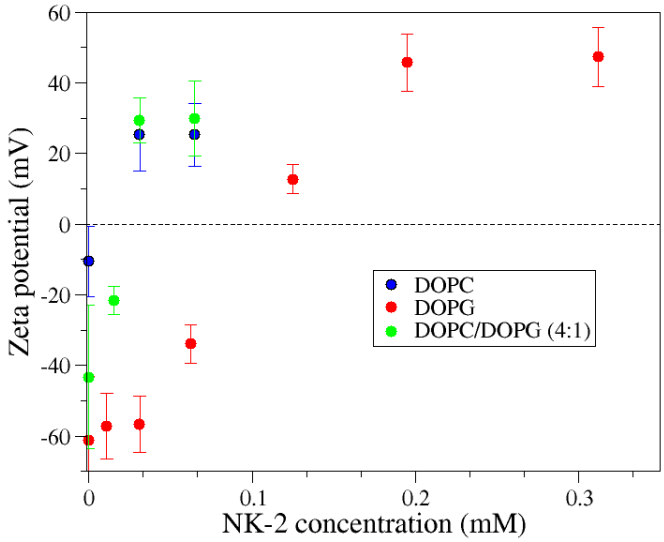

Figure 5.4: Zeta potential for DOPC, DOPG, and DOPC/DOPG vesicles attached by NK-2 peptides inferred from electrophoresis experiments by Karmakar *et al.* [223].

DOPC vesicles charge neutralization and even charge overcompensation and saturation is observed upon addition of cationic NK-2 peptides [143, 223]. The lipid bilayer-peptide interaction thus seems to be driven by electrostatic as well as hydrophobic interactions. Charge overcompensation was not reported for DPPC.

In this section we use these zeta potentials to determine the binding free energies of NK-2 for DOPC, DOPG and DOPC/DOPG vesicles. We first describe the corresponding ansatz published by von Deuster and Knecht [146] and subsequently present inferred binding free energies and area densities of membrane bound peptides. The latter give insight about the interaction between membrane bound peptides. The results are finally discussed and compared with results obtained from our simulations.

Ansatz

The ansatz to determine the binding affinity of a charged peptide for particular lipid vesicles or membranes is based on the change of the membrane surface charge $\Delta\sigma$ as mediated by peptide adsorption. The change of the surface charge $\Delta\sigma$ is obtained from the inferred zeta potential as described below. By means of $\Delta\sigma$ it is possible to determine the concentration of bound peptides c_s which depends on the peptide concentration in the bulk solution, c, and the binding free energy, ΔG. In the following we first derive this relation and then describe the estimation of $\Delta\sigma$ from zeta potentials.

The relation between the number of peptides adsorbed to the bilayer surface, N_s, and the number of peptides in the bulk, N_b, can be described by the free energy difference between both corresponding thermodynamic states as

$$N_\mathrm{s} = N_\mathrm{b} \cdot \exp\left(-\beta\left(\Delta G - T\Delta S\right)\right). \tag{5.1}$$

Here, ΔG denotes the binding affinity, $\beta = 1/(k_\mathrm{B}T)$, k_B the Boltzmann constant, and $T = 298$ K the temperature. The term $-T\Delta S$ refers to the contribution arising from the difference in the translational entropy of the peptide in bulk and adsorbed at the bilayer. This term can be estimated from the peptide accessible volume in bulk, V_b, and at the membrane, V_s, according to

$$-T\Delta S = -k_\mathrm{B}T \log\left(\frac{V_\mathrm{s}}{V_\mathrm{b}}\right). \tag{5.2}$$

Assuming that the vast majority of peptides within the sample resides in the bulk phase,

$$c \approx c_\mathrm{b}\,, \tag{5.3}$$

with the average peptide concentration $c = (N_\mathrm{s} + N_\mathrm{b})/V$ and the sample volume $V \approx V_\mathrm{b}$. Equations 5.1 and 5.2 result in

$$\begin{aligned} c_\mathrm{s} &= c \cdot \exp\left(-\beta\Delta G\right) \\ \Leftrightarrow \Delta G &= -k_\mathrm{B}T \log\left(\frac{c_\mathrm{s}}{c}\right). \end{aligned} \tag{5.4}$$

The concentration of bound peptides, c_s, can be expressed as $c_\mathrm{s} = N_\mathrm{s}/V_\mathrm{s} = \Gamma/\Delta z$ with the area density of bound peptides $\Gamma = N_\mathrm{s}/A$. Here, A denotes the complete vesicle surface and Δz the accessible space of the peptide normal to the surface. The latter might be taken as the standard deviation of the peptides' center of mass position normal to the bilayer as obtained from MD simulations. The described ansatz implies that an adsorbed peptide is not restricted in its translation along the bilayer surface. Thus, especially if the peptides are prone to aggregation the surface area available for each peptide, A_p, has to be large compared to

the surface area covered by a single peptide, a_p. Hence,

$$A_\mathrm{p} \gg a_\mathrm{p}. \tag{5.5}$$

The adsorption of charged peptides results in a change of the vesicle surface charge, $\Delta\sigma$, depending on the area density of bound peptides, Γ, and the charge of the peptide, q_p, according to

$$\Delta\sigma = q_\mathrm{p}\Gamma = q_\mathrm{p} c_\mathrm{s} \Delta z. \tag{5.6}$$

The surface charge, σ, and the surface potential, ψ_0, are related via

$$\sigma = \sqrt{8\varepsilon_0\varepsilon_\mathrm{r} k_\mathrm{B} T c_\mathrm{el}} \sinh\left(\frac{ze\psi}{2k_\mathrm{B}T}\right). \tag{5.7}$$

This relation is denoted as Grahame equation and obtained from the Gouy-Chapman theory (Poisson-Boltzmann theory in one dimension) [228]. Here, ε_r is the relative permittivity of the solution, ε_0 the vacuum permittivity, c_el the electrolyte concentration, e the elementary charge, and $z = +1$ the charge number of counter ions. Approximately we determined the surface charge, σ, by the electrostatic potential at the shear plane, the zeta potential, replacing the potential at the surface, ψ_0. For phospholipid vesicles in alkali metal chloride solutions the shear plane was found to be located in about 2 Å distance from the bilayer surface as obtained by fitting the Stern equation to zeta potentials inferred from electrophoresis experiments [229]. This approach to determine the surface density, σ, from the Zeta potential, ζ, has recently been verified by MD simulations by Knecht and Klasczyk [230, 231].

Evaluation

Understanding the binding affinities from zeta potentials via equation 5.4 requires to account for the partial compensation of the vesicle surface charge by counter ions bound to the lipids. The adsorption of a peptide whose charge is complementary to that of the surface leads to a release of counter ions which decreases the effective charge, q_p, of the peptide. The number of released counter ions per peptide, N_ri, may be estimated from the fraction of lipids binding a counter ion, α, and the number of lipids covered by a peptide, N_lc, as

$$N_\mathrm{ri} = \alpha N_\mathrm{lc}. \tag{5.8}$$

To compute N_lc we assume that the peptide adopts an α-helical structure at the membrane. The thickness of an α-helix is typically $D = 0.54$ nm whereas the average length per amino acid is $L = 0.15$ nm. Thus, the area covered by a 26 residue peptide as NK-2 adsorbed to the membrane can be estimated as

$a_p = 26 \cdot D \cdot L \approx 2.1$ nm^2. The number of lipids covered by the peptide, N_{lc}, can be determined by the area per lipid, a_l, from

$$N_{lc} = a_p / a_l.$$

The fraction of lipids being charge neutralized due to the binding of a counter ion, α, might be computed by the number of lipids, N_{lq}, including exactly one lipid featuring an unscreened charge

$$\alpha = \frac{N_{lq} - 1}{N_{lq}}. \tag{5.9}$$

The next step is to estimate the surface concentration, Γ_{lq}, of lipid charges, q_l, by

$$\Gamma_{lq} = \frac{\sigma}{q_l}. \tag{5.10}$$

Equation 5.10 allows to calculate the surface area $a_{lq} = 1/\Gamma_{lq}$ exhibiting exactly the charge of one lipid. The surface charge σ is determined from the zeta potential via equation 5.7 applied for the peptide-free case $c = 0$ mM. From the area per lipid, a_l, and $N_{lq} = a_{lq}/a_l$, the fraction of lipids absorbing a counter ion, α, can be computed via equation 5.9. The number of counter ions released upon binding of a peptide is then estimated by equation 5.8 while the effective charge of the peptide, q_p^{eff}, is estimated as $q_p^{eff} = q_p - N_{ri} q_i$ with the peptide net charge q_p and the charge $q_i = +e$ of a single counter ion.
For DOPG we found $\alpha_{PG} = 0.98 \pm 0.01$, leading to a net change of the vesicle charge upon binding of a peptide of $q_p^{eff} = +6.8$ e while for the ratio of ion adsorbing lipids, DOPG, within the DOPC/DOPG mixture $\alpha_{PC/PG} = 0.94 \pm 0.03$ corresponding to $q_p^{eff} = +7.3$ e is obtained. In the latter case it has to be taken into account that only $1/5$ of the lipids are charged and thus the area per charged lipid, a_{lq}, has to be multiplied by this factor. The applied zeta potentials in absence of peptides were inferred as $\zeta_{PG}(c = 0\,\text{mM}) = -61.1\,(\pm 17.9)$ mV for DOPG and $\zeta_{PG/PC}(c = 0\,\text{mM}) = -43.3 \pm (20.3)$ mV for DOPC/DOPG. Furthermore the areas per lipid, a_l, as obtained from our MD simulations shown in table 5.1 were employed. To calculate the area per lipid for DOPC/DOPG we averaged over the according values for DOPC and DOPG considering the mixture ratio 4:1. For the uncharged DOPC vesicles $q_p^{eff} = q_p = +10$ e holds.
The binding affinities inferred from zeta potentials are given in table 5.2. The accessible space of the peptide normal to the surface, Δz, as required in equation 5.6 was estimated to $\Delta z_{PC} = 0.192$ nm for DOPC, $\Delta z_{PG} = 0.163$ nm for DOPG, and $\Delta z_{PC/PG} = 0.186$ nm for DOPC/DOPG. Hereby, $\Delta z_{PC/PG}$ was evaluated by averaging the values Δz_{PC} and Δz_{PG} according to the mixture ratio. Experiments

were conducted at room temperature, $T = 298$ K, in an aqueous solution exhibiting a NaCl concentration of $c_{\mathrm{el}} = 0.6 \pm 0.2$ mM.

The relative permittivity, ε_{r}, in equation 5.7 was set to the value for water at

	c in mM	ζ in mV	ΔG in kJ/mol
DOPC	0	-10.6 ± 9.9	-14.7 ± 1.0
	0.0312	25.4 ± 10.4	
DOPG	0.0312	-56.7 ± 8	-15.3 ± 0.4
	0.1248	12.7 ± 4.1	
DOPC/PG (4:1)	0.0156	-21.6 ± 4.02	-18.2 ± 0.4
	0.0312	29.4 ± 6.4	

Table 5.2: Zeta potentials, ζ, for different NK-2 concentrations, c, as taken from [223] as well as binding free energies, ΔG, obtained from equation 5.7 and 5.4.

room temperature, $\varepsilon_{\mathrm{r}} = 78$.

In order to validate condition 5.3, the total concentration of bound peptides within the sample, c_{ts}, was computed from

$$c_{\mathrm{ts}} = \Gamma \cdot \frac{a_{\mathrm{l}} \cdot c_{\mathrm{l}}}{2} \, .$$

Here, $c_{\mathrm{l}} = 0.65$ mM is the concentration of lipids within the sample and a_{l} the area per lipid. The second term $a_{\mathrm{l}} c_l / 2$ is the concentration of accessible lipid area within the sample. The factor $1/2$ takes into account that the inner lipid monolayer of the vesicle is inaccessible to the peptide. For all investigated systems the ratio between the concentration of peptides in bulk, $c_{\mathbf{b}} = c - c_{\mathrm{ts}}$, and the concentration of peptides within the whole sample, c, was found to be $c_{\mathbf{b}}/c > 0.96$. The condition 5.3 is therefore always fulfilled.

The prerequisite 5.5 was tested by computing the lipid area containing exactly one adsorbed peptide $A_{\mathrm{p}} = 1/\Gamma$ and comparing it to the surface area covered by a single peptide, $a_{\mathrm{p}} = 2.1$ nm^2. Hereby a_{p} was estimated by considering an α-helix consisting of 26 residues as described above. For all systems and for all studied peptide concentrations $A_{\mathrm{p}}/a_{\mathrm{p}} > 111$ was found. Condition 5.5 is therefore fulfilled.

Area density of bound peptides

The interaction between membrane bound peptides is crucial for the activity of antimicrobial peptides. As described in section 1.4 of the introduction depends the propensity of antimicrobial peptides to induce membrane pores and membrane disruption strongly on the corresponding peptide/lipid ratio.

The interaction between membrane bound peptides may be described by a potential, $V(r) = \gamma q_p^2 v(r)$, depending on the charge of the peptide, q_p, a positive factor, $\gamma > 0$, scaling the strength of the interaction, and a positive strictly monotonically decreasing function, $v(r) > 0$, which depends on the distance between two peptides, r. Furthermore $v(r) \to 0$ for $r \to \infty$ is assumed. A potential which fulfills these conditions and which is physically plausible would be provided by the Coulomb potential with an effective dielectric constant for the water-membrane interface. The peptide-peptide interaction can be neglected for low concentrations of membrane bound peptides. This is crucial for the determination of peptide binding affinities for particular vesicle species and is expressed in the condition 5.5. The concentration of membrane bound peptides increases with its bulk concentration until it saturates. In this case the concentration of membrane bound peptides is maximal. We assume for simplicity that in saturation the peptides arrange on a quadratic lattice and that each peptide is surrounded by four nearest neighbors in a distance of $r_{\min}$. Under these conditions the equation

$$\Delta G + 4\gamma q_p^2 v(r_{\min}) = 0 \tag{5.11}$$

holds. Thus, $r_{\min}$ can be determined via

$$r_{\min} = v^{-1}\left(\frac{-\Delta G}{4\gamma q_p^2}\right). \tag{5.12}$$

The inverse function $v^{-1}(\cdot)$ of $v(\cdot)$ is strictly monotonically decreasing. Furthermore we assume $v^{-1}(\cdot) > 0$. As $\Delta G < 0$ on the right side of equation 5.12, $r_{\min}$ decreases if the charge of the peptide q_p decreases. For a quadratic lattice the area density of membrane bound peptides Γ^s may then be estimated from

$$\Gamma^s = \frac{1}{r_{\min}^2}. \tag{5.13}$$

As described in section 5.2.3 the adsorption of NK-2 to the DOPG vesicles leads to a release of counter ions bound to the lipids and hence to a decrease in the effective net charge of the peptide, $q_p^{\text{eff}} = +6.8$ e. As the distance $r_{\min}$ decreases with the peptide charge an increase of the area density of membrane bound peptides Γ^s in saturation may be expected. The area density Γ^s can be determined via equations 5.6 and 5.7 using the zeta potentials obtained in absence of peptides ($c = 0$ mM) and in saturation.
In absence of peptides $\zeta_{PG} = -61.1\,(\pm 17.9)$ mV was inferred for DOPG and $\zeta_{PC} = -10.6\,(\pm 9.9)$ mV for DOPC as apparent from figure 5.4. For saturation Karmakar *et al.* found $\zeta_{PG} = 47.3\,(\pm 8.4)$ mV for DOPG at $c = 0.312$ mM and $\zeta_{PG} = 25.3\,(\pm 8.9)$ mV for DOPC at $c = 0.065$ mM.

Hence, we estimated

$$\Gamma^{\mathrm{s}}_{\mathrm{PG}} = 6.8(\pm 1.8)\cdot 10^{-3}\ \mathrm{nm}^{-2} \qquad \text{for DOPG and}$$
$$\Gamma^{\mathrm{s}}_{\mathrm{PC}} = 1.3(\pm 0.5)\cdot 10^{-3}\ \mathrm{nm}^{-2} \qquad \text{for DOPC.}$$

According to equation 5.13 this corresponds to $r_{\min} = 12.1\,(\pm 1.6)\,\mathrm{nm}$ for DOPG and $r_{\min} = 27.6\,(\pm 5.3)\,\mathrm{nm}$ for DOPC.
In simulations the peptide may be affected by long-range interactions with its periodic image. The distance between the peptide and its closest periodic images is given by the length of the simulation box parallel to the bilayer, $d_{x,y}$. While for simulations of charged peptides in water the interaction between the peptide and its periodic images may be neglected due to ionic screening as well as the comparably high relative permittivity of water ($\varepsilon_{\mathrm{r}} \approx 80$) and $V(r) \propto 1/\varepsilon_{\mathrm{r}}$ for the Coulomb potential this does not necessarily hold true for a peptide located at the interface between the polar headgroup and the nonpolar hydrocarbon region of a bilayer. The former exhibits a rather high relative permittivity parallel to the bilayer, $\varepsilon_{\mathrm{r},\parallel} \approx 210(\pm 30)$, while the relative permittivity of the latter is quite low, $\varepsilon_{\mathrm{r},\parallel} \approx 4(\pm 3)$, as determined from MD simulations for DPPC [232]. Under these conditions the interaction between the peptide and its periodic image might have to be taken into account. According to this, instead of the binding free energy ΔG at infinite low concentrations of membrane bound peptides the free energy ΔG^{bc} including the interaction between the peptide and its four nearest periodic images are computed by our simulations. In accordance with the ansatz described above this leads to

$$\Delta G^{\mathrm{bc}} = \Delta G + 4\gamma q_{\mathrm{p}}^2 v\,(d_{x,y})\,.$$

Hence, for the difference in the binding free energy of NK-2 at DOPG and DOPC the relation

$$\Delta\Delta G^{\mathrm{bc}}_{\mathrm{PC}\to\mathrm{PG}} = \Delta G^{\mathrm{bc}}_{\mathrm{PG}} - \Delta G^{\mathrm{bc}}_{\mathrm{PC}} = \Delta\Delta G_{\mathrm{PC}\to\mathrm{PG}} + 4\gamma v\,(d_{x,y})\left((q^{\mathrm{eff}}_{\mathrm{PG}})^2 - (q^{\mathrm{eff}}_{\mathrm{PC}})^2\right)$$

is obtained. Hereby, $q^{\mathrm{eff}}_{\mathrm{PG}}$ and $q^{\mathrm{eff}}_{\mathrm{PC}} = +10\,\mathrm{e}$ are the effective net charge of the peptide bound to the DOPG and DOPC bilayer, respectively, as obtained from our simulations. For DOPG we inferred $q^{\mathrm{eff}}_{\mathrm{PG}} = +8.5\,\mathrm{e}$ as will be described in section 5.3. As $\gamma > 0$ and $\gamma v\,(d_{x,y}) > 0$ our simulations yield a difference in the binding free energy, $\Delta\Delta G_{\mathrm{PC}\to\mathrm{PG}}$, reduced by a subtrahend of $4\cdot\left(8.5^2 - 10^2\right)\mathrm{e}^2\gamma v\,(d_{x,y}) = -111\,\mathrm{e}^2\gamma v\,(d_{x,y})$ due to the peptide's interaction with its periodic images. As furthermore $d_{x,y} \approx 6.5\,\mathrm{nm} < r_{\min}$ for DOPC as well as for DOPG and the potential $v(r)$ decreases strictly monotonically it can be assumed that the contribution of the peptide-peptide interaction to the determined $\Delta\Delta G^{\mathrm{bc}}_{\mathrm{PC}\to\mathrm{PG}}$ is rather high.

5.3 Discussion

The difference between the affinities of NK-2 for DOPG and DOPC vesicles as obtained from electrophoresis experiments is determined to

$$\boxed{\Delta\Delta G_{\mathrm{PC}\to\mathrm{PG}} = \Delta G_{\mathrm{PG}} - \Delta G_{\mathrm{PC}} = -0.6(\pm 1.12)\ \mathrm{kJ/mol.}}$$

At first sight this result appears rather surprising as NK-2 is highly cationic and the peptide is thus expected to strongly favor complementarily charged DOPG over DOPC vesicles. Instead, NK-2 appears to exhibit the same binding affinity for both vesicle types. Furthermore, our *simulations* indicate a much higher adsorption propensity of NK-2 for DOPG bilayers, $\Delta\Delta G_{\mathrm{PC}\to\mathrm{PG}} = -54.4 \pm 21.8$ kJ/mol. On the other hand, we estimate that in experiment the negative charge of $\alpha_{\mathrm{PG}} = 98(\pm 1)\%$ lipids is neutralized by positive counter ions bound to the lipids. This effect dramatically diminishes the electrostatic attraction of the peptide to the vesicles originated by charge complementarity.
To determine the ratio α_{PG} in our simulations the Na^+ number density was integrated over the bilayer region confined by the Gibbs-dividing surfaces of the two leaflets. The Gibbs-dividing surface approximately corresponds to the shear plane as suggested by MD simulations of a zwitterionic phospholipid (POPC) bilayer exposed to an electric field parallel to the bilayer surface [230]. It is given by the plane where the water density is equal to half of its bulk value. This plane is closely located to the phosphor group region as indicated by the density profiles shown in figure 5.3. In the described manner, from *simulations*, we found that merely 58.3 Na^+ ions bind to a DOPG bilayer comprising 128 lipids. Thus $\alpha_{\mathrm{PG}} = 58.3/128 = 0.46$ corresponding to an effective peptide net charge of $q_{\mathrm{p}}^{\mathrm{eff}} = +8.5$ e was estimated.
The obtained comparably low ratio of bound counter ions might result from force field inaccuracies as for example mediated by the underestimation of the charge of PO_4^- groups within the PG head groups. Tolokh *et al.* reported a ratio of 27% of membrane bound Na^+ ions using the CHARMM force field [233] whereas for the GROMOS force field a ratio of about 60% was found [234]. On the other hand, it has to be taken into account that the number of lipids charge neutralized by bound counter ions depends on the concentrations of ions, $c_{\mathrm{i,s}}$, at the membrane surface as a higher concentration, $c_{\mathrm{i,s}}$, increases the binding probability. The concentrations $c_{\mathrm{i,s}}$ are different in experiment and simulations. The effect of $c_{\mathrm{i,s}}$ given by a possible difference in boundary conditions should be dissected from the possible difference in the intrinsic binding affinity arising from possible force field inaccuracies. To this aim, the intrinsic binding constant, K_{int}, [235] was compared between simulation and experiment. The intrinsic binding constant K_{int} is related to the fraction of lipids binding an ion, α, the fraction of ion-free lipids, $1-\alpha$, and the concentration of counter ions at the

surface, $c_{\mathrm{i,s}}$, according to

$$K_{\mathrm{int}} = \frac{\alpha}{c_{\mathrm{i,s}}(1-\alpha)}. \tag{5.14}$$

In experiment, the concentration $c_{\mathrm{i,s}}$ can be estimated from the Boltzmann relation [229] as

$$c_{\mathrm{i,s}} = c_{\mathrm{i,b}} \exp\left(-ze\beta\psi_0\right). \tag{5.15}$$

Hereby, $c_{\mathrm{i,b}} = 0.6 \pm 0.2$ mM is the concentration of ions in the bulk, $z = +1$ the charge number of the counter ions, e the elementary charge, $\beta = 1/(k_{\mathrm{B}}T)$, k_{B} the Boltzmann constant, and T the temperature. The value of $c_{\mathrm{i,s}}$ was estimated by replacing the surface potential ψ_0 in equation 5.15 by the zeta potential. For DOPG with $\zeta(c = 0\ \mathrm{mM}) = -61.9\ (\pm 17.9)$ mV in the absence of peptides (also employed to determine α as described above) $c_{\mathrm{i,s}} = 3.8(\pm 3.0) \cdot 10^{-3}$ nm^{-3} was obtained. With $\alpha = 0.98\ (\pm 0.01)$ the experimental intrinsic binding constant is estimated as $K_{\mathrm{int}} = 1.27(\pm 1.17) \cdot 10^4$ nm^3. For our simulations, $c_{\mathrm{i,s}}$ might be approximated by the number density of Na^+ ions at the aforementioned Gibbs-dividing surface. Here, a Na^+ concentration of $c_{\mathrm{i,s}} \approx 1.9$ nm^{-3} and thus with $\alpha = 0.46$ as described above $K_{\mathrm{int}} \approx 0.45$ nm^3 is obtained.
Two effects are therefore identified to cause the large discrepancy between $\Delta\Delta G_{\mathrm{PC}\to\mathrm{PG}}$ obtained from simulations and experiment: on the one hand, the interaction of the peptide with its periodic images as described in section 5.2.3, and on the other hand, the underestimation of the intrinsic binding constant for the association of counter ions with the lipids. Furthermore it has to be noted that in experiment the charge of the peptide itself might be compensated by counter ions which would decrease its effective charge even further.
Interestingly, we found that NK-2 binds even more strongly to DOPC/DOPG than to pure DOPG vesicles,

$$\boxed{\Delta\Delta G_{\mathrm{PC/PG}\to\mathrm{PG}} = \Delta G_{\mathrm{PG}} - \Delta G_{\mathrm{PC/PG}} = +2.9(\pm 0.6)\ \mathrm{kJ/mol.}}$$

This might result from a slightly lower fraction of DOPG lipids charge neutralized by bound counter ions. For DOPG we obtained $\alpha_{\mathrm{PG}} = 98 \pm 1\%$ and for the fraction of DOPG lipids within DOPC/DOPG (4:1) vesicles $\alpha = 94 \pm 3\%$. Although both values agree within the error range the values suggest that α might be slightly lower for DOPC/DOPG. This may result from the lower surface charge of the vesicle and therefore a smaller density of cations at its shear plane, leading to a decrease in the probability of counter ion binding.

5.4 Conclusion

We have investigated the affinity of the antimicrobial NK-2 peptide for anionic DOPG and zwitterionic DOPC lipid bilayers by means of MD simulation in combination with the thermodynamic integration (TI) method. Furthermore we compared our results with the affinities of NK-2 for DOPC, DOPG and mixed DOPC/DOPG vesicles as obtained by analysis of zeta potentials inferred from electrophoresis experiments. Interestingly, we found that simulations predict a much stronger adsorption of the peptide to DOPG bilayers whereas electrophoresis experiments indicate a similar propensity of the peptide to attach to DOPC or DOPG vesicles. We explain this unexpected finding by counter ions bound to the charged lipids which largely compensate the anionic charge of the DOPG vesicles, an effect which appears to be underestimated by the simulations.

Our findings might be of large importance for the understanding of the modes of action of antimicrobial peptides as they suggest that the selective activity of the peptides against pro- but not eukaryotic cells may not simply be explained by different binding affinities of the peptides for pure plasma cell membranes. On the other hand, in saturation we inferred an about fivefold higher area density of membrane bound peptides for DOPG compared to DOPC. This increased area density results from a lower peptide-peptide-interaction due to the compensation of cationic peptide charges by anionic lipids. The area density of membrane bound peptides correlates with the peptide/lipid ratio which is crucial for the propensity of antimicrobial peptide mediated pore formation in membranes as described in section 1.4 of the introduction.

Another crucial aspect which differentiates prokaryotic from eukaryotic cell membranes is the cholesterol content. Cholesterol accounts typically for $20-25\%$ of all lipid molecules within plasma cell membranes of vertebrate eukaryotes whereas it is not present in prokaryotes [236]. It strongly interacts with the surrounding lipids inducing a higher lateral lipid order and increased packing density. This decreases the lipid fluidity and the membrane permeability for small polar molecules as for example water. These effects might as well decrease the pore formation propensity of eukaryotic cell membranes yielding an additional explanation for the reduced activity of antimicrobial peptides here [237].

6

Summary

In this PhD thesis molecular dynamics simulations (MD) have been employed to investigate the mutual influence between peptides and model membranes. In particular the impact of (i) air-water interfaces on the folding behavior of Aβ monomers associated with Alzheimer's disease, (ii) the effect of these monomers on the formation and stability of phospholipid bilayer defects like water pores, and (iii) the difference in the affinity of the antimicrobial peptide NK-2 for zwitterionic and anionic phospholipid bilayers have been studied.

As to (i), the secondary structures of the alloforms Aβ_{40} and Aβ_{42} at pH 5 and pH 7 in presence and absence of an air-water-interface were examined. Here, for both peptides we observe a decrease in the amount of β-structures in aqueous solution at pH 5 compared to physiological pH conditions. A comparable decrease was not observed at an air-water-interface where the fraction of β-structures does not remarkably change upon a decrease in pH. On the other hand, for all systems especially the hydrophilic N-terminus shows a comparable low propensity to form β-sheets or -bridges at pH 5. The N-termini of both peptides contain three histidine residues whose positive charge at pH 5 might promote the interaction between nearby residues resulting in stable helical motifs (Aβ_{42}) or increase the polarity and thus the segment's water solubility (Aβ_{40}). Our findings confirm studies indicating that the higher aggregation propensity of Aβ under slightly acidic compared to pH neutral conditions is rather caused by the peptide's vanishing net charge and thus the absence of electrostatic repulsion than by the formation of aggregation prone

monomer structures [191].
For Aβ_{40} the presence of an air-water-interface diminishes the formation of β-sheets and -bridges which suggests that the higher β-sheet content of Aβ_{40} at air-water-interfaces as detected by infrared reflection-absorption spectroscopy (IRRAS) by Schladitz *et al.* [188] is provoked by peptide-peptide interactions promoted by adjusted peptide orientations or increased peptide densities at the interface. In case of Aβ_{42} the β-structure content is either higher (pH 5) or similar to the one in bulk solution (pH 7). This difference to Aβ_{40} may be explained by the additional two hydrophobic residues which increase the peptide's tendency to locate its hydrophobic C-terminus directly at the interface and might play a role in the difference in aggregation propensities between the peptides in membrane environments and thus their toxicities *in vivo*.
As our studies indicate that peptide-peptide interactions might be crucial for the adoption of aggregation prone conformations provoked by air-water-interfaces or pH conditions close to the peptide's isoelectric point it would be enlightening to perform similar studies for small oligomers like dimers or trimers. Hereby it might be necessary to employ enhanced sampling methods like accelerated [238] and discrete [239] MD simulations or the replica exchange method [206].

As to (ii), the free energy of water pores in zwitterionic phospholipid bilayers (DPPC) attached by an Aβ_{42} monomer was determined by means of the umbrella-sampling method. The comparison with a peptide-free reference system revealed that the adsorption of an Aβ_{42} monomer dramatically increases the pore density and durability but also decreases the pore size. The latter is indicated from a diminished unidirectional flux of water molecules through the pore. Pore mediated water permeabilities as well as pore opening rates are comparable for both systems.
Furthermore for the peptide-free reference system we determined lipid flip-flop waiting times which were found to be in accordance with experimental results. For this system we argued that the evaluation of our simulations are an improvement to a former similar study by Tieleman and Marrink [215].
The higher propensity for pore formation observed for the Aβ_{42} adhered bilayer might be explained by an effective lowering of the dielectric barrier provided by the nonpolar bilayer core region. This finding is in accordance with studies from Sokolov *et al.* [110, 240] who suggested that rather the general disturbance of membrane integrity than the formation of single calcium channels might play the major role in Aβ mediated calcium dyshomeostasis. Sokolov *et al.* proposed that surface attached Aβ oligomers increase the area per lipid leading to a penetration of water molecules into the nonpolar bilayer region and thus to

an increase of its effective dielectric constant. Our simulations rather indicate that the Aβ peptide locally dislocates polar head groups into the bilayer tail region which furthermore facilitates the intrusion of water molecules into the membrane indicated from comparably high densities and stabilities of small water pores. These both effects decrease the effective dielectric constant of the bilayer core region mediating a higher ion permeability of the bilayer. Here, it has to be noted that Sokolov *et al.* observed an increased ion current through lipid bilayers only in presence of Aβ oligomers ($\sim 90 - 110$ kDa [240]) but not monomers (~ 4.5 kDa). As we already observed a strong effect of Aβ_{42} monomers on the integrity of the bilayer as well as the frequency and stability of water pores it would be very interesting to perform comparable simulation studies with small toxic Aβ-oligomers like tetramers or pentamers.
Furthermore the role of the lipid composition of the bilayer on the free energy and stability of water pores might be investigated. Here especially the interaction between Aβ and anionic phosphatidylinositol (PI) lipids might be important for a deeper understanding of Alzheimer's disease as a higher PI content has been observed in membranes within disease affected brain regions like the frontal and temporal cortex or the hippocampus [241].

As to (iii), the free energy difference for the transfer of the peptide NK-2 from an anionic (DOPC) to a zwitterionic (DOPG) phospholipid bilayer was determined by means of atomistic MD-simulations in conjunction with the thermodynamic integration (TI) method. Our simulations indicate a much higher affinity of the antimicrobial peptide to anionic compared to zwitterionic bilayers. Hereby our results agree well with a comparable simulation study by von Deuster and Knecht [145] using a coarse grained description.
Furthermore we determined the affinity of NK-2 for DOPC, DOPG as well as DOPC/DOPG (4:1) vesicles from zeta potentials inferred from electrophoretic mobilities by Karmakar *et al.* [223]. Unexpectedly, NK-2 showed similar affinities for DOPC and DOPG vesicles which is not in accordance with results from our simulations. This discrepancy may be explained by force field inaccuracies like the underestimation of bilayer adsorbed counter ions or by finite size effects like the interaction between the peptide and its periodic images.
Our interpretation of the experimental results indicate that the comparable affinities of NK-2 for anionic and zwitterionic vesicles are accounted for by the adsorption of counter ions which largely neutralize the charge of the anionic lipids. Thus a higher density of bilayer adsorbed peptides in case of DOPG may rather be explained by weaker peptide-peptide repulsion than by higher membrane binding affinities. This decrease in the electrostatic repulsion between peptides arises due to the partly screening of the positive net charge of the peptide by the

anionic lipids.
In a similar way it might also be desirable to analyze the affinity of NK-2 for other vesicle species like DOPE/DOPG (4:1) or DOPC/DOPE (4:1). The corresponding zeta potentials were already inferred by Karmakar *et al.* [223]. The corresponding areas per lipid, a_l, and the standard deviations of the z-position , Δz, of the membrane attached peptide may be obtained by comparably simple MD simulations. In this simulations it would also be interesting to investigate the influence of the attached peptide on the formation of lipid domains within the mixed bilayer.
Additionally it has to be mentioned that the Grahame equation 5.7 employed to determine surface charges from zeta potentials is strictly only valid for 1:1 electrolytes. Hence in our analysis we neglected the impact of solvated cationic peptides on the strength of the electrolyte. Especially for large peptide concentrations further analysis might be necessary to validate this approximation. An appropriate ansatz was already provided by Grahame in 1947 [242].
It would also be very enlightening to study the role of cholesterol on NK-2 mediated membrane disruption or pore formation within phospholipid bilayers. As a starting point a single NK-2 peptide attached to a pure phospholipid and a phospholipid-cholesterol bilayer may be considered. For both systems the free energy for the transition of the peptide from a parallel to a normal surface orientation might be determined by MD simulations in conjunction with the umbrella sampling technique. Similar simulations were performed by Irudayam and Berkowitz for the antimicrobial peptide melittin within a pure zwitterionic phospholipid bilayer (POPC) [243]. To enhance the sampling of the conformational space of the peptide it might be necessary to employ more sophisticated techniques like the replica exchange umbrella sampling (REUS) instead of the common umbrella sampling method [244].

Glossary

Acronyms

Aβ	Amyloid beta
AD	Alzheimer's disease
ADDL	Amyloid beta derived diffusible ligands
ADI	Alzheimer's disease international
AFM	Atomic force microscopy
AICD	Amyloid precursor protein intracellular domains
AMBER	Assisted model building with energy refinement
ApoE	apolipoprotein E
APP	Amyloid precursor protein
CD	Circular dichroism
CHARMM	Chemistry at Harvard molecular mechanics
CR	Congo Red
CTF	Carboxy-terminal fragment
DNA	Deoxyribonucleic acid
DOPC	Dioleoylphosphatidylcholine
DOPC	Dioleoylphosphatidylglycerol
DPPC	Dipalmitoylphosphatidylcholine
DSSP	Define secondary structure of proteins
EM	Electron microscopy
FTIR	Fourier-transform infrared spectroscopy
GROMACS	Groningen machine for chemical simulations
GROMOS	Groningen molecular simulations

HFIP	Hexafluoroisopropanol
IRRAS	Infrared reflection-absorption spectroscopy
LINCS	Linear constraint solver
LPS	Lipopolysaccharides
LUV	Large unilamellar vesicle
MD	Molecular dynamics
NK	Natural killer
NMR	Nuclear magnetic resonance
OPLS	Optimized potential for liquid simulations
PC	Phosphatidylcholine
PDB	Protein data bank
PE	Phosphatidylethanolamine
PG	Phosphatidylglycerol
PI	Phosphatidylinositol
PME	Particle mesh Ewald
PMF	Potential of mean force
POPC	Palmitoyloleoylphosphatidylcholine
POPE	Palmitoyloleoylphosphatidylethanolamine
POPG	Palmitoyloleoylphosphatidylglycerol
RCSB	Research collaboraty for structural bioinformatics
REUS	Replica exchange umbrella sampling
RMSD	Root mean square deviation
RNA	Ribonucleic acid
ROS	Reactive oxygen species
SDS	Sodium dodecyl sulphate
SFV	Sum-frequency vibrational
SPC	Simple point charge
SSNMR	Solid-state nuclear magnetic resonance
TEM	Transmission electron microscopy
TFE	Trifluoroethanol

ThT	Thioflavin T
TI	Thermodynamic integration
WHAM	Weighted histogram analysis method

Symbols

a	Area per lipid
α	Soft-core parameter or fraction of lipids binding a counter ion
b	Boltzmann factor
c	Concentration
$C_{ij}^{(12)}$	$C^{(12)}$ coefficient scaling the repulsive term of the Lennard-Jones potential between particles i and j
$C_{ij}^{(6)}$	$C^{(6)}$ coefficient scaling the attractive term of the Lennard-Jones potential between particles i and j
δ	Dirac delta function
d	Bond length or distance
e	Elementary charge
ε_0	Vacuum permittivity
ε_r	Relative permittivity
$\mathbf{F}$	Force vector
G	Gibbs free energy
H	Hamiltonian function
h	Planck constant
k_B	Boltzmann constant
K_int	Intrinsic binding constant
λ	Coupling parameter (TI) or reaction coordinate (umbrella sampling)
m	Mass
N	Number
ν	Resonance frequency
P	Probability
p	Probability density or power of the soft-core potential
Φ	Proper dihedral angle
Ψ_0	Surface potential
Q	Configurational integral
q	Electric charge or generalized coordinate
$\mathbf{r}$	Position
t	Time

ρ	Density
r_{ij}	Distance between the particle i and j
S	Entropy
σ	Radius of interaction
S_z	z-component of the lipid order parameter
T	Temperature
Δt	Discrete time interval
θ	Bond angle
U	Potential energy
V	Potential or volume
$\mathscr{W}$	Bias potential
$\mathscr{W}$	Potential of mean force
Z	Partition function
z	Charge number or coordinate
ζ	Improper dihedral angle

Appendix

A.1 Amyloid β: Time evolution of secondary structure at air-water-interface

On the following pages the time evolutions of the secondary structures of the peptides Aβ_{40} and Aβ_{42} under different conditions as discussed in chaper 3 are shown.

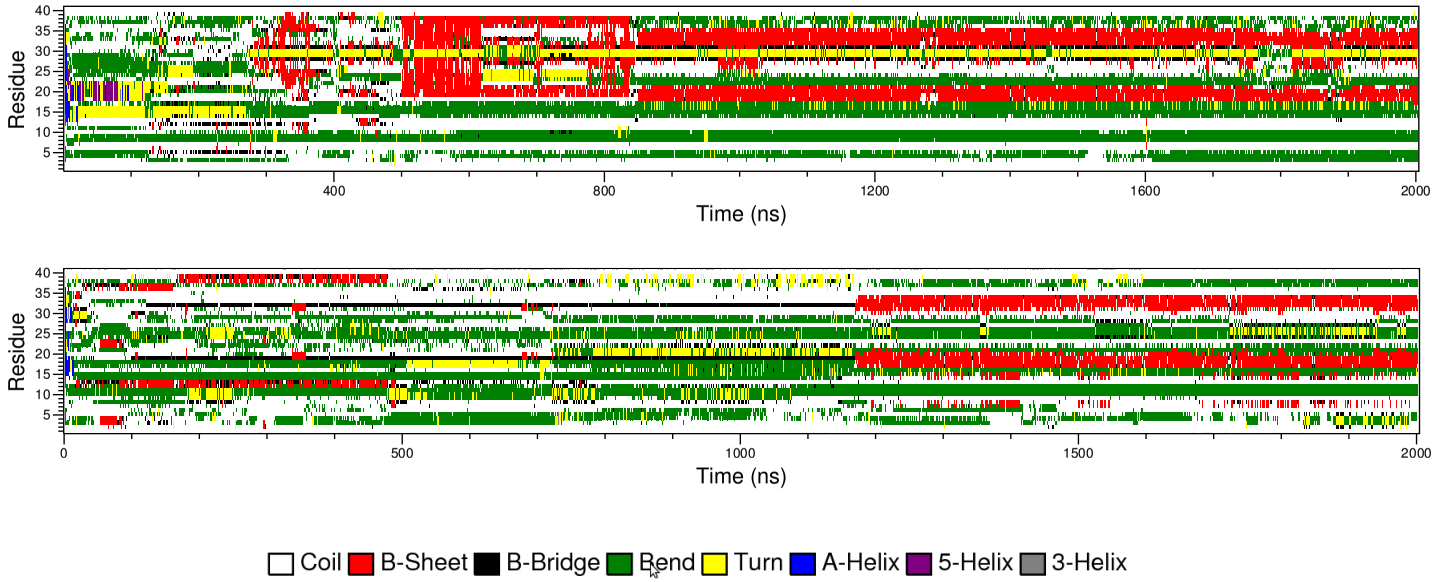

Figure A.1: Time evolution of secondary structure for individual residues of Aβ_{40} at slightly acidic pH in bulk solution (*top*) and at air-water-interface (*bottom*).

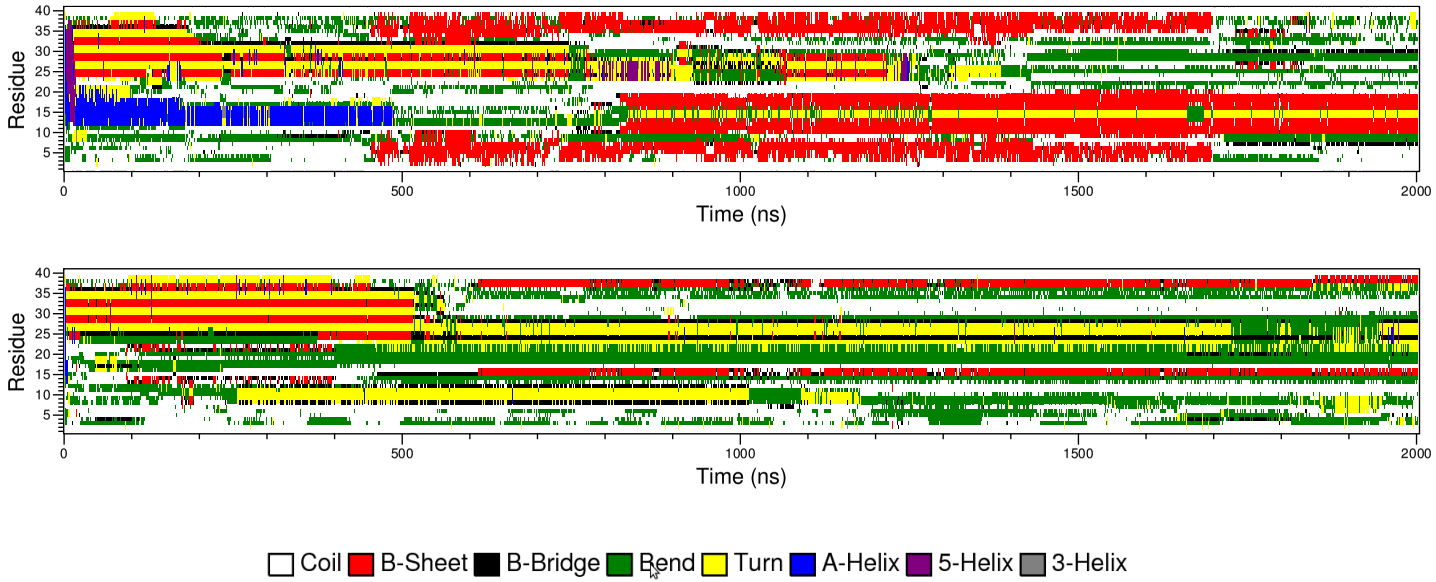

Figure A.2: Time evolution of secondary structure for individual residues of Aβ_{40} at neutral pH in bulk solution (*top*) and at air-water-interface (*bottom*).

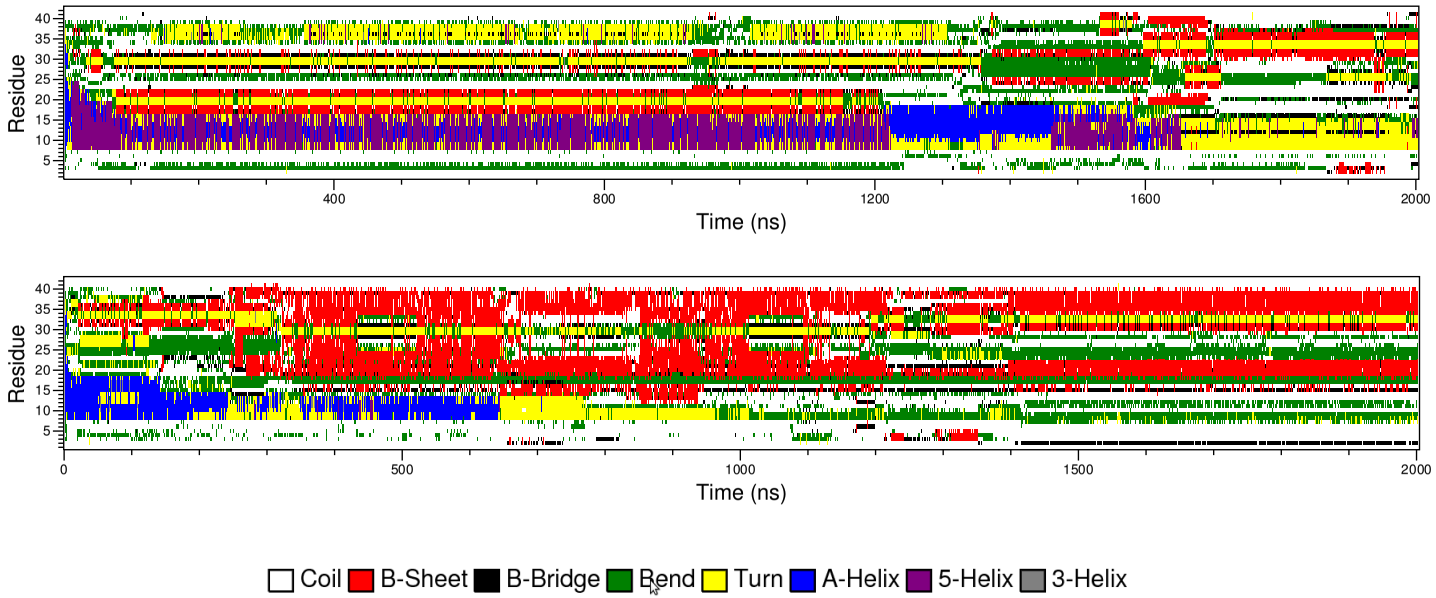

Figure A.3: Time evolution of secondary structure for individual residues of Aβ_{42} at slightly acidic pH in bulk solution (*top*) and at air-water-interface (*bottom*).

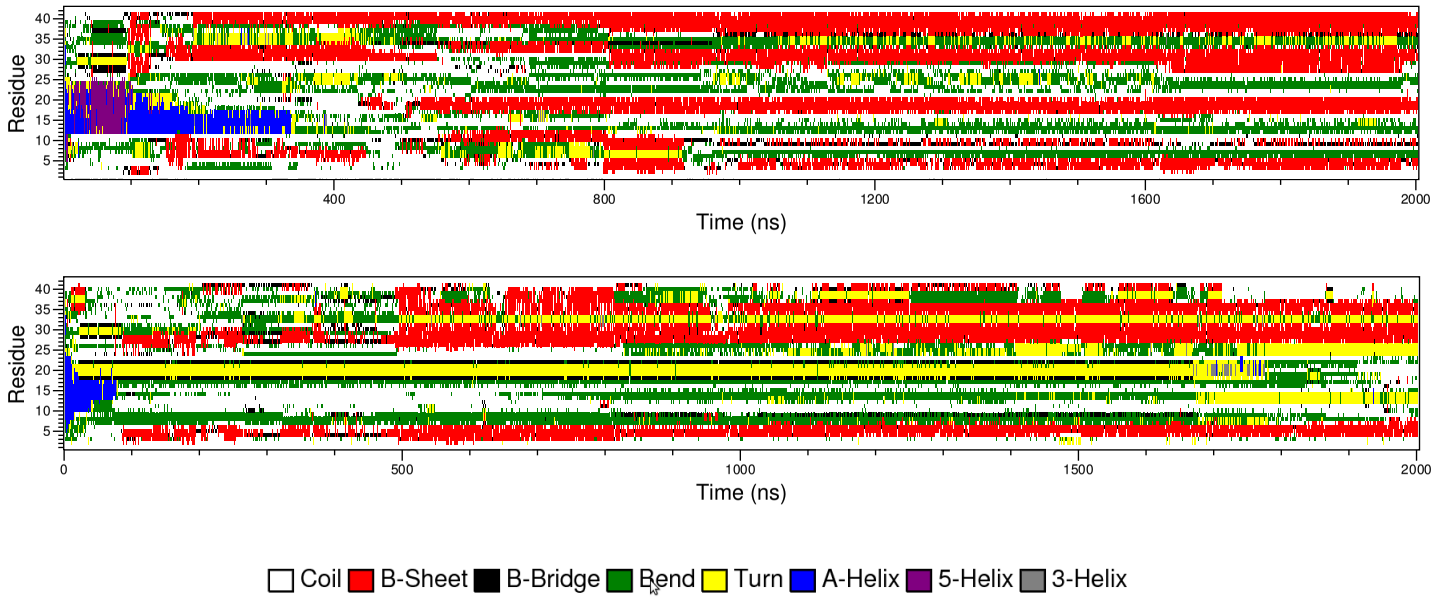

Figure A.4: Time evolution of secondary structure for individual residues of Aβ_{42} at neutral pH in bulk solution (*top*) and at air-water-interface (*bottom*).

A.2 Amyloid β: Pore densities in phospholipid bilayers

In this section equation 4.5 and 4.6 employed in section 4.2.4 to determine the density of membrane pores in case of pure and peptide attached lipid bilayers are derived. To estimate pore densities, first a peptide-free lipid bilayer shall be considered. The distance of the phosphate group of a given lipid from the center of the bilayer in z-direction shall be denoted as z. If z is fixed below a critical value z_p using an umbrella potential in a MD simulation, a pore forms spontaneously. It is intuitive to denote a lipid with $z < z_\mathrm{p}$ as to reside in the "center" of a pore. The probability that a given lipid resides in the center of a pore, P_p, is given by

$$P_\mathrm{p} = \exp\left(-\beta \cdot G_\mathrm{p}\right). \tag{A.1}$$

Here, $\beta = 1/k_\mathrm{B}T$ where k_B denotes Boltzmann's constant and T the absolute temperature. The free energy G_p is

$$G_\mathrm{p} = -k_\mathrm{B}T \cdot \log\left(Z_\mathrm{p}/Z\right) \tag{A.2}$$

where

$$Z = \int_0^{z_\mathrm{c}} b(z)\mathrm{d}z \tag{A.3}$$

is the full partition function for a bilayer-inserted lipid and z_c denotes the position above which the lipid is desorbed from the bilayer. The symbol Z_p denotes the partition function for the state "lipid resides in pore center" which is given by

$$Z_\mathrm{p} = \int_0^{z_\mathrm{p}} b(z)\mathrm{d}z \tag{A.4}$$

with the Boltzmann factor

$$b(z) = \exp\left(-\beta \cdot G(z)\right). \tag{A.5}$$

Here, $G(z)$ is the potential of mean force (PMF) along z as obtained from the umbrella sampling simulations of the peptide-free system. Now a macroscopic bilayer patch at macroscopic time scales shall be considered. If N denotes the number of lipids of one leaflet, $\langle N_\mathrm{p}\rangle$ the number of pores averaged over time, N_l the number of lipids in the center of a given pore coming from one leaflet, and $\langle N_\mathrm{l}\rangle$ the average number of lipids in the center of pores averaged over time, the equation

$$\langle N_\mathrm{l}\rangle = \langle N_\mathrm{p}\rangle \cdot N_\mathrm{l} = P_\mathrm{p} \cdot N$$

holds. Here, N_l may be obtained from a MD simulation of a bilayer exhibiting a pore by determining the corresponding number of phosphate groups with dis-

tances 0 to z_p from the center of the bilayer. If A denotes the area of the (now macroscopic) patch, $a = A/N$ the area per lipid, and

$$\rho_p = \frac{\langle N_p \rangle}{A}$$

the number of pores per area, this leads to

$$\rho_p = \frac{\exp\left(-\beta \cdot G_p\right)}{N_l \cdot a}. \tag{A.6}$$

If, in contrast, a peptide is present, we assume that (i) the probability of a lipid residing in the center of a pore is equal for all lipids in contact with the peptide and that (ii) pores always involve lipids in contact with peptides. Admittedly, assumption (i) is a rather crude approximation due to the inhomogeneity of the peptide. Accordingly, in our case, pulling different lipids in contact with the peptide induced pore formation in one out of three cases only as described in section 4.2.1. This effect was taken into account as described in the result section 4.2.4. Assumption (ii) might lead to a lower or upper bound of the corresponding pore density depending on the free energies of pores in absence and presence of the peptide. The probability that a given lipid in contact with the peptide resides in the center of a pore, $P_{p,c}$, is given by equation (A.1) with G_p in equation (A.1) and (A.2) replaced by $G_{p,c}$ and $G(z)$ in equation (A.5) by $G_{pep}(z)$, where $G_{pep}(z)$ denotes the PMF obtained from the umbrella sampling simulations in the presence of the peptide. If $\langle N_{l,c} \rangle$ denotes the number of lipids in contact with a peptide and residing in the center of a pore averaged over time, N_c the number of lipids in contact with a peptide, and $N_{l,c}$ the number of lipids in contact with a peptide and residing in the center of a single pore, the equation

$$\langle N_{l,c} \rangle = \langle N_p \rangle \cdot N_{l,c} = \exp\left(-\beta \cdot G_{p,c}\right) \cdot N_c$$

holds. If N_{pep} is the number of peptides, $n_c = N_c/N_{pep}$ the number of lipids in contact with a single peptide, and $n_{pep} = N_{pep}/N$ the molar ratio of peptides and lipids, the pore density is

$$\rho_p = \exp\left(-\beta \cdot G_{p,c}\right) \cdot n_c \cdot \frac{n_{pep}}{a \cdot N_{l,c}}.$$

In the presence of a peptide, two types of pores will be present: c-type pores denoting pores involving lipids in contact with a peptide, and n-type pores *not* involving lipids in contact with a peptide. If the average number of c-type pores is $\langle N_{p,c} \rangle$, the average number of n-type pores $\langle N_{p,n} \rangle$, and the total number of

pores $\langle N_\mathrm{p} \rangle$, then

$$\langle N_\mathrm{p} \rangle = \langle N_\mathrm{p,c} \rangle + \langle N_\mathrm{p,n} \rangle.$$

The number of lipids in the center of a c-type pore shall be called $N_\mathrm{l,c}$, and the number of lipids in the center of a n-type pore as $N_\mathrm{l,n}$. Then the number of c-type pores is given by

$$\langle N_\mathrm{p,c} \rangle = \frac{N_\mathrm{c}}{N_\mathrm{l,c}} \cdot \exp(-\beta \cdot G_\mathrm{p,c})$$

and the number of n-type pores by

$$\langle N_\mathrm{p,n} \rangle = \frac{N - N_\mathrm{c}}{N_\mathrm{l,n}} \cdot \exp(-\beta \cdot G_\mathrm{p,n}).$$

Here,

$$G_{\mathrm{p},i} = -k_\mathrm{B} T \cdot \log\left(\frac{Z_{\mathrm{p},i}}{Z_i}\right) \qquad i = \mathrm{c,n}$$

with the partition function for the pore state

$$Z_{\mathrm{p},i} = \int_0^{z_\mathrm{p}} b_i(z)\mathrm{d}z \qquad i = \mathrm{c,n}$$

and the full partition function for the membrane-inserted lipid

$$Z_{\mathrm{p},i} = \int_0^{z_\mathrm{c}} b_i(z)\mathrm{d}z \qquad i = \mathrm{c,n}.$$

Here, as before, z_c denotes the position from which the lipid is desorbed from the bilayer and $b_i(z)$ the Boltzmann factor

$$b_i(z) = \exp\left(-\beta \cdot G_i(z)\right) \qquad i = \mathrm{c,n},$$

with $G_\mathrm{n}(z)$ denoting the PMF for the peptide-free and $G_\mathrm{c}(z)$ the PMF for the bilayer with peptide. With

$$P_i \equiv \exp\left(-\beta \cdot G_{\mathrm{p},i}\right) \qquad i = \mathrm{c,n}$$

and $n_\mathrm{c} n_\mathrm{pep} = N_\mathrm{c}/N$, the number of pores per area, ρ_P, is given by

$$\rho_\mathrm{P} = \frac{\langle N_\mathrm{p} \rangle}{A} = \frac{\langle N_\mathrm{p} \rangle}{Na} = \frac{P_\mathrm{c} \cdot n_\mathrm{c} n_\mathrm{pep}}{N_\mathrm{l,c} a} + \frac{P_\mathrm{n}\left(1 - n_\mathrm{c} n_\mathrm{pep}\right)}{N_\mathrm{l,n} a}. \tag{A.7}$$

A.3 NK-2: Time evolution of secondary structure at phospholipid bilayers

Here, the time evolution of the peptide NK-2 attached to a zwitterionic DOPC and an anionic DOPG bilayer as discussed in section 5.2.1 are shown.

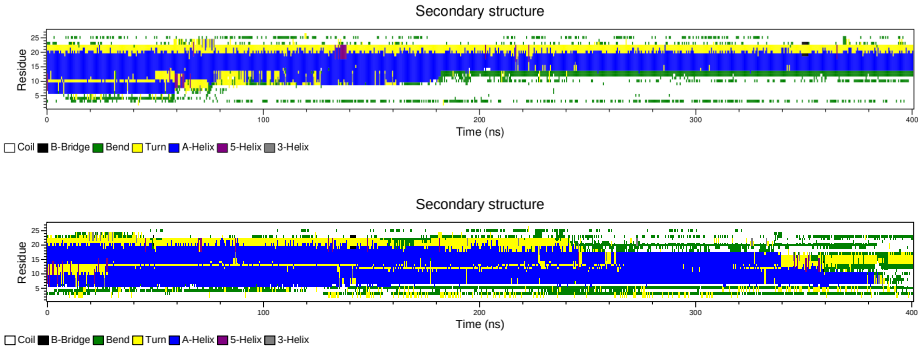

Figure A.5: Time evolution of secondary structure of the NK-2 peptide attached to DOPC (*top*) and a DOPG (*bottom*) bilayer.

Bibliography

[1] W. Stillwell. Chapter 1 - introduction to biological membranes. In *An introduction to biological membranes*, pages 1–12. 2013.

[2] F. Bordi and C. Cametti. Biomembranes. In *Encyclopedia of condensed matter physics*, pages 116–122. 2005.

[3] S. J. Singer and G. L. Nicolson. The fluid mosaic model of the structure of cell membranes. *Science*, 175(4023):720–731, 1972.

[4] K. Simons and E. Ikonen. Functional rafts in cell membranes. *Nature*, 387(6633):569–572, 1997.

[5] W. Stillwell. Chapter 8 - from lipid bilayers to lipid rafts. In *An introduction to biological membranes*, pages 117–129. 2013.

[6] R. A. Kyle. Amyloidosis: a convoluted story. *Brit. J. Haematol.*, 114(3):529–538, 2001.

[7] O. S. Makin and L. C. Serpell. Structures for amyloid fibrils. *FEBS J.*, 272(23):5950–5961, 2005.

[8] L. C. Serpell, M. Sunde, M. D. Benson, G. A Tennent, M. B Pepys, and P. E Fraser. The protofilament substructure of amyloid fibrils. *J. Mol. Biol.*, 300(5):1033–1039, 2000.

[9] M. Sunde and C. Blake. The structure of amyloid fibrils by electron microscopy and x-ray diffraction. In *Advances in protein chemistry*, volume 50, pages 123–159. 1997.

[10] J. S. Pedersen, D. Dikov, J. L. Flink, H. A. Hjuler, G. Christiansen, and D. E. Otzen. The changing face of glucagon fibrillation: structural polymorphism and conformational imprinting. *J. Mol. Biol.*, 355(3):501–523, 2006.

[11] M. Saiki, S. Honda, K. Kawasaki, D. Zhou, A. Kaito, T. Konakahara, and H. Morii. Higher-order molecular packing in amyloid-like fibrils constructed with linear arrangements of hydrophobic and hydrogen-bonding side-chains. *J. Mol. Biol.*, 348(4):983–998, 2005.

[12] H. H. Bauer, U. Aebi, M. Häner, R. Hermann, M. Müller, T. Arvinte, and H. P. Merkle. Architecture and polymorphism of fibrillar supramolecular assemblies produced by in vitro aggregation of human Calcitonin. *J. Struct. Biol.*, 115(1):1–15, 1995.

[13] M. Biancalana and S. Koide. Molecular mechanism of Thioflavin-T binding to amyloid fibrils. *Biochim. Biophys. Acta*, 1804(7):1405–1412, 2010.

[14] R. Nelson and D. Eisenberg. Recent atomic models of amyloid fibril structure. *Curr. Opin. Struct. Biol.*, 16(2):260–265, 2006.

[15] M. Fändrich and C. M. Dobson. The behaviour of polyamino acids reveals an inverse side chain effect in amyloid structure formation. *EMBO J.*, 21(21):5682–5690, 2002.

[16] M. T. Krejchi, S. J. Cooper, Y. Deguchi, E. D. T. Atkins, M. J. Fournier, T. L. Mason, and D. A. Tirrell. Crystal structures of chain-folded antiparallel β-sheet assemblies from sequence-designed periodic polypeptides. *Macromol.*, 30(17):5012–5024, 1997.

[17] Robert Tycko. Solid state NMR studies of amyloid fibril structure. *Ann. Rev. Phys. Chem.*, 62:279–299, 2011.

[18] H. Hiramatsu and T. Kitagawa. FT-IR approaches on amyloid fibril structure. *Biochim. Biophys. Acta*, 1753(1):100–107, 2005.

[19] M. R. Nilsson. Techniques to study amyloid fibril formation in vitro. *Methods*, 34(1):151–160, 2004.

[20] S. V. Litvinovich, S. A. Brew, S. Aota, S. K. Akiyama, C. Haudenschild, and K. C. Ingham. Formation of amyloid-like fibrils by self-association of a partially unfolded fibronectin type III module. *J. Mol. Biol.*, 280(2):245–258, 1998.

[21] M. Stefani and C. M. Dobson. Protein aggregation and aggregate toxicity: new insights into protein folding, misfolding diseases and biological evolution. *J. Mol. Med.*, 81(11):678–699, 2003.

[22] V. N. Uversky and A. L. Fink. Conformational constraints for amyloid fibrillation: the importance of being unfolded. *Biochim. Biophys. Acta*, 1698(2):131–153, 2004.

[23] F. Chiti and C. M. Dobson. Protein misfolding, functional amyloid, and human disease. In *Ann. Rev. Biochem.*, volume 75, pages 333–366. 2006.

[24] M. Stefani. Structural features and cytotoxicity of amyloid oligomers: Implications in Alzheimer's disease and other diseases with amyloid deposits. *Prog. Neurobiol.*, 99(3):226–245, 2012.

[25] C. M. Dobson and M. Karplus. The fundamentals of protein folding: bringing together theory and experiment. *Curr. Opin. Struct. Biol.*, 9(1):92–101, 1999.

[26] F. Chiti, M. Stefani, N. Taddei, G. Ramponi, and C. M. Dobson. Rationalization of the effects of mutations on peptide and protein aggregation rates. *Nature*, 424(6950):805–808, 2003.

[27] T. R. Jahn and S. E. Radford. The Yin and Yang of protein folding. *FEBS J.*, 272(23):5962–5970, 2005.

[28] R. J. Ellis. Macromolecular crowding: obvious but underappreciated. *Trends Biochem. Sci.*, 26(10):597–604, 2001.

[29] F. U. Hartl and M. Hayer-Hartl. Molecular chaperones in the cytosol: from nascent chain to folded protein. *Science*, 295(5561):1852–1858, 2002.

[30] A. Sethuraman and G. Belfort. Protein structural perturbation and aggregation on homogeneous surfaces. *Biophys. J.*, 88(2):1322–1333, 2005.

[31] M. Zhu, P. O. Souillac, C. Ionescu-Zanetti, S. A. Carter, and A. L. Fink. Surface-catalyzed amyloid fibril formation. *J. Biol. Chem.*, 277(52):50914–50922, 2002.

[32] M. Bokvist, F. Lindström, A. Watts, and G. Gröbner. Two types of Alzheimer's β-amyloid (1-40) peptide membrane interactions: aggregation preventing transmembrane anchoring versus accelerated surface fibril formation. *J. Mol. Biol.*, 335(4):1039–1049, 2004.

[33] P. B. Stathopulos, G. A. Scholz, Y.-M. Hwang, J. A.O. Rumfeldt, J. R. Lepock, and E. M. Meiering. Sonication of proteins causes formation of aggregates that resemble amyloid. *Prot. Sci.*, 13(11):3017–3027, 2004.

[34] K. S. Satheeshkumar and R. Jayakumar. Sonication induced sheet formation at the air–water interface. *Chem. Comm.*, (19):2244–2245, 2002.

[35] H. Naiki, N. Hashimoto, S. Suzuki, H. Kimura, K. Nakakuki, and F. Gejyo. Establishment of a kinetic model of dialysis-related amyloid fibril extension in vitro. *Amyl.-Int. J. Exp. Clin. Inv.*, 4(4):223–232, 1997.

[36] T. R. Serio, A. G. Cashikar, A. S. Kowal, G. J. Sawicki, J. J. Moslehi, L. Serpell, M. F. Arnsdorf, and S. L. Lindquist. Nucleated conformational conversion and the replication of conformational information by a prion determinant. *Science*, 289(5483):1317–1321, 2000.

[37] G. Bitan, A. Lomakin, and D. B. Teplow. Amyloid β-protein oligomerization - prenucleation interactions revealed by photo-induced cross-linking of unmodified proteins. *J. Biol. Chem.*, 276(37):35176–35184, 2001.

[38] G. Bitan, M. D. Kirkitadze, A. Lomakin, S. S. Vollers, G. B. Benedek, and D. B. Teplow. Amyloid beta-protein (A beta) assembly: A beta 40 and A beta 42 oligomerize through distinct pathways. *Proc. Nat. Acad. Sci. USA*, 100(1):330–335, 2003.

[39] J. D. Harper, S. S. Wong, C. M. Lieber, and P. T. Lansbury Jr. Observation of metastable Aβ amyloid protofibrils by atomic force microscopy. *Chem. Biol.*, 4(2):119–125, 1997.

[40] D. M. Walsh, A. Lomakin, G. B. Benedek, M. M. Condron, and D. B. Teplow. Amyloid beta-protein fibrillogenesis - Detection of a protofibrillar intermediate. *J. Biol. Chem.*, 272(35):22364–22372, 1997.

[41] J. D. Harper, C. M. Lieber, and P. T. Lansbury. Atomic force microscopic imaging of seeded fibril formation and fibril branching by the Alzheimer's disease amyloid-beta protein. *Chem. Biol.*, 4(12):951–959, 1997.

[42] T. R. Serio, A. G. Cashikar, A. S. Kowal, G. J. Sawicki, J. J. Moslehi, L. Serpell, M. F. Arnsdorf, and S. L. Lindquist. Nucleated conformational conversion and the replication of conformational information by a prion determinant. *Science*, 289(5483):1317–1321, 2000.

[43] M. Bouchard, J. Zurdo, E. J. Nettleton, C. M. Dobson, and C. V. Robinson. Formation of insulin amyloid fibrils followed by FTIR simultaneously with CD and electron microscopy. *Prot. Sci.*, 9(10):1960–1967, 2000.

[44] M. K. M. Chow, A. M. Ellisdon, L. D. Cabrita, and S. P. Bottomley. Polyglutamine expansion in Ataxin-3 does not affect protein stability – implications for misfolding and disease. *J. Biol. Chem.*, 279(46):47643–47651, 2004.

[45] D. M. Walsh, I. Klyubin, J. V. Fadeeva, W. K. Cullen, R. Anwyl, M. S. Wolfe, M. J. Rowan, and D. J. Selkoe. Naturally secreted oligomers of amyloid beta protein potently inhibit hippocampal long-term potentiation in vivo. *Nature*, 416(6880):535–539, 2002.

[46] J. P. Cleary, D. M. Walsh, J. J. Hofmeister, G. M. Shankar, M. A. Kuskowski, D. J. Selkoe, and K. H. Ashe. Natural oligomers of the amyloid-protein specifically disrupt cognitive function. *Nature Neurosci.*, 8(1):79–84, 2005.

[47] K. A. Conway, S. J. Lee, J. C. Rochet, T. T. Ding, R. E. Williamson, and P. T. Lansbury. Acceleration of oligomerization, not fibrillization, is a shared property of both alpha-synuclein mutations linked to early-onset Parkinson's disease: implications for pathogenesis and therapy. *Proc. Nat. Acad. Sci. USA*, 97(2):571–576, 2000.

[48] G. Anderluh, I. Gutierrez-Aguirre, S. Rabzelj, S. Ceru, N. Kopitar-Jerala, P. Macek, V. Turk, and E. Zerovnik. Interaction of human stefin B in the prefibrillar oligomeric form with membranes - correlation with cellular toxicity. *FEBS J.*, 272(12):3042–3051, 2005.

[49] I. Sirangelo, C. Malmo, C. Iannuzzi, A. Mezzogiorno, M. R. Bianco, M. Papa, and G. Irace. Fibrillogenesis and cytotoxic activity of the amyloid-forming apomyoglobin mutant W7FW14F. *J. Biol. Chem.*, 279(13):13183–13189, 2004.

[50] Alzheimer's disease international (ADI) *http//:www.alz.co.uk* as at 09-2013.

[51] A. Alzheimer. Über eine eigenartige Erkrankung der Hirnrinde. *Allg. Z. Psychiatrie Psychisch-Gerichtliche Med.*, 13:146–148, 1907.

[52] D. H. Small and R. Cappai. Alois Alzheimer and Alzheimer's disease: a centennial perspective. *J. Neurochem.*, 99:708–710, 2006.

[53] G. G. Glenner and C. W. Wong. Alzheimer's disease: initial report of the purification and characterization of a novel cerebrovascular amyloid protein. *Biochem. Biophys. Res. Comm.*, 120:885–890, 1984.

[54] I. Grundke-Iqbal. Abnormal phosphorylation of the microtubule-associated protein tau (τ) in Alzheimer cytoskeletal pathology. *Proc. Nat. Acad. Sci.*, 83:4913–4917, 1986.

[55] M. Goedert. Cloning and sequencing of the cDNA encoding a core protein of the paired helical filament of Alzheimer disease: identification as the microtubule-associated protein tau. *Proc. Nat. Acad. Sci.*, 85:4051–4055, 1988.

[56] Y. Ihara, N. Nukina, R. Miura, and M. Ogawara. Phosphorylated tau protein is integrated into paired helical filaments in Alzheimers-disease. *J. Biochem.*, 99:1807–1810, 1986.

[57] Avila, J. and Lucas, J. J. and Pèrez, M. and Hernández, F. Role of tau protein in both physiological and pathological conditions. *Physiol. Rev.*, 84:361–384, 2004.

[58] M. P. Mattson. Pathways towards and away from Alzheimer's disease. *Nature*, 430:631–639, 2004.

[59] U. C. Müller and H. Zheng. Physiological functions of APP family proteins. *Cold Spring Harb. Perspect. Med.*, 2, 2012.

[60] C. Haass, C. Kaether, G. Thinakaran, and S. Sisodia. Trafficking and proteolytic processing of APP. *Cold Spring Harb. Perspect. Med.*, 2, 2012.

[61] J. Hardy and D. J. Selkoe. The amyloid hypothesis of Alzheimer's disease: progress and problems on the road to therapeutics. *Science*, 297(5580):353–356, 2002.

[62] R. Kayed, E. Head, J. L. Thompson, T. M. McIntire, S. C. Milton, C. W. Cotman, and C. G. Glabe. Common structure of soluble amyloid oligomers implies common mechanism of pathogenesis. *Science*, 300:486–489, 2003.

[63] O. M. A. El-Agnaf, D. S. Mahil, B. P. Patel, and B. M. Austen. Oligomerization and toxicity of β-amyloid-42 implicated in Alzheimer's disease. *Biochem. Biophys. Res. Comm.*, 273:1003–1007, 2000.

[64] M. P. Lambert, A. K. Barlow, B. A. Chromy, C. Edwards, R. Freed, M. Liosatos, T. E. Morgan, I. Rozovsky, B. Trommer, K. L. Viola, P. Wals, C. Zhang, C. E. Finch, G. A. Krafft, and W. L. Klein. Diffusible, nonfibrillar ligands derived from A beta 1-42 are potent central nervous system neurotoxins. *Proc. Natl. Acad. Sci. USA*, 95:6448–6453, 1998.

[65] M.P. Mattson. Untangling the pathophysiochemistry of beta-amyloid. *Nat. Struct. Biol.*, 2(11):926–928, 1995.

[66] M. D. Kirkitadze, G. Bitan, and D. B. Teplow. Paradigm shifts in Alzheimer's disease and other neurodegenerative disorders: the emerging role of oligomeric assemblies. *J. Neurosci. Res.*, 69:567–577, 2002.

[67] S. C. Bondy, S. X. Guo-Ross, and A. T. Truong. Promotion of transition metal-induced reactive oxygen species formation by β-amyloid. *Brain Res.*, 799:91–96, 1998.

[68] X. Huang, C. S. Atwood, M. A. Hartshorn, G. Multhaup, L. E. Goldstein, R. C. Scarpa, M. P. Cuajungco, D. N. Gray, J. Lim, R. D. Moir, R. E. Tanzi, and A. I. Bush. The Aβ peptide of Alzheimer's disease directly produces hydrogen peroxide through metal ion reduction. *Biochem.*, 38:7609–7616, 1999.

[69] D. A. Butterfield and C. M. Lauderback. Lipid peroxidation and protein oxidation in Alzheimer's disease brain: potential causes and consequences involving amyloid beta-peptide-associated free radical oxidative stress. *Free Radical Biol. & Med.*, 32:1050–1060, 2002.

[70] M. E. King, H.-M. Kan, P. W. Baas, A. Erisir, C. G. Glabe, and G. S. Bloom. Tau-dependent microtubule disassembly initiated by prefibrillar β-amyloid. *J. Cell Biol.*, 175:541–546, 2006.

[71] L. Mucke, E. Masliah, G. Q. Yu, M. Mallory, and E. M. Rockenstein. High-level neuronal expression of A beta(1-42) in wild-type human amyloid protein precursor transgenic mice: synaptotoxicity without plaque formation. *J. Neurosci.*, 20:4050–4058, 2000.

[72] S. Oddo, A. Caccamo, J. D. Shepherd, M. P. Murphy, T. E. Golde, R. Kayed, R. Metherate, M. P. Mattson, Y. Akbari, and F. M. LaFerla. Triple-transgenic model of Alzheimer's disease with plaques and tangles. *Neuron*, 39:409–421, 2003.

[73] I. Dewachter and F. van Leuven. Secretases as targets for the treatment of Alzheimer's disease: the prospects. *Lancet Neurol.*, 1:409–416, 2002.

[74] L. A. Kotilinek, B. Bacskai, M. Westerman, T. Kawarabayashi, and L. Younkin. Reversible memory loss in a mouse transgenic model of Alzheimer's disease. *J. Neurosci.*, 22:6331–6335, 2002.

[75] D. Morgan, D. M. Diamond, P. E. Gottschall, K. E. Ugen, C. Dickey, J. Hardy, K. Duff, P. Jantzen, G. DiCarlo, D. Wilcock, K. Connor, J. Hatcher, C. Hope, M. Gordon, and G. W. Arendash. Aβ peptide vaccination prevents memory loss in an animal model of Alzheimer's disease. *Nature*, 408:982–985, 2000.

[76] L. O. Tjernberg, C. Lilliehöök, D. J. E. Callaway, J. Näslund, S. Hahne, J. Thyberg, L. Terenius, and C. Nordstedt. Controlling amyloid β-peptide fibril formation with protease-stable ligands. *J. Biol. Chem.*, 272(19):12601–12605, 1997.

[77] E. Gazit. A possible role for π-stacking in the self-assembly of amyloid fibrils. *FASEB J.*, 16(1):77–83, 2002.

[78] L. O. Tjernberg, J. Naslund, F. Lindqvist, J. Johansson, A. R. Karlstrom, J. Thyberg, L. Terenius, and C. Nordstedt. Arrest of beta-amyloid fibril formation by a pentapeptide ligand. *J. Biol. Chem.*, 271(15):8545–8548, 1996.

[79] M. A. Findeis, G. M. Musso, C. C. Arico-Muendel, H. W. Benjamin, A. M. Hundal, J. Lee, J. Chin, M. Kelley, J. Wakefield, N. J. Hayward, and S. M. Molineaux. Modified-peptide inhibitors of amyloid β-peptide polymerization. *Biochem.*, 38(21):6791–6800, 1999.

[80] J. J. Balbach, Y. Ishii, O. N. Antzutkin, R. D. Leapman, N. W. Rizzo, F. Dyda, J. Reed, and R. Tycko. Amyloid fibril formation by Aβ16-22, a seven-residue fragment of the Alzheimer's β-amyloid peptide, and structural characterization by solid state NMR. *Biochem.*, 39(45):13748–13759, 2000.

[81] S. Kim, T. J. Jeon, A. Oberai, D. Yang, J. J. Schmidt, and J. U. Bowie. Transmembrane glycine zippers: Physiological and pathological roles in membrane proteins. *Proc. Nat. Acad. Sci. USA*, 102(40):14278–14283, 2005.

[82] K.T. O'Neil and W.F. DeGrado. A thermodynamic scale for the helix-forming tendencies of the commonly occurring amino acids. *Science*, 250(4981):646–651, 1990.

[83] V. Fonte, V. Dostal, C. M. Roberts, P. Gonzales, P. Lacor, J. Magrane, N. Dingwell, E. Y. Fan, M. A. Silverman, G. H. Stein, and C. D. Link. A glycine zipper motif mediates the formation of toxic beta-amyloid oligomers in vitro and in vivo. *Mol. Neurodeg.*, 6(1):1–17, 2011.

[84] L. W. Hung, G. D. Ciccotosto, E. Giannakis, D. J. Tew, K. Perez, C. L. Masters, R. Cappai, J. D. Wade, and K. J. Barnham. Amyloid-β peptide (Aβ) neurotoxicity is modulated by the rate of peptide aggregation: Aβ dimers and trimers correlate with neurotoxicity. *J. Neurosci.*, 28(46):11950–11958, 2008.

[85] O. O. Olubiyi and B. Strodel. Structures of the amyloid beta-peptides A beta(1-40) and A beta(1-42) as influenced by pH and a D-peptide. *J. Phys. Chem. B*, 116(10):3280–3291, 2012.

[86] C. M. Yates, J. Butterworth, M. C. Tennant, and A. Gordon. Enzyme activities in relation to pH and lactate in postmortem brain in Alzheimer-type and other dementias. *J. Neurochem.*, 55(5):1624–1630, 1990.

[87] N. G. Sgourakis, Y. Yan, S. A. McCallum, C. Wang, and A. E. Garcia. The Alzheimer's peptides Aβ40 and 42 adopt distinct conformations in water: a combined MD/NMR study. *J. Mol. Biol.*, 368(5):1448–1457, 2007.

[88] Y. Yan and C. Wang. Aβ42 is more rigid than Aβ40 at the C terminus: Implications for Aβ aggregation and toxicity. *J. Mol. Biol.*, 364(5):853–862, 2006.

[89] K. H. Lim, H. H. Collver, Y. T. H. Le, P. Nagchowdhuri, and J. M. Kenney. Characterizations of distinct amyloidogenic conformations of the Aβ (1–40) and (1–42) peptides. *Biochem. Biophys. Res. Comm.*, 353(2):443–449, 2007.

[90] S. Zhang, K. Iwata, M.J. Lachenmann, J.W. Peng, S. Li, E.R. Stimson, Y.-a. Lu, A.M. Felix, J.E. Maggio, and J.P. Lee. The Alzheimer's peptide Aβ adopts a collapsed coil structure in water. *J. Struct. Biol.*, 130(2–3):130–141, 2000.

[91] L. Hou, H. Shao, Y. Zhang, H. Li, N. K. Menon, E. B. Neuhaus, J. M. Brewer, I.-J. L. Byeon, D. G. Ray, M. P. Vitek, T. Iwashita, R. A. Makula, A. B. Przybyla, and M. G. Zagorski. Solution NMR studies of the Aβ(1-40) and Aβ(1-42) peptides establish that the Met35 oxidation state affects the mechanism of amyloid formation. *J. Am. Chem. Soc.*, 126(7):1992–2005, 2004.

[92] S. Vivekanandan, J. R. Brender, S. Y. Lee, and A. Ramamoorthy. A partially folded structure of amyloid-beta(1-40) in an aqueous environment. *Biochem. Biophys. Res. Comm.*, 411(2):312–316, 2011.

[93] R. Riek, P. Guntert, H. Dobeli, B. Wipf, and K. Wuthrich. NMR studies in aqueous solution fail to identify significant conformational differences between the monomeric forms of two Alzheimer peptides with widely different plaque-competence, A beta(1-40)(ox) and A beta(1-42)(ox). *Europ. J. Biochem.*, 268(22):5930–5936, 2001.

[94] M. Yang and D. B. Teplow. Amyloid β-protein monomer folding: free energy surfaces reveal alloform specific differences. *J. Mol. Biol.*, 384(2):450–464, 2008.

[95] N. G. Sgourakis, M. Merced-Serrano, C. Boutsidis, P. Drineas, Z. Du, C. Wang, and A. E. Garcia. Atomic-level characterization of the ensemble of the A beta(1-42) monomer in water using unbiased molecular dynamics simulations and spectral algorithms. *J. Mol. Biol.*, 405(2):570–583, 2011.

[96] R. Zhou. Free energy landscape of protein folding in water: Explicit vs. implicit solvent. *Proteins*, 53(2):148–161, 2003.

[97] S. Tomaselli, V. Esposito, P. Vangone, N. A. J. van Nuland, A. M. J. J. Bonvin, R. Guerrini, T. Tancredi, P. A. Temussi, and D. Picone. The α-to-β conformational transition of Alzheimer's Aβ-(1–42) peptide in aqueous media is reversible: a step by step conformational analysis suggests the location of β conformation seeding. *ChemBioChem*, 7(2):257–267, 2006.

[98] M. Coles, W. Bicknell, A. A. Watson, D. P. Fairlie, and D. J. Craik. Solution structure of amyloid beta-peptide(1-40) in a water-micelle environment. Is the membrane-spanning domain where we think it is? *Biochem.*, 37(31):11064–11077, 1998.

[99] M. Kawahara, I. Ohtsuka, S. Yokoyama, M. Kato-Negishi, and Y. Sadakane. Membrane incorporation, channel formation, and disruption of calcium homeostasis by Alzheimer's β-amyloid protein. *Internat. J. Alzh. Dis.*, 2011, 2011.

[100] A. Demuro, I. Parker, and G. E. Stutzmann. Calcium signaling and amyloid toxicity in Alzheimer disease. *J. Biol. Chem.*, 285(17):12463–12468, 2010.

[101] C. Rovira, N. Arbez, and J. Mariani. Aβ(25–35) and Aβ(1–40) act on different calcium channels in CA1 hippocampal neurons. *Biochem. Biophys. Res. Comm.*, 296(5):1317–1321, 2002.

[102] E. Alberdi, M. V. Sánchez-Gómez, F. Cavaliere, A. Pérez-Samartín, J. L. Zugaza, R. Trullas, M. Domercq, and C. Matute. Amyloid β oligomers induce Ca^{2+} dysregulation and neuronal death through activation of ionotropic glutamate receptors. *Cell Calcium*, 47(3):264–272, 2010.

[103] J. H. Weiss, C. J. Pike, and C. W. Cotman. Rapid communication: Ca^{2+} channel blockers attenuate β-amyloid peptide toxicity to cortical neurons in culture. *J. Neurochem.*, 62(1):372–375, 1994.

[104] H. R. Parri and K. T. Dineley. Nicotinic acetylcholine receptor interaction with-amyloid: molecular, cellular, and physiological consequences. *Curr. Alzh. Res.*, 7(1):27–39, 2010.

[105] M. Verdurand, A. Bérod, D. Le Bars, and L. Zimmer. Effects of amyloid-β peptides on the serotoninergic 5-ht1a receptors in the rat hippocampus. *Neurobiol. Aging*, 32(1):103–114, 2011.

[106] S. D. Buckingham, A. K. Jones, L. A. Brown, and D. B. Sattelle. Nicotinic acetylcholine receptor signalling: roles in Alzheimer's disease and amyloid neuroprotection. *Pharmacol. Rev.*, 61(1):39–61, 2009.

[107] D. H. Cribbs, C. J. Pike, S. L. Weinstein, P. Velazquez, and C. W. Cotman. All-D-enantiomers of β-amyloid exhibit similar biological properties to all-L-β-amyloids. *J. Biol. Chem.*, 272(11):7431–7436, 1997.

[108] A. Demuro, E. Mina, R. Kayed, S. C. Milton, I. Parker, and C. G. Glabe. Calcium dysregulation and membrane disruption as a ubiquitous neurotoxic mechanism of soluble amyloid oligomers. *J. Biol. Chem.*, 280(17):17294–17300, 2005.

[109] B. Hille. *Ion channels of excitable membranes*, volume 507. 2001.

[110] Y. Sokolov, J. A. Kozak, R. Kayed, A. Chanturiya, C. Glabe, and J. E. Hall. Soluble amyloid oligomers increase bilayer conductance by altering dielectric structure. *J. Gen. Physiol.*, 128(6):637–647, 2006.

[111] R. Capone, F. G. Quiroz, P. Prangkio, I. Saluja, A. M. Sauer, M. R. Bautista, R. S. Turner, J. Yang, and M. Mayer. Amyloid-β-induced ion flux in artificial lipid bilayers and neuronal cells: resolving a controversy. *Neurotoxic. Res.*, 16(1):1–13, 2009.

[112] A. Quist, I. Doudevski, H. Lin, R. Azimova, D. Ng, B. Frangione, B. Kagan, J. Ghiso, and R. Lal. Amyloid ion channels: a common structural link for protein-misfolding disease. *Proc. Nat. Acad. Sci. USA*, 102(30):10427–10432, 2005.

[113] H. Lin, R. Bhatia, and R. Lal. Amyloid β protein forms ion channels: implications for Alzheimer's disease pathophysiology. *FASEB J.*, 15(13):2433–2444, 2001.

[114] H. Jang, J. Zheng, R. Lal, and R. Nussinov. New structures help the modeling of toxic amyloid ß ion channels. *Trends Biochem. Sci.*, 33(2):91–100, 2008.

[115] N. Arispe, E. Rojas, and H. B. Pollard. Alzheimer disease amyloid beta protein forms calcium channels in bilayer membranes: blockade by tromethamine and aluminum. *Proc. Nat. Acad. Sci. USA*, 90(2):567–571, 1993.

[116] N. Arispe, H. B. Pollard, and E. Rojas. Giant multilevel cation channels formed by Alzheimer disease amyloid β-protein [AβP-(1-40)] in bilayer membranes. *Proc. Nat. Acad. Sci. USA*, 90(22):10573–10577, 1993.

[117] Y. Hirakura, M.-C. Lin, and B. L. Kagan. Alzheimer amyloid Aβ1–42 channels: effects of solvent, pH, and Congo Red. *J. Neurosci. Res.*, 57(4):458–466, 1999.

[118] H. Jang, J. Zheng, and R. Nussinov. Models of β-amyloid ion channels in the membrane suggest that channel formation in the bilayer is a dynamic process. *Biophys. J.*, 93(6):1938–1949, 2007.

[119] H. Jang, F. T. Arce, S. Ramachandran, R. Capone, R. Azimova, B. L. Kagan, R. Nussinov, and R. Lal. Truncated β-amyloid peptide channels provide an alternative mechanism for Alzheimer's disease and Down syndrome. *Proc. Nat. Acad. Sci.*, 107(14):6538–6543, 2010.

[120] B. L. Kagan, R. Azimov, and R. Azimova. Amyloid peptide channels. *J. Membrane Biol.*, 202(1):1–10, 2004.

[121] S. B. Levy. Antibiotic resistance - the problem intensifies. *Adv. Drug Del. Rev.*, 57(10):1446–1450, 2005.

[122] M. Leeb. Antibiotics: a shot in the arm. *Nature*, 431(7011):892–893, 2004.

[123] R. E. W. Hancock and G. Diamond. The role of cationic antimicrobial peptides in innate host defences. *Trends Microbiol.*, 8(9):402–410, 2000.

[124] K. A. Brogden. Antimicrobial peptides: pore formers or metabolic inhibitors in bacteria? *Nat. Rev. Microbiol.*, 3(3):238–250, 2005.

[125] K. L. Brown and R. E. W. Hancock. Cationic host defense (antimicrobial) peptides. *Curr. Opin. Immun.*, 18(1):24–30, 2006.

[126] A. Tossi, L. Sandri, and A. Giangaspero. Amphipathic, alpha-helical antimicrobial peptides. *Biopol.*, 55(1):4–30, 2000.

[127] R. Gennaro and M. Zanetti. Structural features and biological activities of the cathelicidin-derived antimicrobial peptides. *Biopol.*, 55(1):31–49, 2000.

[128] K. A. Brogden, A. J DeLucca, J. Bland, and S. Elliott. Isolation of an ovine pulmonary surfactant-associated anionic peptide bactericidal for Pasteurella haemolytica. *Proc. Nat. Acad. Sci. USA*, 93(1):412–416, 1996.

[129] C. B. Park, H. S. Kim, and S. C. Kim. Mechanism of action of the antimicrobial peptide buforin II: buforin II kills microorganisms by penetrating the cell membrane and inhibiting cellular functions. *Biochem. Biophys. Res. Comm.*, 244(1):253–257, 1998.

[130] H. Brotz, G. Bierbaum, K. Leopold, P. E. Reynolds, and H. G. Sahl. The lantibiotic mersacidin inhibits peptidoglycan synthesis by targeting lipid II. *Amtimicr. Agents Chemoth.*, 42(1):154–160, 1998.

[131] A. Patrzykat, C. L. Friedrich, L. Zhang, V. Mendoza, and R. E. W. Hancock. Sublethal concentrations of pleurocidin-derived antimicrobial peptides inhibit macromolecular synthesis in Escherichia coli. *Antimicr. Agents Chemoth.*, 46(3):605–614, 2002.

[132] D. Andreu and L. Rivas. Animal antimicrobial peptides: an overview. *Biopol.*, 47(6):415–433, 1998.

[133] L. Yang, T. A. Harroun, T. M. Weiss, L. Ding, and H. W. Huang. Barrel-stave model or toroidal model? A case study on melittin pores. *Biophys. J.*, 81(3):1475–1485, 2001.

[134] S. Yamaguchi, D. Huster, A. Waring, R. I. Lehrer, W. Kearney, B. F. Tack, and M. Hong. Orientation and dynamics of an antimicrobial peptide in the

lipid bilayer by solid-state NMR spectroscopy. *Biophys. J.*, 81(4):2203–2214, 2001.

[135] R. E. W. Hancock and D. S. Chapple. Peptide antibiotics. *Antimicr. Agents Chemoth.*, 43(6):1317–1323, 1999.

[136] H. Andersson, H. Gunne, B. Agerberth, A. Boman, T. Bergman, R. Sillard, H. Jornvall, V. Mutt, B. Olsson, H. Wigzell, A. Dagerlind, H. G. Boman, and G. H. Gudmundsson. NK-lysin, a novel effector peptide of cytotoxic T-cells and NK-cells - structure and cDNA cloning of the porcine form, induction by interleukin-2, antibacterial and antitumor-activity. *EMBO J.*, 14(8):1615–1625, 1995.

[137] E. Liepinsh, M. Andersson, G. Otting, and J. M. Ruysschaert. Saposin fold revealed by the NMR structure of NK-lysin. *Nature struct. biol.*, 4(10):793–5, 1997.

[138] M. Andersson, T. Curstedt, H. Jornvall, and J. Johansson. An amphipathic helical motif common to tumourolytic polypeptide NK-lysin and pulmonary surfactant polypeptide SP-B. *FEBS Lett.*, 362(3):328–332, 1995.

[139] E. Liepinsh, M. Andersson, J. M. Ruysschaert, and G. Otting. Saposin fold revealed by the NMR structure of NK-lysin. *Nat. Struct. Biol.*, 4(10):793–795, 1997.

[140] J. Andrä and M. Leippe. Candidacidal activity of shortened synthetic analogs of amoebapores and NK-lysin. *Med. Microbiol. Immun.*, 188(3):117–124, 1999.

[141] D. Andreu, C. Carreno, C. Linde, H. G. Boman, and M. Andersson. Identification of an anti-mycobacterial domain in NK-lysin and granulysin. *Biochem. J.*, 344(3):845–849, 1999.

[142] C. Olak, A. Muenter, J. Andrä, and G. Brezesinski. Interfacial properties and structural analysis of the antimicrobial peptide NK-2. *J. Pept. Sci.*, 14(4):510–517, 2008.

[143] R. Willumeit, M. Kumpugdee, S. S. Funari, K. Lohner, B. Pozo Navas, K. Brandenburg, S. Linser, and J. Andrä. Structural rearrangement of model membranes by the peptide antibiotic NK-2. *Biochim. Biophys. Acta - Biomembranes*, 1669(2):125–134, 2005.

[144] H. Schröder-Borm, R. Willumeit, K. Brandenburg, and J. Andrä. Molecular basis for membrane selectivity of NK-2, a potent peptide antibiotic derived from NK-lysin. *Biochim. Biophys. Acta*, 1612(2):164–171, 2003.

[145] C. I. E. von Deuster and V. Knecht. Competing interactions for antimicrobial selectivity based on charge complementarity. *Biochim. Biophys. Acta – Biomembranes*, 1808(12):2867–2876, 2011.

[146] C. I. E. von Deuster and V. Knecht. Antimicrobial selectivity based on zwitterionic lipids and underlying balance of interactions. *Biochim. Biophys. Acta - Biomembranes*, 1818(9):2192–2201, 2012.

[147] L. Verlet. Computer "experiments" on classical fluids. i. thermodynamical properties of Lennard-Jones molecules. *Phys. Rev.*, 159:98–103, 1967.

[148] R. W. Hockney and J. W. Eastwood. *Computer simulation using particles*. 1981.

[149] W. L. Jorgensen, D. S. Maxwell, and J. Tirado-Rives. Development and testing of the OPLS all-atom force field on conformational energetics and properties of organic liquids. *J. Am. Chem. Soc.*, 118(45):11225–11236, 1996.

[150] A. D. MacKerell, D. Bashford, M. Bellott, R. L. Dunbrack, J. D. Evanseck, M. J. Field, S. Fischer, J. J. Gao, H. Guo, S. Ha, D. Joseph-McCarthy, L. Kuchnir, K. Kuczera, F. T. K. Lau, C. Mattos, S. Michnick, T. Ngo, D. T. Nguyen, B. Prodhom, W. E. Reiher, B. Roux, M. Schlenkrich, J. C. Smith, R. Stote, J. Straub, M. Watanabe, J. Wiórkiewicz-Kuczera, D. Yin, and M. Karplus. All-atom empirical potential for molecular modeling and dynamics studies of proteins. *J. Phys. Chem. B*, 102(18):3586–3616, 1998.

[151] W. D. Cornell, P. Cieplak, C. I. Bayly, I. R. Gould, K. M. Merz, D. M. Ferguson, D. C. Spellmeyer, T. Fox, J. W. Caldwell, and P. A. Kollman. A second generation force field for the simulation of proteins, nucleic acids, and organic molecules. *J. Am. Chem. Soc.*, 117(19):5179–5197, 1995.

[152] W. F. van Gunsteren, S. R. Billeter, A. A. Eising, P. H. Hünenberger, P. Krüger, A. E. Mark, W. R. P. Scott, and I. G. Tironi. *Biomolecular simulation: The GROMOS96 manual and user guide*. 1996.

[153] S. J. Marrink, H. J. Risselada, S. Yefimov, D. P. Tieleman, and A. H. de Vries. The MARTINI force field: coarse grained model for biomolecular simulations. *J. Phys. Chem. B*, 111(27):7812–7824, 2007.

[154] J.-P. Ryckaert, G. Ciccotti, and H. J. C. Berendsen. Numerical integration of the cartesian equations of motion of a system with constraints: molecular dynamics of n-alkanes. *J. Comp. Phys.*, 23(3):327–341, 1977.

[155] A. Baranyai and D. J Evans. New algorithm for constrained molecular-dynamics simulation of liquid benzene and naphthalene. *Mol. Phys.*, 70(1):53–63, 1990.

[156] J. G. Kirkwood. Statistical mechanics of fluid mixtures. *J. Chem. Phys.*, 3(5):300–313, 1935.

[157] G. M. Torrie and J. P. Valleau. Monte Carlo free energy estimates using non-Boltzmann sampling: application to the sub-critical Lennard-Jones fluid. *Chem. Phys. Lett.*, 28(4):578–581, 1974.

[158] S. Kumar, J. M. Rosenberg, D. Bouzida, R. H. Swendsen, and P. A. Kollman. The weighted histogram analysis method for free-energy calculations on biomolecules. I. The method. *J. Comp. Chem.*, 13:1011–1021, 1992.

[159] Bennett, C. H. Efficient estimation of free-energy differences from Monte-Carlo data. *J. Comp. Phys.*, 22(2):245–268, 1976.

[160] A. M. Ferrenberg and R. H. Swendsen. Optimized Monte Carlo data analysis. *Phys. Rev. Lett.*, 63:1195–1198, 1989.

[161] J. S. Hub, B. L. de Groot, and D. van der Spoel. g_wham – A free weighted histogram analysis implementation including robust error and autocorrelation estimates. *J. Chem. Th. Comp.*, 6:3713–3720, 2010.

[162] M. R. Shirts and V. S. Pande. Comparison of efficiency and bias of free energies computed by exponential averaging, the Bennett acceptance ratio, and thermodynamic integration. *J. Chem. Phys*, 122(14), 2005.

[163] T. C. Beutler, A. E. Mark, R. C van Schaik, P. R. Gerber, and W. F. van Gunsteren. Avoiding singularities and numerical instabilities in free-energy calculations based on molecular simulations. *Chem. Phys. Let.*, 222(6):529–539, 1994.

[164] H. J. C. Berendsen, J. P. M. Postma, W. F. van Gunsteren, J. Hermans, and B. Pullman (ed.). *Intermolecular forces*. 1981.

[165] D. van der Spoel, E. Lindahl, B. Hess, G. Groenhof, A. E. Mark, and H. J. C. Berendsen. GROMACS: Fast, flexible, and free. *J. Comp. Chem.*, 26:1701–1718, 2005.

[166] B. Hess, C. Kutzner, D. van der Spoel, and E. Lindahl. GROMACS 4: algorithms for highly efficient, load-balanced, and scalable molecular simulation. *J. Chem. Th. Comp.*, 4:435–447, 2008.

[167] H. J. C. Berendsen, D. van der Spoel, and R. van Drunen. GROMACS - A message-passing parallel molecular-dynamics implementation. *Comp. Phys. Comm.*, 91:43–56, 1995.

[168] W. Kabsch and C. Sander. Dictionary of protein secondary structure - pattern-recognition of hydrogen-bonded and geometrical features. *Biopol.*, 22(12):2577–2637, 1983.

[169] X. Daura, K. Gademann, B. Jaun, D. Seebach, W. F. van Gunsteren, and A. E. Mark. Peptide folding: When simulation meets experiment. *Angew. Chem. Int. Ed.*, 38(1-2):236–240, 1999.

[170] E. Terzi, G. Holzemann, and J. Seelig. Self-association of beta-amyloid peptide(1-40) in solution and binding to lipid-membranes. *J. Mol. Biol.*, 252(5):633–642, 1995.

[171] J. McLaurin and A. Chakrabartty. Characterization of the interactions of Alzheimer beta-amyloid peptides with phospholipid membranes. *Europ. J. Biochem.*, 245(2):355–363, 1997.

[172] C. Ege, J. Majewski, G. H. Wu, K. Kjaer, and K. Y. C. Lee. Templating effect of lipid membranes on Alzheimer's amyloid beta peptide. *ChemPhysChem*, 6(2):226–229, 2005.

[173] C. Aisenbrey, T. Borowik, R. Bystrom, M. Bokvist, F. Lindstrom, H. Misiak, M-A. Sani, and G. Grobner. How is protein aggregation in amyloidogenic diseases modulated by biological membranes? *Europ. Biophys. J. Biophys. Let.*, 37(3):247–255, 2008.

[174] G. P. Gorbenko and P. K. J. Kinnunen. The role of lipid-protein interactions in amyloid-type protein fibril formation. *Chem. Phys. Lip.*, 141(1-2):72–82, 2006.

[175] J. McLaurin and A. Chakrabartty. Characterization of the interactions of Alzheimer beta-amyloid peptides with phospholipid membranes. *Europ. J. Biochem.*, 245(2):355–363, 1997.

[176] D. Burdick, B. Soreghan, M. Kwon, J. Kosmoski, M. Knauer, A. Henschen, J. Yates, C. Cotman, and C. Glabe. Assembly and aggregation properties of synthetic Alzheimer's a4/beta amyloid peptide analogs. *J. Biol. Chem.*, 267(1):546–554, 1992.

[177] Y. Su and P.T. Chang. Acidic pH promotes the formation of toxic fibrils from beta-amyloid peptide. *Brain Res.*, 893(1-2):287–291, 2001.

[178] S. J. Wood, B. Maleeff, T. Hart, and R. Wetzel. Physical, morphological and functional differences between pH 5.8 and 7.4 aggregates of the Alzheimer's amyloid peptide AP. *J. Mol. Biol.*, 256(5):870–877, 1996.

[179] O. V. Galzitskaya, D. N. Ivankov, and A. V. Finkelstein. Folding nuclei in proteins. *FEBS Lett.*, 489(2-3):113–118, 2001.

[180] Research collaboratory for structural bioinformatics (RCSB), *http://www.rcsb.org/pdb/home/home.do* as at 05-2013.

[181] D. van der Spoel, E. Lindahl, B. Hess, A. R. van Buuren, E. Apol, P. J. Meulenhoff, D. P. Tieleman, A. L. T. M. Sijbers, K. A. Feenstra, R. van Drunen, and H. J. C. Berendsen. Gromacs user manual version 4.5.4, *http://www.gromacs.org/* as at 07-2013.

[182] G. Bussi, D. Donadio, and M. Parrinello. Canonical sampling through velocity rescaling. *J. Chem. Phys.*, 126(1), 2007.

[183] H. J. C. Berendsen, J. P. M. Postma, W. F. van Gunsteren, A. Di Nola, and J. R. Haak. Molecular-dynamics with coupling to an external bath. *J. Chem. Phys.*, 81(8):3684–3690, 1984.

[184] T. Darden, D. York, and L. Pedersen. Particle mesh Ewald - an n·log(n) method for Ewald sums in large systems. *J. Chem. Phys.*, 98(12):10089–10092, 1993.

[185] U. Essmann, L. Perera, M. L. Berkowitz, T. Darden, H. Lee, and L. G. Pedersen. A smooth particle mesh Ewald method. *J. Chem. Phys.*, 103(19):8577–8593, 1995.

[186] C. Oostenbrink, A. Villa, A. E. Mark, and W. F. van Gunsteren. A biomolecular force field based on the free enthalpy of hydration and solvation: The GROMOS force-field parameter sets 53A5 and 53A6. *J. Comp. Chem.*, 25(13):1656–1676, 2004.

[187] W. Humphrey, A. Dalke, and K. Schulten. VMD: visual molecular dynamics. *J. Mol. Graph.*, 14(1):33–38, 1996.

[188] C. Schladitz, E. P. Vieira, H. Hermel, and H. Mohwald. Amyloid-beta-sheet formation at the air-water interface. *Biophys. J.*, 77(6):3305–3310, 1999.

[189] J. Danielsson, A. Andersson, J. Jarvet, and A. Graslund. N-15 relaxation study of the amyloid beta-peptide: structural propensities and persistence length. *Magn. Reson. Chem.*, 44(SI):S114–S121, 2006.

[190] X. Daura, A. E. Mark, and W. F. van Gunsteren. Parametrization of aliphatic CHn united atoms of GROMOS96 force field. *J. Comp. Chem.*, 19(5):535–547, 1998.

[191] M. Guo, P. M. Gorman, M. Rico, A. Chakrabartty, and D. V. Laurents. Charge substitution shows that repulsive electrostatic interactions impede the oligomerization of Alzheimer amyloid peptides. *FEBS Lett.*, 579(17):3574–3578, 2005.

[192] C. H. Davis and M. L. Berkowitz. Structure of the amyloid-beta (1-42) monomer absorbed to model phospholipid bilayers: a molecular dynamics study. *J. Phys. Chem. B*, 113(43):14480–14486, 2009.

[193] J. M. Alarcon, J. A. Brito, T. Hermosilla, I. Atwater, D. Mears, and E. Rojas. Ion channel formation by Alzheimer's disease amyloid beta-peptide (Abeta40) in unilamellar liposomes is determined by anionic phospholipids. *Pept.*, 27(1):95–104, 2006.

[194] E. Terzi, G. Hölzemann, and J. Seelig. Interaction of Alzheimer β-amyloid peptide (1-40) with lipid membranes. *Biochem.*, 36(48):14845–14852, 1997.

[195] C. C. Curtai, F. E. Ali, D. G. Smith, A. I. Bush, C. L. Masters, and K. J. Barnham. Metal ions, pH, and cholesterol regulate the interactions of Alzheimer's disease amyloid-beta peptide with membrane lipid. *J. Biol. Chem.*, 278(5):2977–2982, 2003.

[196] E. E. Ambroggio, D. H. Kim, F. Separovic, C. J. Barrow, C. J. Barrow, K. J. Barnham, L. A. Bagatolli, and G. D. Fidelio. Surface behavior and lipid interaction of Alzheimer beta-amyloid peptide 1-42: a membrane-disrupting peptide. *Biophys. J.*, 88(4):2706–2713, 2005.

[197] H. Leontiadou, A. E. Mark, and S. J. Marrink. Ion transport across transmembrane pores. *Biophys. J*, 92(12):4209–4215, 2007.

[198] R.T. Hamilton and E.W. Kaler. Alkali metal ion transport through thin bilayers. *J. Phys. Chem.*, 94(6):2560–2566, 1990.

[199] M. Jansen and A. Blume. A comparative-study of diffusive and osmotic water permeation across bilayers composed of phospholipids with different head groups and fatty acyl chains. *Biophys. J.*, 68(3):997–1008, 1995.

[200] D. W. Deamer and J. Bramhall. Permeability of lipid bilayers to water and ionic solutes. *Chem. Phys. Lipids*, 40(2-4):167–188, 1986.

[201] R. A. Böckmann, B. L. de Groot, S. Kakorin, E. Neumann, and H. Grubmüller. Kinetics, statistics, and energetics of lipid membrane electroporation studied by molecular dynamics simulations. *Biophys. J.*, 95(4):1837–1850, 2008.

[202] D. P. Tieleman, H. Leontiadou, Mark A. E., and S. J. Marrink. Simulation of pore formation in lipid bilayers by mechanical stress and electric fields. *J. Am. Chem. Soc.*, 125(21):6382–6383, 2003.

[203] H. Leontiadou, Mark A. E., and S. J. Marrink. Antimicrobial peptides in action. *J. Am. Chem. Soc.*, 128(37):12156–12161, 2006.

[204] G. M. Torrie and J. P. Valleau. Nonphysical sampling distributions in Monte Carlo free-energy estimation: umbrella sampling. *J. Comp. Phys.*, 23:187 – 199, 1977.

[205] K. Hukushima and K. Nemoto. Exchange Monte Carlo method and application to spin glass simulations. *J. Phys. Soc. Jap.*, 65(6):1604–1608, 1996.

[206] Y. Sugita and Y. Okamoto. Replica-exchange molecular dynamics method for protein folding. *Chem. Phys. Lett.*, 314(1-2):141–151, 1999.

[207] C. H. Davis and M. L. Berkowitz. Interaction between amyloid-beta (1-42) peptide and phospholipid bilayers: a molecular dynamics study. *Biophys. J.*, 96(3):785–797, 2009.

[208] D. B Rubin. The bayesian bootstrap. *Ann. Statist.*, 9(1):130–134, 1981.

[209] B. Hess, H. Bekker, H. J. C. Berendsen, and J. G. E. M. Fraaije. LINCS: a linear constraint solver for molecular simulations. *J. Comp. Chem.*, 18:1463–1472, 1997.

[210] O. Berger, O. Edholm, and F. Jähnig. Molecular dynamics simulations of a fluid bilayer of dipalmitoylphosphatidylcholine at full hydration, constant pressure, and constant temperature. *Biophys. J.*, 72(5):2002–2013, 1997.

[211] O. Beckstein and M. S. P. Sansom. The influence of geometry, surface character, and flexibility on the permeation of ions and water through biological pores. *Phys. Biol.*, 1(1):42–52, 2004.

[212] A. H. de Vries, Mark A. E., and S. J. Marrink. Molecular dynamics simulation of the spontaneous formation of a small DPPC vesicle in water in atomistic detail. *J. Am. Chem. Soc.*, 126(14):4488–4489, 2004.

[213] A. A. Gurtovenko and I. Vattulainen. Molecular mechanism for lipid flip-flops. *J. Phys. Chem. B*, 111(48):13554–13559, 2007.

[214] R. P. Mason, R. F. Jacob, M. F. Walter, P. E. Mason, N. A. Avdulov, S. V. Chochina, U. Igbavboa, and W. G. Wood. Distribution and fluidizing action of soluble and aggregated amyloid β-peptide in rat synaptic plasma membranes. *J. Biol. Chem.*, 274(26):18801–18807, 1999.

[215] D. P. Tieleman and S. J. Marrink. Lipids out of equilibrium: Energetics of desorption and pore mediated flip-flop. *J. Am. Chem. Soc.*, 128(38):12462–12467, 2006.

[216] A. Grafmüller, R. Lipowsky, and V. Knecht. Effect of tension and curvature on the chemical potential of lipids in lipid aggregates. *Phys. Chem. Chem. Phys.*, 15(3):876–881, 2012.

[217] S. J. Marrink and H. J. C. Berendsen. Simulation of water transport through a lipid membrane. *J. Phys. Chem.*, 98(15):4155–4168, 1994.

[218] T. Sugii, S. Takagi, and Y. Matsumoto. A molecular-dynamics study of lipid bilayers: effects of the hydrocarbon chain length on permeability. *J. Chem. Phys.*, 123(18), 2005.

[219] J. C. Weaver, K. T. Powell, R. A. Mintzer, S. R. Sloan, and H. Ling. The diffusive permeability of bilayer-membranes: the contribution of transient aqueous pores. *Bioelectrochem. Bioenerg.*, 12(3-4):405–412, 1984.

[220] J. Liu and J. C. Conboy. 1,2-diacyl-phosphatidylcholine flip-flop measured directly by sum-frequency vibrational spectroscopy. *Biophys. J.*, 89(4):2522–2532, 2005.

[221] R. Koynova and M. Caffrey. Phases and phase transitions of the phosphatidylcholines. *Biochim. Biophys. Acta*, 1376(1):91 – 145, 1998.

[222] E. B. Wilson. Probable inference, the law of succession, and statistical inference. *J. Am. Stat. Assoc.*, 22:209–212, 1927.

[223] S. Karmakar, R. Lipowsky, and R. Dimova. Interaction of antimicrobial peptide NK-2 with phospholipid membranes. *Unpublished manuscript*, 2013.

[224] Chemistry at Harvard macromolecular mechanics, *http://www.charmm-gui.org/* as at 05-2013.

[225] S. Jo, T. Kim, and W. Im. Automated builder and database of protein/membrane complexes for molecular dynamics simulations. *PLoS One*, 2(9):e880, 2007.

[226] Y. Shai and Z. Oren. From "carpet" mechanism to de-novo designed diastereomeric cell-selective antimicrobial peptides. *Peptides*, 22(10):1629–1641, 2001.

[227] J. Lyklema. Electrokinetics after Smoluchowski. *Colloids Surf. A: Physicochem. Eng. Aspects*, 222:5–14, 2003.

[228] J. N. Israelachvili. *Intermolecular and Surface Forces*. Academic Press: London, 2nd edition, 1992.

[229] M. Eisenberg, T. Gresalfi, T. Riccio, and S. McLaughlin. Adsorption of monovalent cations to bilayer membranes containing negative phospholipids. *Biochem.*, 18(23):5213–5223, 1979.

[230] V. Knecht, B. Klasczyk, and R. Dimova. Macro- versus microscopic view on the electrokinetics of a water–membrane interface. *Langmuir*, 29(25):7939–7948, 2013.

[231] V. Knecht and B. Klasczyk. Specific binding of chloride ions to lipid vesicles and implications at molecular scale. *Biophys. J.*, 104(4):818–824, 2013.

[232] H. A. Stern and S. E Feller. Calculation of the dielectric permittivity profile for a nonuniform system: application to a lipid bilayer simulation. *J. Chem. Phys.*, 118:3401, 2003.

[233] I. S. Tolokh, V. Vivcharuk, B. Tomberli, and C. G. Gray. Binding free energy and counterion release for adsorption of the antimicrobial peptide lactoferricin b on a popg membrane. *Phys. Rev. E*, 80:031911, 2009.

[234] W. Zhao, T. Róg, A. A. Gurtovenko, I. Vattulainen, and M. Karttunen. Atomic-scale structure and electrostatics of anionic palmitoyloleoylphosphatidylglycerol lipid bilayers with Na^+ counterions. *Biophys. J.*, 92(4):1114–1124, 2007.

[235] H. Hauser, A. Darke, and C. Phillips, M. Ion-binding to phospholipids. *Europ. J. Biochem.*, 62(2):335–344, 1976.

[236] E. Ikonen. Cellular cholesterol trafficking and compartmentalization. *Nat. Rev. Mol. Cell Biol.*, 9(2):125–138, 2008.

[237] J. R. Brender, A. J. McHenry, and A. Ramamoorthy. Does cholesterol play a role in the bacterial selectivity of antimicrobial peptides? *Frontiers Immun.*, 3, 2012.

[238] D. Hamelberg, J. Mongan, and J. A. McCammon. Accelerated molecular dynamics: a promising and efficient simulation method for biomolecules. *J. Chem. Phys.*, 120:11919, 2004.

[239] F. Ding, D. Tsao, H. Nie, and N. V. Dokholyan. Ab initio folding of proteins with all-atom discrete molecular dynamics. *Structure*, 16(7):1010–1018, 2008.

[240] R. Kayed, Y. Sokolov, B. Edmonds, T. M. McIntire, S. C. Milton, J. E. Hall, and C. G. Glabe. Permeabilization of lipid bilayers is a common conformation-dependent activity of soluble amyloid oligomers in protein misfolding diseases. *J. Biol. Chem.*, 279(45):46363–46366, 2004.

[241] M. Söderberg, C. Edlund, I. Alafuzoff, K. Kristensson, and G. Dallner. Lipid composition in different regions of the brain in Alzheimer's disease/senile dementia of Alzheimer's type. *J. Neurochem.*, 59(5):1646–1653, 1992.

[242] D. C. Grahame. The electrical double layer and the theory of electrocapillarity. *Chem. Rev.*, 41(3):441–501, 1947.

[243] S. J. Irudayam and M. L. Berkowitz. Binding and reorientation of melittin in a POPC bilayer: computer simulations. *Biochim. Biophys. Acta - Biomembranes*, 1818(12):2975–2981, 2012.

[244] Y. Sugita, A. Kitao, and Y. Okamoto. Multidimensional replica-exchange method for free-energy calculations. *J. Chem. Phys.*, 113:6042, 2000.

Publication List

Parts of this thesis have also been published in the following publication

T. Pobandt and V. Knecht. Free energy of lipid bilayer defects affected by Alzheimer's disease associated amyloid-β_{42} monomers. *J. Phys. Chem. B*, 2014. Doi: 10.1021/jp410477x.

Danksagung

Abschließend möchte ich mich bei all jenen bedanken, die mich während meiner Promotion begleitet und unterstützt und somit maßgeblich zum Gelingen dieser Arbeit beigetragen haben.

Ganz besonders möchte ich mich bei meinem Betreuer Dr. Volker Knecht bedanken, der mir zu jeder Zeit geduldig mit Rat und Tat zur Seite stand, auch wenn dies teilweise aufgrund äußerer Umstände nicht immer ganz einfach war. Er ermöglichte mir die Arbeit an äußerst interessanten und spannenden Themen und war jederzeit bereit meine Forschung in richtige Bahnen zu lenken. Vielen Dank.

Weiterhin möchte ich mich recht herzlich bei Prof. Dr. Martin Schoen von der Technischen Universität Berlin bedanken, der es mir ermöglichte meine Arbeit in seiner Arbeitsgruppe “Theoretische Chemie“ zu Ende zu führen. Hier wurde ich sehr freundlich empfangen, was mir gerade die letzten, doch eher schwierigen Monate des Zusammenschreibens deutlich erleichtert hat.

Die Zeit meines Aufenthaltes an der University of North Carolina at Chapel Hill habe ich sehr genossen und ich habe wissenschaftlich und persönlich interessante und schöne Erfahrungen sammeln können. Hierfür danke ich insbesondere Prof. Dr. Max Berkowitz und seiner Arbeitsgruppe für das hervorragende Arbeitsklima . Ausdrücklichen Dank gebührt dabei Dr. Sheeba Irudayam, die mir mit zahlreichen Diskussionen geholfen hat einen anderen Blick auf meine Forschung zu erhalten.

Weiterhin möchte ich mich bei Petra Erdmann bedanken, die mir bei organisatorischen Anliegen, gerade bezüglich des USA Aufenthaltes, stets behilflich war.